Università degli Studi di Messina

Department of Biomedical and Dental Sciences and Morphofunctional Imaging

Ph. D. in Bioengineering Applied to Medical Sciences

Cycle XXXV

A. A. 2021/2022

PO FSE Sicilia 2020

DEVELOPMENT OF INNOVATIVE PROTOCOLS AND METHODS FOR FUNCTIONAL ASSESSMENT OF MOVEMENT AND NEUROMOTOR REHABILITATION

SSD ING-INF/06

Supervisor:

Prof. Andrea d'Avella

Candidate:

Paolo De Pasquale

Coordinator:

Prof. Michele Gaeta

Index

1. Introduction

Over the years, the role of bioengineering in the medical sciences has been considerably increasing, thanks to the capabilities of new advanced tools and technologies, which are nowadays more widely available in terms of cost and complexity. The goal of bioengineering is to combine engineering methods and tools with life science's medical and biological issues. Bioengineering is applied in the domains of technology, industry, medicine, and in healthcare as well as in the workplace and in sports. Thanks to various multidisciplinary methodologies, bioengineering deals with multiscale modeling of physiological systems (from the molecular-cellular to the functional level), with reference to electrical, magnetic, chemical and mechanical phenomena and their interactions; as well as models identification techniques. Furthermore, bioengineering concerns the instrumentation for biosignals and data acquisition, as well as the signal processing procedures required for clinical purposes. Application opportunities range from the design of devices, aimed at monitoring, diagnosis, therapeutic intervention, the structural or functional replacement of organs or biological functions of a sensory, motor or metabolic type; to the ergonomic aspects of the person's interactions with the environment, including human-machine interfaces; up to the design of intelligent autonomous systems and telemedicine scenarios.

Among the many medical applications, new technologies may have a significant impact on the assessment and therapy of neuromotor disorders. New technologies for the measurement of human movements and the visualization of virtual environments, and their diffusion in the field of consumer electronics, provide sophisticated data acquisition systems and data analysis techniques that allow to study complex movements at negligible cost. These technologies can be applied to the study of human movement both in the context of basic science to understand fundamental aspects of motor control and for medical applications to develop novel neuromotor assessment and rehabilitation protocols. Virtual reality (VR) systems provide both a head-mounted display creating an immersive virtual

environment and a sophisticated instrument for kinematic data acquisition thanks to the integrated motion capture capability. Thanks to commercial cross-platform game engines, immersive real-life scenarios can be easily developed and they can be employed as a controlled environment where to perform daily activities or complex tasks. These systems provide feedback to participants during the performance of motor tasks and rehabilitation training exercises which may allow for quantitative assessment of visuomotor function and for novel neuromotor rehabilitation approaches. For instance, a movement deficit may be compensated, and a patient with a motor disability, such as a stroke survivor, may be assisted to perform a task in the VR better than in reality, providing salient feedback on the functional movement to recover, and improving the patient's participation to the training protocol by reducing the frustration and learned non-use due to the motor impairment, thus encouraging beneficial neuroplasticity. Another advantage of providing altered feedback is the possibility to study the adaptive processes underlying the learning of novel dynamics simulating novel physical environments.

Studying kinematics often requires understanding the patterns of muscle activation which underlie movement generation. In recent years, several approaches have been developed to study the relation between electromyography (EMG) and kinematics or force generation, and to customize rehabilitation protocols in order to restore specific components of the movement affected by the motor impairment. Modern technologies allow to record EMG activity associated with muscle contraction using lightweight wireless sensors, which can be used for investigating complex movements in a noninvasive way. Some of these systems, developed for other purposes such as gaming are now available at an affordable price, which may promote a more extensive use of these technologies also in telemedicine scenarios. EMG signals have also been used for the control of assistive exoskeletons or prostheses. However, myoelectric interfaces are typically not very reliable and decoding participant's intention through EMG signals is still challenging. Thanks to the advancements in machine learning techniques, it is now possible to reliably decode EMG signals in a reasonable time for real time applications. Using myoelectric interfaces in a

rehabilitation context may promote usages of residual myoelectric activity of the impaired limb to assist patients in generating voluntary movements through their spared cortico-spinal pathway, promoting neuroplasticity that reshape neuromuscular activity and enhance motor learning, leading in some cases to motor function restoration.

Thanks to the instrumental evaluations, quantitation assessment of physiological parameters may be performed. For instance using modern statistical analysis, such as linear discriminant analysis (LDA) which is a supervised classification technique, it is possible to quantify the degree of separation of observations in different groups. Therefore, it is possible to define different kinematic styles and inter individual strategies.

Most of the applications developed during my PhD require a user interface (UI) to set experimental parameters and to avoid and prevent artifacts recordings during data acquisition. UI is generally designed after an iteration process which includes all the professionals involved (medical doctors, therapists, engineer and researcher).

The common thread among the various projects presented in this thesis is the development of bioengineering techniques to carry out functional assessments. For each project, different methods of data acquisition, processing and analysis were developed based on the nature of the data to be recorded and the task of interest. In some cases, when some systems capable of recording the data required to analyze the specific task had already been developed and described in the literature, the aim of the project was to develop a low-cost solution capable of recording data with high accuracy and reliability. In other cases, when from a literature review no systems were found to match the requirements of a specific application, new developments were made to improve existing systems overcoming their limitations. When required for the development of a system, physiological models were created with reference to the mechanical phenomena and the interactions between the user and hardware components, or the ergonomic aspects of the person's interactions with the environment. Moreover, machine learning techniques have been integrated to allow the design of

intelligent partially autonomous methods. Finally, when the data acquisition systems were already available, advanced analysis methods were applied to the acquired data.

Overall, three low-cost systems have been developed in collaboration with national and international research centers. The first system developed (Chap 3) allows to record the kinematic parameters during throwing actions through the development of a platform which integrates optoelectronic systems, synchronized camera systems, artificial intelligence methods for the automatic estimation of the distance from the point of impact of the ball from the center of the target and a hand-ball model to make the estimation of the throwing parameters as reliable as possible. The second low-cost system (Chap. 4) allows not only to record kinematic parameters through optoelectronic sensors, but also the recording of electromyographic signals, and thanks to artificial intelligence techniques to recognize hand gestures through the electromyographic activity of forearm muscles. In line with this project, some data analyses and initial developments were carried out to evaluate the feasibility of further developments to incorporate electromyographic recording of several muscles for the estimation, through machine learning methods, of the spatial position of the hand rather than just hand gesture (Chap. 5). The last developed data acquisition system, based on a force transducer, is a system for evaluating the maximum bite force (Chap. 6). This system allows to evaluate the maximum bite force and to monitor it over time providing reliable and repeatable recordings, thanks to the development of a mechanical model which describes the physical interactions between the masticatory system and the device and takes into account the physiognomy of the subject. However, it was not always necessary to develop a data acquisition setup. Indeed, in chapter 2, the data acquisition setup was previously developed. In this case, the focus was more on the use of kinematic data processing and analysis techniques.

Table 1.1 shows a schematic representation of all the projects developed during the PhD. For each project the table reports the methods developed and integrated in the systems (✓), the methods which are not included (✗) and the methods which will be included in the next future (✗*).

Chapter	Description	VR	EMG	Machine Learning	UI	Data Analysis
2	Interception of virtual throws	✓	✗	✗	✗	✓
3	Real and virtual throws	✓	✗	✓	✓	✓
4	Virtual mirror therapy	✓	✓	✓	✓	✓
5	Virtual mirror therapy new developments	✗*	✓	✓	✗*	✓
6	Maximum bite force measurement device	✗*	✗*	✗	✓	✓

Table 1.1. Summary of PhD projects and methods involved. For each project the table indicates the methods that have been developed and integrated in the systems (✓), the methods not included in the development (✗), and the methods which will be included in the next future (✗*).

2. Evaluation of sensorimotor performance through motion recording and virtual reality systems

Based on:

Maselli, A., De Pasquale, P., Lacquaniti, F., & d'Avella, A. (2022). Interception of virtual throws reveals predictive skills based on the visual processing of throwing kinematics. iScience, 25(10), 105212. https://doi.org/10.1016/j.isci.2022.105212

2.1. Introduction

Intercepting fast objects requires predictive abilities. Sensorimotor control of interception is affected by latencies intrinsic to the processing of sensory information and to the planning and execution of motor commands (Zago et al., 2009). Altogether, these latencies may sum up to several hundreds of milliseconds, a temporal window in which a fast object may travel distances of the order of a few meters. It is, therefore, clear that successful interception must rely on predictive processes that anticipate the future trajectory of the flying object.

Predictions of flying ball trajectories can be made based on information from the ball's flight itself. Evidence from previous studies suggested that the human brain integrates information from the ball trajectory with an internal model of the physical laws of motion under gravity to predict successful interception points (Russo et al., 2017; Zago et al., 2008). Alternatively, prospective models assume that in interceptive tasks the hand is continuously guided by the visual information from the moving object (Peper et al., 1994). Both cases hold that predictions are continuously updated during the projectile's flight (Brenner & Smeets, 2018).

In addition to the ball trajectory, the throwing action can provide information for predicting the ball trajectory (Maselli et al., 2017). The kinematics of intentional actions, namely the way our body segments move in space and time, provide information about the goal of the

action ahead of its completion. This has been shown for simple actions, such as reaching for a bottle to pour water into a glass or to move it to another location (Ansuini et al., 2008). Importantly, such modulation in the kinematics of executed actions can be decoded by human observers who are able to anticipate appropriate responses (Ansuini et al., 2015; Cavallo et al., 2016; Soriano et al., 2018). Similar results have been found for more complex motor behaviors. The full-body kinematics of tennis serve (Huys et al., 2009) or of an overarm throw (Maselli et al., 2017) delivers information about the future direction of the hit or thrown ball. Elite sports players can use this information for enhancing their interceptive performance, but only in the context of the sports they have extensively trained (Abernethy, 1990; Aglioti et al., 2008; Mann et al., 2010). Most studies to date investigated how predictive skills based on the observation of complex actions depend on motor expertise. However, whether non-experts can readout information from complex but ecological relevant actions, like throwing, remains unclear. In the current study, we addressed this issue.

Our aim was to assess whether untrained adults can extract information from observed overarm throwing actions to improve their interceptive performance. We considered overarm throwing because, besides being a complex full-body motor behavior well studied in sport science, it is part of the repertoire of universal human motor behaviors (Payne, 2017) observed across cultures and geographical regions (Lombardo & Deaner, 2018; Young, 2009). Still further, throwing as a fundamental motor behavior has been associated with the shaping of the biomechanical bodily structure, and with the development of cognitive skills throughout human evolution (Calvin, 1982; Roach et al., 2013; Roach & Richmond, 2015). It is, therefore, plausible that, along with the innate ability to perform overarm throws, humans have developed skills to decode information from observed throwing actions to enhance their performance in interpersonal interactions involving throwing and catching objects, also a pervasive behavior in humans.

In previous studies, we examined overarm motor behavior in untrained adults (Maselli et al., 2017, 2019) who were instructed to perform free overarm throws at different targets placed at six meters distance. By combining dimensionality reduction and machine learning techniques we could characterize the predictability of individual throwers by quantifying advanced (i.e. preceding ball release) information that would permit an observer to anticipate the outgoing direction of the projectile (Maselli et al., 2017). In particular, we extracted the spatiotemporal profile of advanced information in the kinematics of individual throwers, by computing the accuracy with which it is possible to distinguish throws directed to the right, rather than to the left when looking at specific body segments and at different temporal phases of the throwing action. Results revealed how the full-body kinematics of throwing actions encodes information about the outgoing ball direction well ahead of ball release (up to 600 ms in advance). Large interindividual differences were found across participants, with advanced information distributed dishomogeneously in time and throughout body segments in a way that varies across individuals. So, while some throwers deliver most of the relevant information from their stepping trajectories, for others trunk rotations may be more informative. The question then arises whether non-expert observers can extract information from a thrower with the same efficiency as data-driven classifiers and whether they are better tuned to extract information from specific patterns of movement which may be present in some throwers but not others.

The marked interindividual variability in the predictability of throwing action is in line with the heterogeneity that emerged from a complementary analysis of the full-body throwing kinematics aimed at characterizing and categorizing throwing actions across genders and individuals (Maselli et al., 2019). The motor pattern adopted in an unconstrained overarm throwing task was, indeed, found to be specific to individual throwers, to the extent that it is possible to recognize the identity and gender of a thrower from the pattern of joint trajectories characterizing a single throw. Despite this, there are similarities in the motor behavior observed across individuals. Four main classes of throwing strategies were identified across a pool of untrained throwers (n = 20), mainly differing in their stepping

pattern and, to a lesser degree, in the trajectory of the throwing arm. The emergence of individual throwing strategies (or styles), above the overall background motor variability characterizing the unconstrained throwing task, finds resonance in the more general view that redundancy in complex motor tasks implies the existence of multiple solutions (Ganesh et al., 2010; Ganesh & Burdet, 2013; Maselli et al., 2019) and with the evidence that individuals tend to adhere to one of the possible solutions (Vidal & Lacquaniti, 2021). These results further motivate and generalize the question above, namely if non-expert throwers can equally extract information from different throwers or are better attuned to a specific class of throwing strategies.

Here we present an experiment designed to assess predictive skills based on the observation of throwing actions in untrained adults. In particular, we wondered whether advanced information, i.e., the information available ahead of ball release that provides hints about the outgoing ball trajectory, can be read out by non-expert observers and exploited in real-time to improve performance in interceptive tasks. In addition, we tested whether interceptive performance based on the observation of throwing actions depends on the throwing strategy of the individual throwing strategy adopted by the observed thrower. For this, we selected four non-expert throwers (with no specific training in throwing and catching sports) from our earlier study (Maselli et al., 2019), each representative of a different throwing style.

2.2. Results

Participants, wearing an immersive virtual reality (VR) headset, were instructed to intercept a virtual ball under three different visibility conditions, using a virtual racket. In two conditions they could see a virtual character facing them and executing a throwing action. In one case the flight of the ball released by the virtual character was visible (*AllVisible*), while in the other the ball was not rendered during its flight (*ThrowerOnly*). The third condition included only the ball flight, starting after an unpredictable interval in which the ball was shown still at a position corresponding to the location of ball release (*BallOnly*). Both the thrower's kinematics and the ball trajectories displayed in the virtual environment accurately reproduced the kinematics of real throws recorded in our previous studies (Maselli et al., 2017, 2019). We included successful throws directed to four different targets and executed by four throwers, representative of the four of previously identified throwing strategies (Maselli et al., 2019). The four throwers were selected so to minimize differences in their predictability temporal profiles. For each of them, four throws, one for each target (Fig. 1), were selected so to minimize the variability in their flight time (seeMethods for more details). All together the experimental design included three factors: the throw visibility (*BallVisibility*), the hit target (*Target*), and the thrower identity (*Thrower*).

Comparing interception performance across conditions allowed to address the research questions in our agenda by testing the following hypotheses. First, we hypothesize that interceptive performance improves when the thrower kinematics is visible in addition to the ball trajectory, i.e., performance in *AllVisible* is better that in *BallOnly* (H1). In addition, we hypothesize that the interception kinematics observed in the *ThrowerOnly* condition allows to disentangle the direction of the invisible ball (H2). If confirmed, both hypotheses would imply that non-expert participants are able to extract and use information from the observed throwing kinematics to prepare favourable conditions for successful interception and to effectively improve performance. We further hypothesize that, when the throwing action is visible, interceptive performance systematically varies with the throwing style of

the opponent (H3). To test this, we inspected interceptive performance in the *ThrowerOnly* condition, for which performances are not dominated and saturated by information from the ball trajectory. Interception performance was assessed based on two variables: the *success rate* of interception (*Score*) and the *minimum distance* between the ball trajectory and the racket (D_{min}). The hypotheses under scrutiny were tested by contrasting *Score* and D_{min} across experimental conditions using respectively generalized linear mixed models (GLMM) and linear mixed models (LMM).

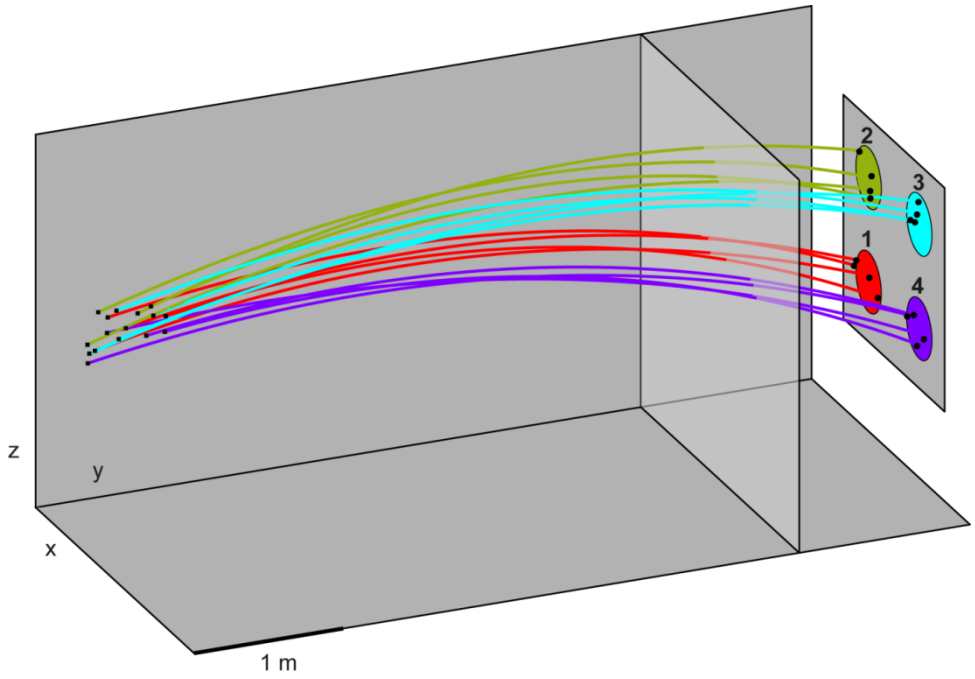

Figure 1: Ball trajectories. The trajectories selected for the four throwers are shown and coloured according to the corresponding target. The four targets are circles of 20 cm radius arranged on a vertical plane placed at a distance of 6 m from the initial position of the thrower. The location of the vertical semitransparent grey plane corresponds to the mean y-coordinate of interceptions across trials and participants. The interception point of the different trajectories with this plane clearly shows how, for each target, differences in the impact point of throws from different throwers are not negligible.

2.2.1. Differences in the ball trajectory alone affect performance

The use of ecological stimuli, namely throwing kinematics and ball trajectories from real throws as visual stimuli, poses the issue of a possible confound associated with unavoidable differences in the trajectories of the different throws. In fact, although the selection of the throws from different throwers and to different targets have been selected so to minimize the variance in the ball release velocity and in the spatial distribution of the ball trajectories (seeMethods for details), such differences in ball trajectories across conditions cannot be completely suppressed. The potential impact of such difference on performance should be then taken into account when comparing performances associated with individual throwers.

The trajectories selected for the different combinations of thrower and target are shown in Figure 1, where differences across conditions can be clearly appreciated. We thus tested whether these differences in the ball flight alone (so in the *BallOnly* condition) affected interceptive performances. Both performance variables, *Score* and D_{min}, exhibit a noticeable modulation by *Thrower* (Fig. 2). Performance showed similar level of modulation by *Target* (Fig. 3). *Score* data were fitted with the GLMM model in Eq. 1 in Methods ($R^2 = 0.19$), which revealed a significant main effect of *Target* ($p = 0.008$) and a significant interaction between *Target* and *Thrower* ($p < 10^{-10}$). Post-hoc analysis, based on the comparisons of the coefficients of the dummy variables and their interactions (values for the dummy variables were defined with respect to the reference condition Target 4 – Thrower 2, which has the highest mean *Score* value in the *BallOnly* condition) revealed that: i) *Score* for Target 2 were significantly lower with respect to *Score* for Target 4 ($p = 0.003$), and ii) *Target* by *Thrower* interactions were significant for all throwers and both Targets 2 and 3, with *Score* values in all the 6 conditions all lower than in the reference condition ($p < 0.01$ for all comparisons).

The corresponding LMM model was fitted on D_{min} ($R^2 = 0.25$). In this case, the main effect of of *Target* ($p = 0.009$) and the *Target* × *Thrower* interactions ($p < 10^{-10}$). Post-hoc analysis revealed that the *Target* by *Thrower* significant interaction is associated with D_{min} values

being significantly larger than in the reference condition (Target 4 – Thrower 2) in the following conditions: Target 2/3 – Thrower 1 ($p = 0.001$ and $p < 10^{-10}$ respectively), Target 2/3 – Thrower 3 ($p < 10^{-10}$ and $p = 0.02$ respectively), Target 1/3 – Thrower 4 ($p = 0.007$ and $p < 10^{-4}$ respectively).The detailed output from both the GLMM and LMM models discussed above can be found in the supplementary online material.

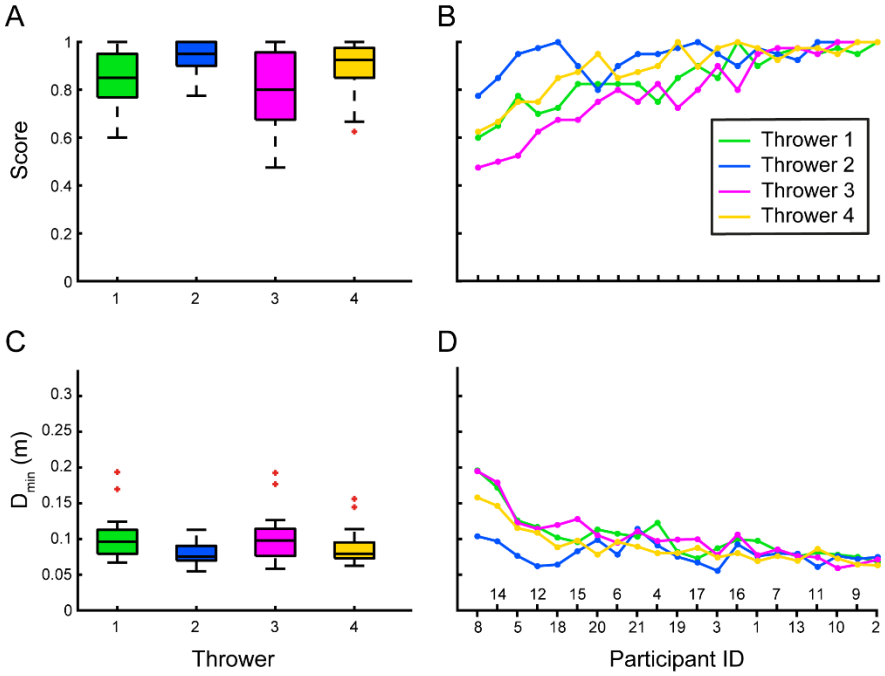

Figure 2. Performance in the *BallOnly* condition: the effect of *Thrower*. (**A**, **C**) The box plots show the distributions across participants of *Score* and D_{min} for the four throwers included in the study. (**B**, **D**) The *Score* and D_{min} values from individual participants are shown, with participants ordered along the x-axis by decreasing levels of overall (across all targets and throwers) *Score* in the *BallOnly* condition.

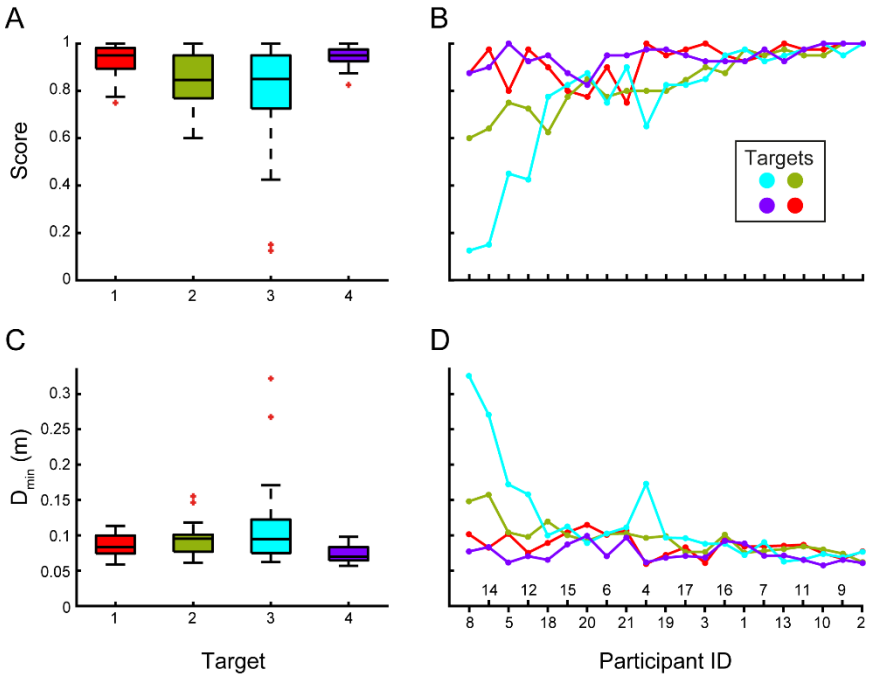

Figure 3. Performances in the *BallOnly* condition: the effect of *Target*. (**A**, **C**) The box plots show the distributions across participants of *Score* and D_{min} for the four targets included in the study. (**B**, **D**) The *Score* and D_{min} values from individual participants are shown, with participants ordered along the x-axis by decreasing levels of overall (across all targets and throwers) *Score* in the *BallOnly* condition.

The performances of individual participants (panels B and D of both Fig.s 2 and 3) clearly show how modulations of performance by both *Thrower* and *Target* are dominated by participants with the worst performance. It is interesting that among the worst performing participants a consistent pattern of performance modulation is observed, which indicates that some trajectories are easier to intercept. In particular, trajectories hitting the bottom targets (1 and 4) are easier to intercept than those hitting the top targets. Top left trajectories (to Target 3) are the most difficult, as to be expected given that all participants used the right hand to intercept the ball.

The significant differences in performance reported here are attributed to differences in the ball trajectories alone, as the throwing action is occluded in the *BallOnly* condition. As this could be a possible source of confound when testing the impact of thrower visibility on

interceptive performance, we considered performance differences between throws to each target and by each thrower.

2.2.2. Thrower visibility improves interceptive performance

To test whether viewing the throwing action in addition to the ball trajectory improves interceptive performance (H1) we compared performance (both *Score* and D_{min}) in the *AllVisible* and *BallOnly* conditions, treating *Thrower* and *Target* as additional independent factors. To take into account the impact of different ball trajectories on performance, we considered the performance difference between the two *ThrowVisibility* conditions, i.e. ΔS = *Score*(*AllVisibile*) − *Score*(*BallOnly*) and $\Delta D_{min} = D_{min}$(*AllVisibile*) − D_{min}(*BallOnly*). Doing so it is possible to appreciate the effect of thrower visibility on the performance in the same set of ball trajectories. Distributions of these differences across participants are shown in Figures 4 for the different *Throwers* and in Figures 5 for the different *Targets*.

Despite the large inter-individual variability and the small absolute values of ΔS and ΔD_{min}, they both appear to be skewed towards positive and negative values respectively, both pointing to an overall improvement in the performance when viewing the throwing action in addition to the ball trajectory. This can be better appreciated for the participants performing the worst in the *BallOnly* condition, for which there was more space for improvement. In particular, the larger improvements were observed for participants 8 and 14, when intercepting throws from *Thrower* 1 and 3 directed to *Target* 3.

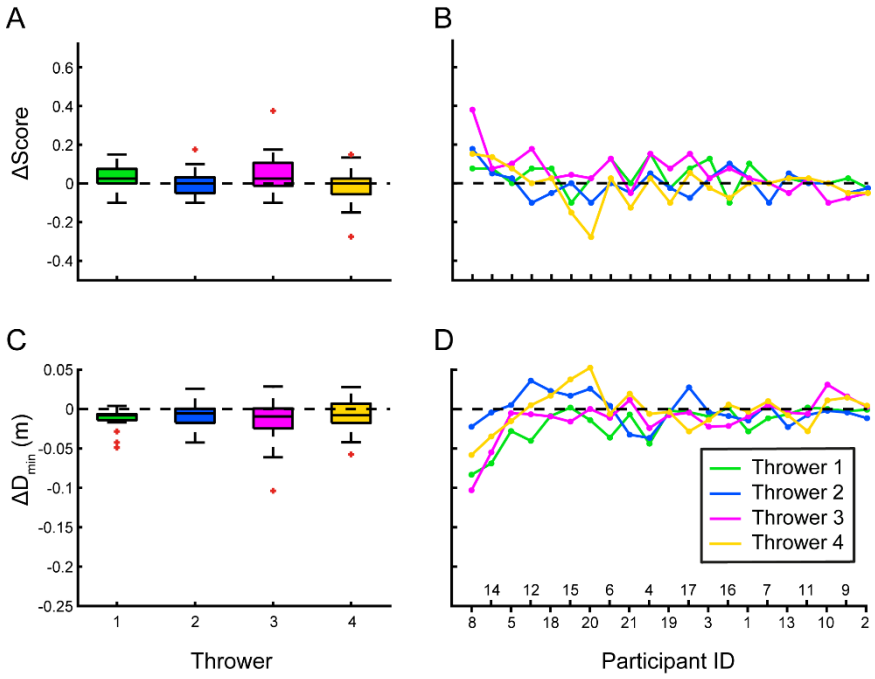

Figure 4. Difference in performance between *AllVisible* and *BallOnly* conditions: the effect of *Thrower*. (**A**, **C**) The box plots show the distributions across participants of ΔS and ΔD_{min} (differences across visibility conditions) for the four throwers included in the study. (**B**, **D**) The corresponding values from individual participants are show, with participants ordered along the x-axis by decreasing levels of overall (across all targets and throwers) *Score* in the *BallOnly* condition.

Statistical significance of the differences across visibility conditions were tested using the GLMM model in Eq. 2 in Methods for *Score* ($R^2 = 0.14$) and the corresponding LMM model for D_{min} ($R^2 = 0.23$). The model includes three main factors, *Target*, *Thrower* and *TrialType*, and their interactions. The *TiralType* factor was included to test the effect of thrower visibility by comparing the *AllVisible* versus *BallOnly* conditions.

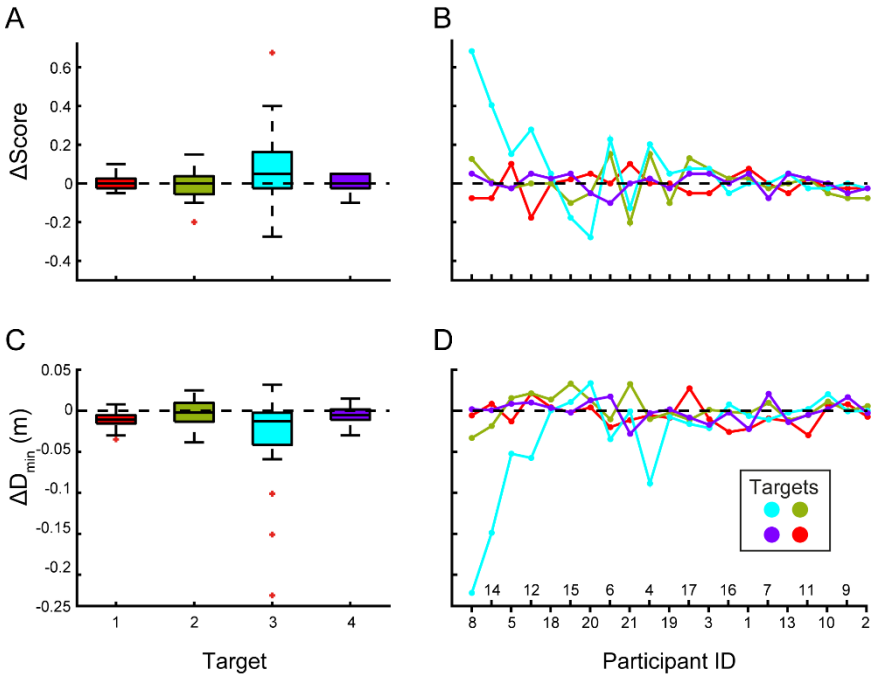

Figure 5. Difference in performance between *AllVisible* and *BallOnly* conditions: the effect of *Thrower*. (**A**, **C**) The box plots show the distributions across participants of ΔS and ΔD_{min} (differences across visibility conditions) for the four targets included in the study. (**B**, **D**) The corresponding values from individual participants are show, with participants ordered along the x-axis by decreasing levels of overall (across all targets and throwers) *Score* in the *BallOnly* condition.

For *Score* we found a significant main effect of *Thrower* ($p < 0.001$) and significant effects for all the two-way interactions tested, i.e., between *Target* and *Thrower* ($p < 10^{-10}$), between *Target* and *TrialType* ($p = 0.018$), and between *Thrower* and *TrialType* ($p = 0.032$). In addition a significant three-way interaction of *TrialType* with *Thrower* and *Target* ($p < 0.001$) was found. Post-hoc analysis revealed that *Score* values for Thrower 1 and 3 were significantly lower than for the reference Thrower 2 ($p = 0.004$ and $p = 0.032$ respectively), and that *Score* values for Target 1 are significantly lower that for reference Target 4. The effect of thrower visibility was instead significant only for a subset of conditions: *Score* values were higher in the *AllVisibile* conditions for throws to Target 2 ($p = 0.01$), in particular for Thrower 3 and 4 ($p = 0.040$ and 0.042 respectively), as well as for throws to Target 3 but only for Thrower 4 ($p = 0.034$). In addition, a number of significant two-way interactions between *Target* and

Thrower were found (see the complete output of the model in the supplementary online material).

Similar results were obtained for D_{min}, for which, in addition to the significant effects reported for *Score*, we found a significant effect of *Target* ($p = 0.02$). The effect of thrower visibility was significant only in its interaction with the *Target* and *Thrower* factors. The complete output from the model can be found in the supplementary online material.
These outcomes support the observation drawn above in discussing Figures 4 and 5, and thus confirm hypothesis H1 showing how interceptive performance improves when viewing thrower kinematics in addition to ball trajectory, although the effect could be appreciated only for some combinations of *Thrower* and *Targets*, and in particular for ball trajectories that cannot be intercepted with optimal performance (*Score* > 0.8) in the *BallOnly* condition.

Improvement in performance associated with vision of the throwing action may derive from the ability to extract advance information about the future direction of the outgoing ball that can be used to prepare more effectively the interceptive movement, for example by directing the hand in the region of interest and/or taking a preparatory posture allowing for better hand control. To corroborate this interpretation, we looked at interceptive performance in the *ThrowerOnly* condition to test whether participants could discriminate the direction of the invisible ball based on the throwing kinematics alone (H2).

2.2.3. Untrained adults can extract information about the outgoing ball direction based only on the throwing kinematics

Effective interception of the invisible ball trajectory with the racket surface is an extremely difficult task. For this, for each trial we estimated *extended interception point*, defined as the location of the centre of the virtual racket at the time of its minimum distance (D_{min}) from the ball's trajectory. We then inspected the difference in the distribution of the *extended*

interception point across the four targets. The distributions of the extended interception points for throws to the four targets are represented in Figures 6 as the 2D ellipses obtained by projecting them onto the frontal (xz) plane, separately for the different throwers (columns) and for four representative participants (rows). The latter were chosen among all participants as the ones performing better and worse in the Right-vs-Left (P19 and P7 respectively) and Up-vs-Down discrimination (P6 and P2 respectively), as revealed by the linear discriminant analysis (LDA) discussed below. For participant 6 the ellipses associated with different targets tends to occupy different regions of the space, with a spatial arrangement that corresponds to the target positions both in elevation and laterally, indicated a capacity to correctly discriminate the direction of the occluded balls based on information extracted exclusively from the throwing kinematics. Participant 19 instead is characterized by a clear separation of the ellipses by side but not in elevation, therefore the ability to discriminate the lateral direction of the occluded balls, but not their elevation. A similar trend, but with a lower degree of ellipses separation is observed for participant 2. The discrimination ability drops drastically for participant 7, characterized by larger ellipses (indicating a larger variability in the extended interception points distributions) and a higher degree of overlap among them. For most participants (supplementary Figure S1), the separation between targets at different sides (Right-vs-Left) appears to be larger than for target at different elevation (Up-vs-Down), suggesting an overall better predictability of the ball direction on the horizontal (mediolateral) direction, rather than on the vertical direction. Interestingly, differences in the ellipses geometry and spatial arrangement can be clearly noticed when comparing different throwers.

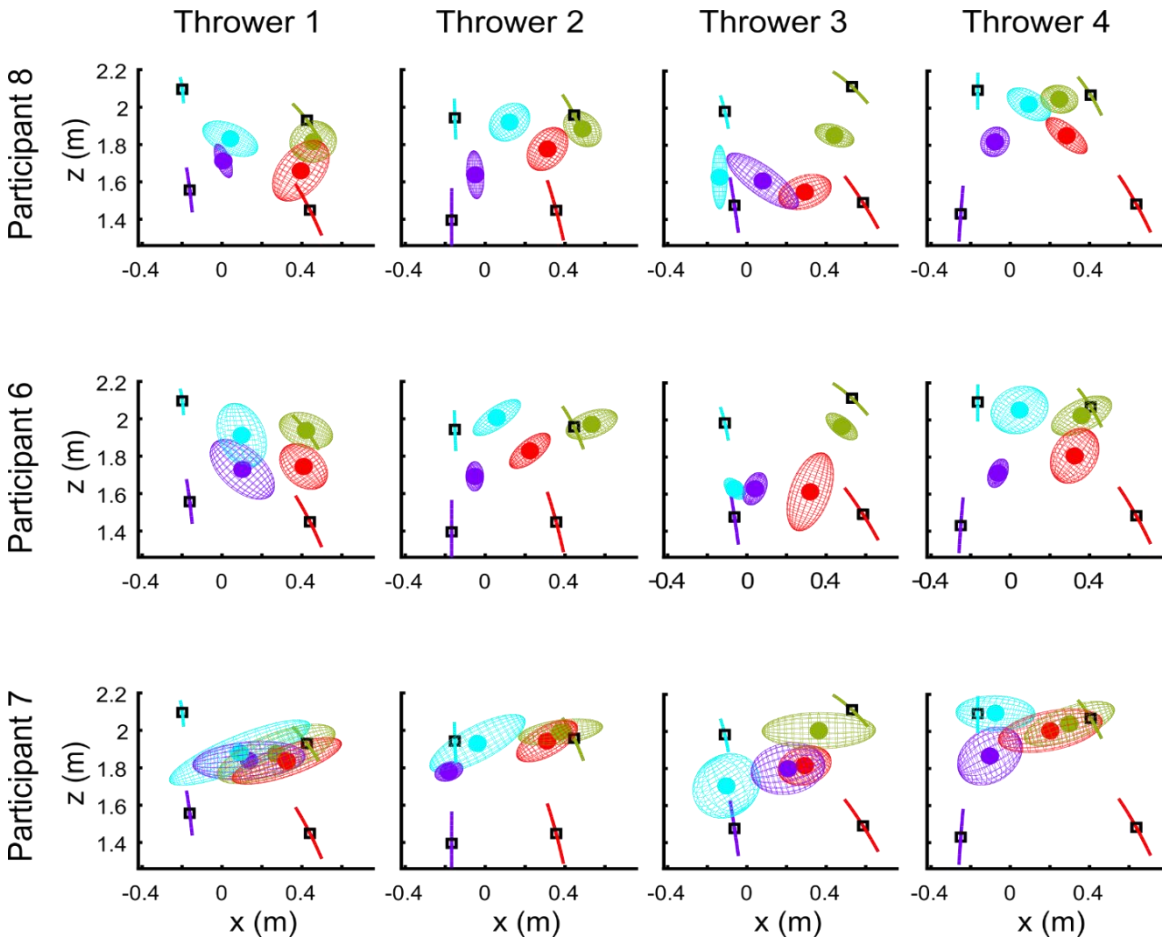

Figure 6. Distributions of extended interception points. The four ellipsoids in each panel represent the distribution of the extended intercepting points for throws directed to the different targets, coded by colour. The centre of each ellipsoid corresponds to mean (averaging extended interception positions across the corresponding subset of trials), whereas the principal semi-axes correspond to the standard deviation of the distributions along the 3 directions of higher variability. Panels in the three rows represents performance from three representative participants. Panels along the four columns corresponds to participants performance in the subset of throws from individual throwers.

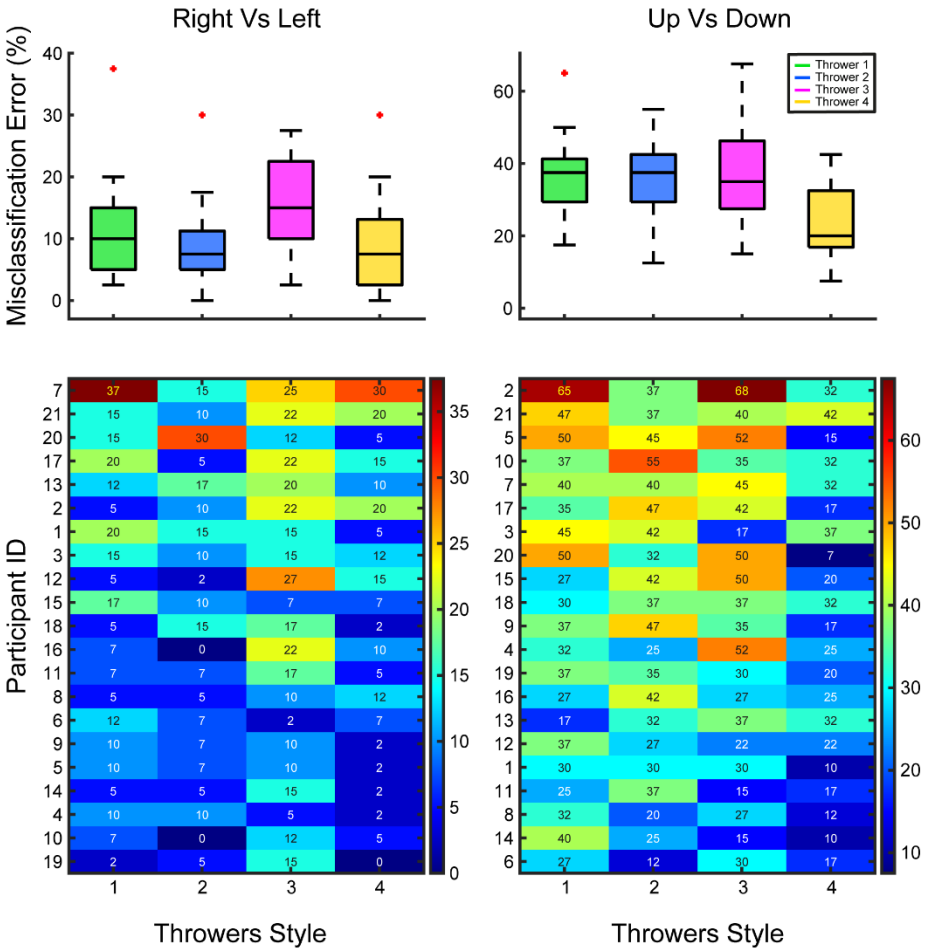

Figure 7. Results from the linear discriminant analysis (LDA) applied to the problem of ball side and elevation discrimination in the ThrowerOnly condition trials. (**A**) Heat map show the resulting misclassification errors from LDA applied to the Right-vs-Left (left panel) and Up-vs-Down (right panel) problems, for all participants (rows) and for the different throwers (columns); participants are ordered from top to bottom in decreasing order of average misclassification errors across throwers. (**B**) Boxplots provide the summary statistics (across participants) of the misclassification errors from LDA applied to the Right-vs-Left (left panel) and Up-vs-Down (right panel) problems, associated with the four throwers.

As a quantitative assessment, we used a linear discriminant analysis (LDA) to test whether the interception kinematics effectively discriminate ball direction. Horizonal and vertical discrimination were tested separately by considering two 2-class problems: Right-vs-Left and Up-vs-Down. For each participant (catcher), the analysis was conducted on the four

subsets of trials associated with the different throwers. The LDA model was trained with the positions of the extended interception points, each labelled according to the belonging class (Right/Left, Up/Down) of the corresponding throw. Results are shown in Figure 7A, in terms of misclassification errors (MEs) estimated with the one-leave-out method (seeMethods for more details). Figure 7B shows the summary boxplots corresponding to the MEs distributions across all participants for the different throwers. In the horizontal classification problems, the ME values for all possible combinations of catcher and thrower are well below chance level (50 per cent for the 2-class discrimination problems), with an average value of 11.43 and standard deviation of 7.58. The misclassification errors for the vertical discrimination problem are larger, with an average value of 32.92 and standard deviation of 12.42. Indeed, for this problem not all combinations of catchers and throwers have misclassification rates below chance level, implying that some participants were not able to correctly infer the vertical arrival position of the outgoing ball for one or more throwers.

We next tested whether the extraction of information of the outgoing ball trajectory from the throwing kinematics depended on the thrower. For this, we fit *Score* and D_{min}, in the *ThrowerOnly* condition, with GLMM and LMM respectively, adopting the models in Eq. 1 of Methods. For both we found a significant main effect of *Target* and *Thrower*, and a significant interaction between the two; all p-values are below 10^{-6}, but for the main effect of *Thrower* on *Score*, which is 0.016. The detailed output of both models can be found in the supplementary online material.

In sum, these results indicate that untrained individuals are able to extract information about the future ball direction on the basis of the throwing kinematics alone, thus confirming our hypothesis H2, and that the ability to extract information is significantly modulated by the thrower kinematics strategy, thus confirming H3.

2.3. Discussion

The current study shows that human adults, not specifically trained in throwing sports, are able to extract information from the observed kinematics of a throwing action, and to use online this information to enhance their interceptive performance. Participants who had to intercept a thrown ball in an immersive virtual reality setup, performed better when they could see the complete throwing action in addition to the ball flight. Moreover, when the ball was occluded during its flight, participants were able to correctly direct the interceptive action using the information provided by the throwing action alone. In addition, our results highlight how the reported predictive skills based on the observation of naturalistic throwing actions are modulated by the thrower, as the throwing pattern adopted by some throwers could be read out better than the pattern adopted by others. Crucially, these effects are mostly evident for participants having poor interceptive skills, and in general for those conditions in which the baseline performance, corresponding to trials in which only the ball flight was visible, were poor leaving room from improvements associated with the visibility of the throwing action.

These results extend our current knowledge on the nature of predictive skills for action, and in particular for interceptive behaviour. Studies focusing on interceptive performance have demonstrated how humans make use of internal predictions about projectiles trajectories to successfully intercept flying objects, plausibly based on an internal model of how objects moves under the effect of gravity (Dayan et al., 2007; Russo et al., 2017; Zago et al., 2008). Our results show that untrained adults are able to correctly predict the direction of projected objects also based on the kinematics of the throwing action. Notably, this implies a more complex ability for predictions with respect to the processing of a ball flight. Previous studies have demonstrated the ability of elite sport athletes to correctly infer the future direction of a thrown ball based on the observed throwing movement of an opponent, but this ability has been so far considered a skill learned throughout extensive and sport-specific training. So, anticipatory skills based on action observations have been shown to be higher

for elite athletes than for non-experts (Abernethy, 1990; Farrow et al., 2005; Müller & Abernethy, 2012), but only if they were specifically trained in the observed throwing or kicking technique (Aglioti et al., 2008; Mann et al., 2010). While these results demonstrated that specific training enhances predictive skills, our results provide direct evidence that humans have the ability to extract and use online advanced information from observed throwing actions for the successful interception of projected objects even without training. It may be possible that such predictive ability evolved together with throwing (Calvin, 1982; Lombardo & Deaner, 2018; Roach et al., 2013; Young, 2009) and catching skills, although this is a speculation that needs to be further explored in dedicated studies.

Results from the current study are also interesting in the context of social neuroscience. Humans are known to extensively rely on predictions based on the observation of biological motion for inferring others intentions and anticipating the future unfolding of observed actions (Ambrosini et al., 2015; Ansuini et al., 2015; Cavallo et al., 2016). These predictive mechanisms are thought to be key to guarantee a smooth and effective interpersonal interaction based on non-verbal communication (J. R. Flanagan & Johansson, 2003; Giese & Rizzolatti, 2015; Pezzulo et al., 2019). Still, established experimental evidences for these overall conclusions are largely based on the examination of simple actions, such as reaching for an object to grasp and/or move it (Aglioti et al., 2008; Ansuini et al., 2008; Donnarumma et al., 2017; J. R. Flanagan & Johansson, 2003). Here we showed that similar mechanisms are at play in complex forms of interpersonal interactions, demonstrating that not only humans are able to predict the unfolding of complex full-body action involving the manipulation of external objects, but they are also able to use online these predictions to optimize the interaction. So, our results extend previous research on interpersonal communication by including quantitative assessments of the critical role played by predictive mechanisms associated with action observation in complex and full body motor behaviour.

Importantly, the experimental evidence from the current study are grounded in a scrupulous experimental design, in which the visual stimuli – namely the throwing actions shown to participants in the interceptive task – have been selected based on a previous

analysis in which the information content about the outgoing direction of the projected ball has been fully characterized (Maselli et al., 2017). That study showed a large interindividual variability in throwing predictability, so that individual throwers differ not only in how early (before ball release) they become predictable, but also in the set and sequence of body segments that deliver the most relevant information. Having quantified and characterized the information about the outgoing ball direction encoded in the selected throws, we could then assess the extent to which such information could be decoded by a human observer and make grounded comparisons across different throwers conditions.

In particular, the current study addressed the issue of how differences in the predictability profile of throwers adopting different motor strategies impact on prediction skills and on the ensuing interceptive performance. Results show that interceptive performance varies with the opponent thrower: despite the large interindividual differences, a consistent trend was found across participants for individual throwers being less predictable (e.g., Thrower 3 for side discrimination) or more predictable (e.g., Thrower 4 for elevation discrimination) than others. Although the four throwers were selected so to have comparable temporal profiles of their predictability, differences in their motor strategies and therefore in the kinematics cues (body segments) that convey the relevant information could explain the different degrees of information read out from individual throwers. This suggests that not all information encoded in the kinematics of an action is equally easy to decode, and thus that the human brain may be better tuned to specific bodily cues when decoding observed actions for predicting their incoming unfolding. Nevertheless, it is interesting to notice how results show a better discrimination of the outgoing ball lateral motion with respect to vertical motion, which is in line with the marked differences found for the encoding of the relative information (Maselli et al., 2017).

Noticeably, the grounded comparison of different ecologically valid experimental conditions (in this case different throwing styles) has been granted by the introduction of novel methodology to quantitatively characterize complex motor behaviour (Maselli et al., 2019) and kinematics-driven predictability with a small set of parameters. These

quantitative approaches allow for further sophisticated analysis. For example, one could look at the relation of interceptive performance with the detailed spatiotemporal structure of each thrower's predictability so to point out which are the kinematics cues (e.g., from which body segments) that are easier to decode. One could also wonder whether there is an individual tuning to specific bodily cues and whether this tuning reflects the individual motor expertise and styles (Vidal & Lacquaniti, 2021), as mirror neurons theories would suggest (Calvo-Merino et al., 2010; Casile & Giese, 2006; Giese & Rizzolatti, 2015). In this case, a match in the throwing styles of catcher and thrower would facilitate the decoding of the observed throwing action. While these questions go beyond the aim of the current study, we plan to address them in future studies.

In sum, the results of the present study highlight the ability of humans to formulate detailed predictions about the unfolding of complex full-body actions, and to use online these predictions to optimize interactions. Differently from what suggested by previous studies, our results show that such predictive skills do not require an extensive exposure to, or motor training in, the observed action, and may be therefore rooted in an intrinsic internal knowledge of how common actions in the human-motor repertoire maps into changes in the physical state of the surrounding environment. The combination of ecological valid stimuli, immersive technologies and new methods for describing and categorizing complex actions that allowed to achieve these results, may pave the way for a research agenda that aim at exploring in more details the sensorimotor mechanisms underlaying the role of prediction skills in real-life multi-agents interactions.

2.3.1. Limitations of the study

The current study has some intrinsic limitations associated with the use of immersive virtual reality (IVR). In fact, IVR exposure may affect motor behaviour in a way that it is still not straightforward to predict (Thomas et al., 2016; Zhang & Sternad, 2021). However, IVR

grants the otherwise impossible chance of adopting complex but perfectly reproducible visual stimuli, in our case reproducing with high fidelity the full-body kinematics of throwing actions from real throwers. In this respect, we believe that IVR provides a precious experimental tool for state-of-art research on non-verbal interpersonal interaction, affording the optimal compromise between systematic experimental designs and the use of complex ecologically valid stimuli.

2.4. Methods

2.4.1. Experimental model and subject details

Participants performed a task in immersive virtual reality (IVR), in which they had to intercept a virtual ball thrown by a virtual character. Before this, participants were asked to perform a real throwing session, replicating the task and the experimental procedure adopted in our previous studies (Maselli et al., 2017, 2019). This part of the data collection served for a complementary study in which we aimed at exploring how interceptive performance are affected by the relation between the throwing styles of the catcher and the thrower.

The experiment consisted in a $3 \times 4 \times 4$ within-subjects design, the three factors being the *ThrowVisibility*, *Thrower* and *Target*. All factors modulate the visual stimuli to which participants were exposed in the virtual catching task. The *ThrowVisibility* factor had three levels: *BallOnly*, in which only the ball trajectory was displayed; *ThrowerOnly*, in which the throwing kinematics was displayed but the ball disappeared at the ball-release time; and *AllVisible*, in which both the throwing kinematics and the full ball trajectory was available to participants. The *Thrower* factor had four levels in which the throwing kinematics was modulated: each level corresponded to one of the four throwing styles identified and described in our previous work (Maselli et al., 2019). For each thrower, we further

considered throws to four different targets arranged with respect to the thrower as in (Maselli et al., 2017).

The virtual catching session included 10 repetitions for each condition, summing up to a total of 480 trials presented to participants in a pseudorandom order: trials were grouped in 10 blocks of 48 trials (one for each condition), and trials within each group were arranged in a random order.

Twenty-two participants (11 female; age: 26.5 ± 4.9 years, mean ± std) took part to the experiment. They were all right handed according to the laterality score given by the Edinburgh questionnaires (L: 0.86 ± 0.14). They were informed that they could leave the experiment and/or could ask for breaks at any time. All but one participant (who only performed the throwing session for technical problems) completed the whole experiment. A second participant, despite completing the experiment was excluded from the analysis because they failed in following properly the task instructions.

2.4.2. Method details

2.4.2.1. Throwing stimuli selection

The virtual throws stimuli, including both the throwing kinematics and the ball trajectories, faithfully reproduced the real throwing kinematics recorded from real subjects (Maselli et al., 2017, 2019). First, we selected four throwers among the twenty subjects available, each representative of a throwing style. The four throwers were selected so to match as close as possible the temporal profile of their characteristic "throwing predictability", as computed and reported in (Maselli et al., 2017). To this aim, we minimized the variance of the time intervals before ball release at which the thrower becomes predictable in the groups of four throwers each representative of a specific throwing style. According to this criterium, the selected subjects were P4, P5, P6 and P13 from (Maselli et al., 2017), representative

respectively of the *No-Step*, *Left-Step*, *Right-Step* and *Double-Step* throwing styles identified in (Maselli et al., 2019). The throwing kinematics and corresponding predictability profiles are shown in Figures 3 and 7 of (Maselli et al., 2017), while the animated kinematics as displayed through the HMD can be seen in the supplementary videos SV1-SV4 (showing the throws to Target 1 for all throwers). For each thrower we next selected four throws, one for each target. The throws selected were those that, among the successful trials (i.e. throws hitting the intended target of 20 cm radius), minimized (i) the reciprocal distance of the impact locations on the target board, and (ii) the variance of the flight time across the four throwers. Following these criteria the mean and standard deviation of the flight time across participants, averaged across target, was 0.595 ± 0.02 s, while the mean distance of the same-target arrival locations was 0.17 cm. The kinematics recoded in the selected trials was used to create the virtual throwing stimuli (more details in the "Virtual Scene" subsection). As a sanity check, we computed the differences in flight times and speed at impact of the virtual balls thrown by the different throwers to the four targets in the Unity scenario. Flight time was estimated as the time interval between ball release and the virtual impact of the ball with the plane of average interception (i.e., the vertical xz plane placed at the mean y-coordinate of interceptions across trials and participants shown in Fig. 1). Impact speed was estimated as the ball tangential velocity at the time of intersection with the same plane. Mean and standard deviation across throwers and targets were 0.450 ± 0.01 s for the flight time, and 8.771 ± 0.431 m/s for the ball speed. The corresponding values for each single thrower are given in table T1. The reported differences across throwers have been taken into account when assessing the impact of the individual throwing strategy on interceptive performance by looking at the difference in performances between *AllVisible* and *BallOnly* conditions.

Thrower ID	**Flight Time [s]**	**Impact Speed [m/s]**
1	0.457 ± 0.010	9.178 ± 0.221
2	0.449 ± 0.006	8.290 ± 0.142
3	0.442 ± 0.006	8.979 ± 0.205
4	0.451 ± 0.013	8.638 ± 0.456

Table T1. Ball flight time and impact speed by thrower. The table reports mean and standard deviations across throws to the four targets of ball flight time (from ball release to impact with the plane of average interception shown in Fig. 1) and impact speed for the four throwers included in the experiment.

2.4.2.2. Experimental setup

The experimental setup included a Vive system for IVR and the motion capture optical system OptiTrack for the recordings of full-body kinematics.

The Vive system (HTC Europe Co. Ltd, Slough, Berkshire, U.K), includes two base stations emitting infrared pulses which create a "room scale" tracking area where the headset and the controllers can be tracked with sub-millimeter precision. The headset streams the interactive virtual scenario designed for the virtual catching task, at a refresh rate of 90Hz and a 110° field of view, with a display resolution of 1080×1200 pixels per eye. For the experiment we further used one Vive controller, which participants held in their right hand and used to control a virtual racket for intercepting the virtual ball. The controller was also used to track the hand kinematics during the interceptive task. The Vive system was integrated via SteamVR with the Unity Engine running on a personal computer.

The OptiTrack (NaturalPoint, Inc., Oregon, USA) optoelectronic motion capture system, including its data acquisition and processing software Motive Body, was used to track the full-body kinematics during both the real throwing task and the virtual catching task. Participants were instrumented with 57 retroreflective markers that allowed to track the whole body. The experimental setup for the throwing task replicated exactly the one described in (Maselli et al., 2017).

2.4.2.3. Virtual scenario

The virtual scene has been implemented on the Unity platform. It included an empty room of 8 × 15 m^2 floor size and 5 m height, a 9 cm diameter ball, four virtual characters, and a racket. The latter was generated by attaching a white disk (20 cm diameter, 3 cm thickness) to a virtual replica of the hand-held controller. The four virtual characters were created by resizing the skeleton's body segments of a standard virtual character, so to match the bodily proportion and the high of the real participants selected as throwers. This assured that when loading the kinematics of a specific throw onto the corresponding virtual character as an animation (which is controlled by the joint angles kinematics) the spatial trajectories of the single joints accurately matched the one recorded in the motion capture session. The characters head was occluded by an opaque sphere, in order to remove possible implicit cues about the intended target present in the head movement of the thrower (see Fig. 8). For each throw the ball was animated according to the trajectory of the real ball, also tracked by the motion capture system. Each trial was associated with a single trial and therefore a single thrower. The participant started the throwing stimuli by pressing a button on the hand-held controller while being in a fixed initial position and holding a neutral A-pose, with the feet slightly spread and the arm along the sides of the body. According to the experimental condition, each trial either began either with the thrower appearing in the initial A-pose as in Fig. 9A, facing the participants (*AllVisible*, *ThrowerOnly*), or with the ball appearing at the location corresponding to the throwing release point of the specific trial (*BallOnly*). The animation of the throwing action or the ball flight was started after an average interval of 1 second with a uniformly distributed random jitter of 0.5 seconds, included to make the start unpredictable. In the *AllVisible* condition both the throwing action and the complete ball flight were shown, while in the *BallOnly* and the *ThrowerOnly* condition only the ball trajectory and the avatar throwing action respectively were displayed.

The controller position and orientation were tracked by the HTC Vive system. If the actual ball trajectory was successfully intercepted, a haptic feedback of the event was rendered as a vibration of the controller.

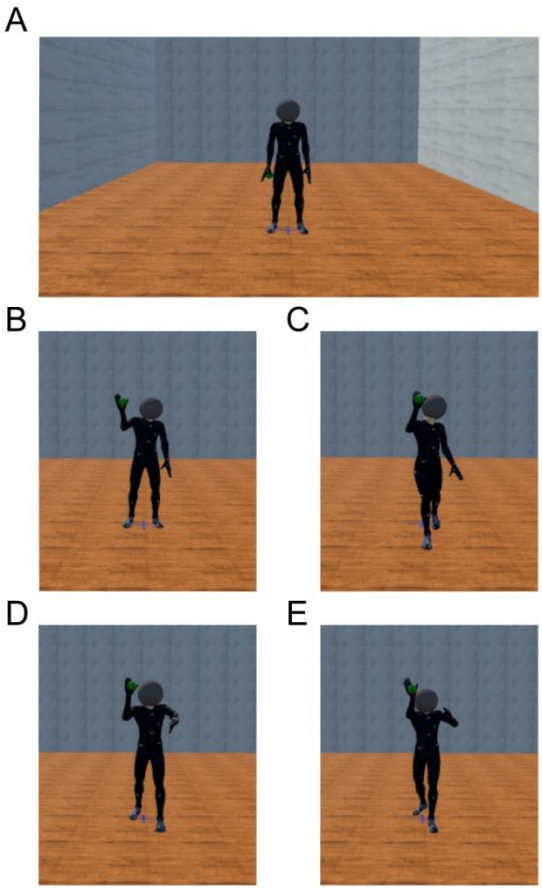

Figure 8. Virtual scene: throwing stimuli. (**A**) The figure shows virtual thrower initial A-pose. (**B**, **C**, **D**, **E**) Snapshots of the different throwers at the moment of ball release.

2.4.2.4. Procedure

Participants were instructed about the experimental procedure and signed a consent form before taking part to the experiment. They then filled the Edinburgh handedness questionnaire for assessing hand preference (Oldfield, 1971), a brief questionnaire about their experience with sport activity, and their previous exposure to immersive virtual

reality. Participants were then instrumented with the retroreflective markers for full-body kinematics recording. This preparation phase took on average 20 minutes.

The experiment started with a brief familiarization with the throwing task followed by the experimental throwing session consisting in 80 throws, 20 for each of four targets arranged on a vertical plane at a distance of 6 meters, see (Maselli et al., 2017) for more details. After the throwing session, participants took a break of about five to ten minutes, after which the virtual interception session started. After being fit the head-mounted display (HMD) and provided with the Vive controller, participants performed few trials for getting familiar with task in the three visibility conditions. The experimental session started next and consisted of 480 trials in which the 48 conditions were presented pseudo-randomly, in 10 consecutive blocks each including all 48 conditions. Participants took one to two breaks in which they could remove the HMD and rest. All together the experiment including both the throwing and virtual interception tasks, plus breaks, lasted on average 90 minutes.

In both throwing and interceptive sessions we recorded full-body kinematics. In addition, in the virtual session we recorded the kinematics of the controller held by the intercepting hand (always the right hand) and of the head with the Vive system. In the current study we focus our analysis on the kinematics of the intercepting hand from the controller. The full-body kinematics of the throwing and interceptive actions will be analysed in future studies. The experimental design and protocol were approved by the Ethical Review Board of the Santa Lucia Foundation (Prot. CE/PROG.542).

2.4.3. Quantification and statistical analysis

2.4.3.1. Data collection and pre-processing

For each trial, the kinematics of the hand-held controller and the position of the virtual racket were recorded from the start of the trial to the time at which the ball impacted the racket or exceeded 5.5 m along antero-posterior axis (y-axis) in the VR environment (moving

so behind the participant). For each trial, we analysed the kinematics of the virtual racket position, which is automatically extracted from Unity as a fixed roto-translation of the tracked controller, and sampled at 90 Hz. Positional data were filtered with a digital low pass-filter (a 5th order Butterworth filter with 10 Hz cutoff frequency). Each trial was labelled as successful, or failed, according to whether there was, or was not, a collision between the ball and the virtual racket. *Scores* values for each combination of participant and experimental condition were computed as the fraction of successful trials. In addition, D_{min} was estimated as the distance at which the position difference between the racket and ball was minimal. For each trial, we also extracted the extended interception point as the position of the virtual racket centre at the time of minimum distance between the ball and the racket. Data were processed in Matlab.

2.4.3.2. Statistical analysis

The dependence of the *Score* and the D_{min} on the experimental factors was tested with generalized linear mixed models (GLMM) and linear mixed models (LMM) that account for interindividual variability by including the participant as a random effect. Different mixed models were adopted according to the metric under scrutiny. The experimental factors, i.e. *BallVisibility* (*BV*), the hit target (*Ta*), and the thrower identity (*Th*)) were treated as fixed effect factors with categorical (dummy) variables. Data from the *BallOnly* and *ThrowerOnly* conditions were fitted with the model described in Eq. 1. Instead, when comparting the impact of the thrower visibility by contrasting the *AllVisible* and *BallOnly* conditions data were fitted with the model in Eq. 2.

$$Y = g\ (u_0 + \alpha_0 Ta + \beta_0 Th + \lambda_0 TaTh + \epsilon) \quad (1)$$

$$Y = g\ (u_0 + \alpha_0 Ta + \beta_0 Th + \gamma_0 BV + \lambda_0 Ta\ Th + \zeta_0 Ta\ BV + \Delta_0 Th\ BV + \delta_0 Ta\ Th\ BV + \epsilon) \quad (2)$$

In equations 1 and 2, u_0 represents the individual intercept and accounts for inter-individual differences. The coefficients α_0, β_0, γ_0, λ_0, ζ_0, Δ_0 and δ_0 represent fixed-effects, thus the modulation of the response variable by the main factors *Ta*, *Th*, and *BV*, and their interactions.

In both equations, g represents the link function. As *Score* data have a binomial distribution (as it could take only two possible outcomes: Y = 1 for hits, and Y = 0 for missed balls), they were fitted with a GLMM using a logit link function (Matlab function *fitglme*). For D_{min} , which represents a continuous variable, data were instead fit with a LMM (thus with g representing the identity functions, Matlab function *fitlme*). In all cases the estimation of model parameters were based on the maximum likelihood using Laplace approximation.

Dummy variables for *Th* and *Ta* fixed effect were defined with respect to the corresponding conditions with the highest mean *Score* in the *BallOnly* visibility condition. Post-hoc comparisons could be then performed by assessing the p-values of the regression coefficients for the dummy variables and their interactions.

In order to test the hypothesis that participants were able to make reliable predictions about the direction of the outgoing ball based on information from the throwing kinematics alone, we run a linear discriminant analysis (LDA) on the points of extended interception for the *ThrowerOnly* condition (Matlab function *fitcdiscr*). LDA is a standard supervised classification technique that may be used to quantify the degree of separation of observations in different groups (or classes). The method consists in finding discriminant functions that divide the space in which observations are defined in a number of predefined regions, by maximizing the ratio of the between-groups to the within-group variabilities in the training set (Mardia et al., 1979). By applying LDA to the distribution of extended interception points for throws directed to different targets it is possible then to quantify the ability of the catcher to discriminate the direction of the invisible ball. We specifically tested the ability to discriminate the lateral direction (Right-vs-Left) and the vertical direction (Up-

vs-Down), with different 2-classes LDA tests. LDA performance for both classification problems have been run separately for all combinations of participants and throwers. The data given in input to train the model were the 3D positions of the extended interception points labelled according to the class of belonging of the associated throw (Up/Down, Right/Left). Results are reported in terms of misclassification errors (MEs) computed with the leave-one-out cross-validation procedure. The latter consists in performing the classification assignment of each single observation (the one left out) based on the training set defined by the rest of the observations, repeating the same procedure for all observations in the data set, and defining ME as the percentage of misclassified observations.

3. Development of a low-cost system for studying motor strategies in complex motor tasks

3.1. Introduction

Humans are extremely dexterous. The Central Nervous system (CNS) manages to smoothly coordinate and accurately control several DOFs and hundreds of muscles. However, several studies in human motor control have focused their investigation on simple tasks (e.g. reaching) in very controlled environments (e.g. reaching to targets arranged on a plane) (Franklin & Wolpert, 2011; Shadmehr & Mussa-Ivaldi, 1994). Albeit the fundamental knowledge about motor control that we have gathered from such studies, it is hard to understand how we can generalize those findings to more complex tasks such as most of the motor tasks encountered outside the laboratories, i.e., in the real world. Therefore, it arises the need to explore more naturalistic behaviors and complex tasks (Russo et al., 2021). With the help of innovative technologies, researchers can now approach this realm of movements, without losing the requirements of an experimental protocol that needs to be reproducible and controlled (Krotov et al., 2022; Maselli et al., 2017, 2019).

A fundamental characteristic of complex tasks is that they show multiple solutions, i.e., an individual can accomplish the same goal with different motor strategy, all successful. In addition, the complexity of body dynamics grows exponentially with the number of DoFs involved. Given that, variability also increases and the computational models, classically used to explore simple behaviors, can no longer be applied (Todorov & Jordan, 2002).
Recently, a new approach that is not limited by the dimensionality of the motor task and can be applied to the actions of daily life and sports activities (Tommasino et al., 2021) has been proposed. In particular, such approach has been used to investigate throwing actions, relating ball release kinematic features to performance. It has allowed to characterize the relationship between individual movement strategies, their variability and performance,

providing a new methodology for investigating sports performance and improving functional recovery after injury.

Tommasino and collaborators analyzed throwing actions of 20 participants. Such dataset was collected with a standard motion capture system and the release instant was determined from hand and ball trajectories. Similarly, the performance was calculated when the ball path intersected the target location. Since in a throw, release parameters (i.e. ball velocity and position) determine the ball trajectory (given drag and gravity), accurate estimation of the release instant is fundamental for the analysis of throwing actions. In addition, the dynamics of the environment affects ball behavior and in turn, also the thrower action. What would be the ball launch like and its performance if the dynamics of the ball was not affected by gravity? Can individuals learn to throw accurately in such scenario? Moreover, individuals with throwing expertise, like baseball pitchers, might show different features in their release/performance relation. Given that, it would be interesting extending the results presented by Tommasino and colleagues. One potentially fruitful direction to explore would be to characterize throwing strategies of participants with expertise in different sport disciplines. Moreover, it would also be interesting to investigate not only throwing of real balls but also throwing in a virtual environment, where it is possible to systematically control the dynamics of the ball and thus investigate learning of new complex motor skills.

The aim of the work described in this chapter was to develop a low-cost and easily deployable system for studying throwing actions, both in an experimental setup and in a matched virtual environment, of different groups of sport experts. In this chapter, the development of the different components of such a system are described first. The issues encountered during the development and the solutions found to address them are also discussed. Finally, the results of experimental tests for validating the system are presented. Concerning standard motion capture systems, i.e. marker-based, one limitation impeding their widespread application and easy deployment in field studies is that they are expensive

and require a controlled and large environment to be placed in. Also, placing markers on the participants body may be extremely time consuming. Therefore, to overcome these limitations we decided to exploit the motion capture capabilities embedded in a VR headset and tracking devices.

One of our goals was to investigate throwing actions in VR. The rationale behind this approach is the possibility of exploring learning and adaptive behaviors in altered dynamics conditions. VR indeed allows to test participants in a realistic and controlled environment, and it provides the researcher with the chance of altering the dynamics of the environment, such as different gravity or drag values. In addition, thanks to VR each throw with the same initial conditions will provide the exact same repeatable outcome, i.e., there are no abrupt and unpredictable distractions or noises.

Finally, an unexpensive VR system is also portable, easy to install and therefore could be used outside the traditional laboratory scenario, allowing testing large and diverse populations.

Our system was developed using a commercial VR platform (HTC Vive) and it was designed to investigate throwing of both real and virtual balls. A VR environment reproducing a real experimental setup for studying throwing was developed. The setup consists of a room, a target board, and a ball. Since ball throwing actions are uniquely determined by release parameters and impact parameters, a critical design goal was to achieve an accurate estimation of these parameters. Moreover, realistic throws require hand-ball interaction, therefore a model of such interaction is required. As proposed solutions, we developed and compared several methods to estimate release and impact parameters. The methods are based on a micro-switch integrated in the VR system to detect the ball release event and on algorithms to improve release parameters estimation. As the release event detection by the micro-switch is not always accurate, a mismatch between VR

throws and real ones was observed. Then, different software solutions were investigated to obtain more reliable estimations of release parameters and consequently impact parameters.

3.2. Methods

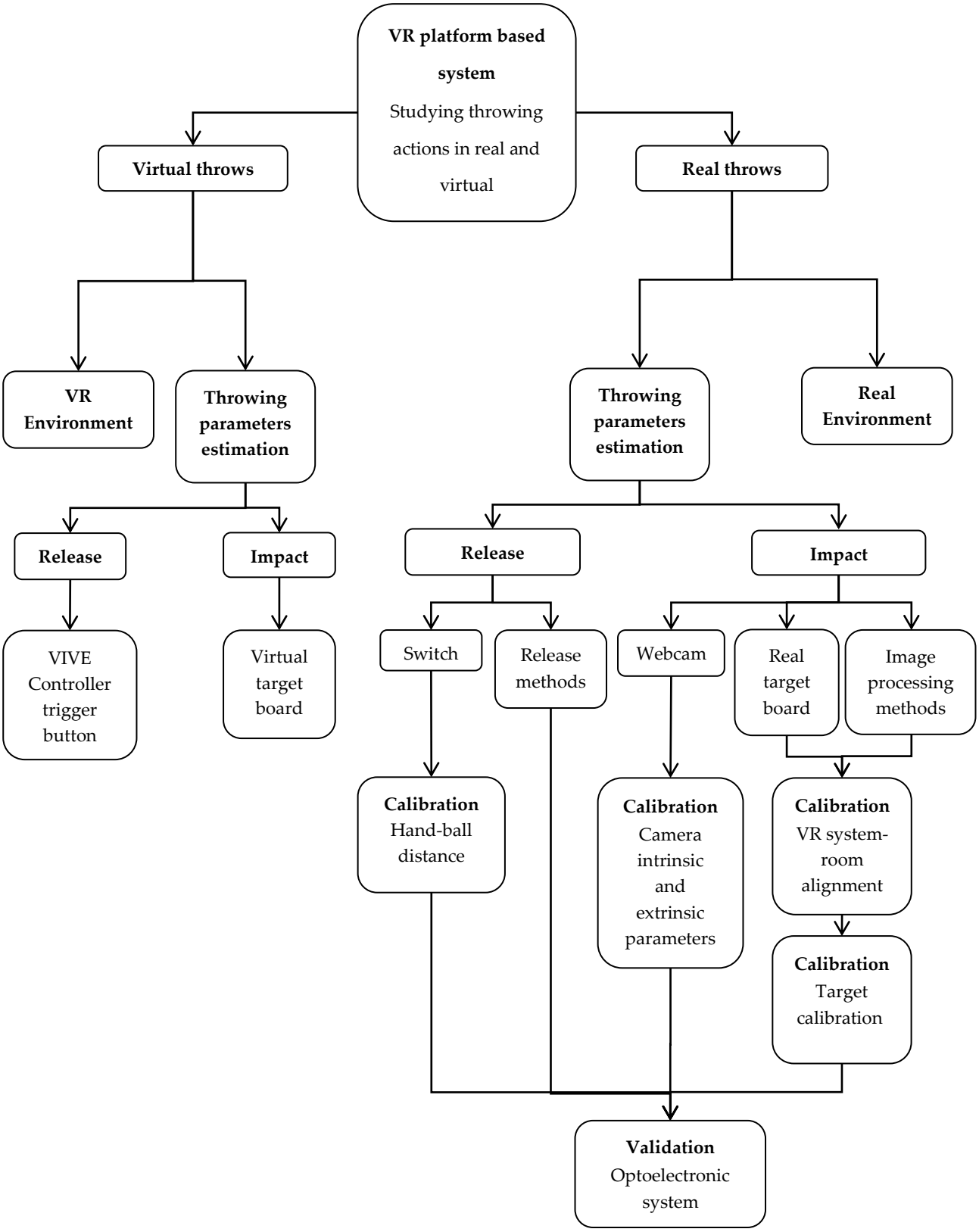

Figure 3.1. Overview of the methods. A schematic representation of the system and the developed procedures and methods.

The developed system (Fig. 3.1), based on a commercial VR platform, allows to study motor strategies during ball throwing actions, as the kinematics of the throwing hand can be recorded with the embedded motion capture system. Several methods have been developed and integrated in the system to simulate throws both in real and virtual environments. Two operation modes have been implemented: Virtual Throws, to perform the throwing action in a virtual scenario and with a virtual ball, Real Throws, to record the participant throwing a real ball towards a real target. For the first operation mode a virtual environment was developed, release events were detected by the trigger button of the VR system hand-held controller while the impact events were computed in the virtual environment as the time taken by the virtual ball to impact on the virtual target. For the second operation mode, a real experimental setup was constructed matching the virtual one. Throwing parameters were estimated by detecting the release events using a switch integrated in the controller and placed on participant's finger and using a novel estimation method, which takes into account hand-ball interaction. Impact parameters were estimated by detecting the ball impact on a target board through a webcam synchronized with the VR system and using an image processing procedure based on a MATLAB toolbox. Parameters detection for the second operation mode required several calibration procedures to estimate real ball-hand distance, to align the real room and the real target with the motion capture system, and to calibrate webcam parameters. The methods developed for real throws were validated with a second standard optoelectronic motion capture system which simultaneously recorded throwing actions.

3.2.1. Experimental setup

The setup is based on a VR platform which includes motion capture sensors to record hand kinematics, and a headset to display the virtual environment. The commercial VR platform was integrated with several devices to allow recording of throws of virtual and real balls and to estimate the kinematic parameters that characterize the throwing task.

3.2.1.1. VR system (HTC Vive)

Figure 3.2. Htc Vive system. The system consists of the headset to display VR, 2 base stations, 2 controllers and 2 trackers for motion capture.

The Vive system (HTC Europe Co. Ltd, Slough, Berkshire, U.K) (Fig. 3.2), includes two base stations emitting infrared pulses which create a tracking area where the positions of headset, the controllers and the trackers can be tracked with sub-millimeter precision. The headset (Fig. 3.3A) displays the interactive virtual scenario designed for the virtual throwing task, at a refresh rate of 90Hz, with a 110° field of view, and with an image resolution of 1080 × 1200 pixels for each eye. For the experiments we used one Vive controller (Fig. 3.3B) and one Vive tracker (Fig. 3.3C). In the Virtual Throws operation mode, the participant wears the headset to visualize the virtual environment, hold the controller is hand and uses it to pick up, move and release the virtual ball. The tracker is placed on the dorsum of the participant's hands to track the throwing movement. In the following, coordinates of the tracker position in the Vive reference system are indicated by a superscript v (e. g. $\boldsymbol{x}_t^v$

indicates the 3D vector representing the position of the tracker in Vive coordinates). In the Real Throws operation mode, the headset is not worn by the participant, the controller is placed on participant's upper arm and used to detect pickup and release events, while the tracker is placed on the dorsum of the participant's hand and is used to track the position of the real ball, which had a fixed position with respect to the tracker when is gripped by participants.

The Vive system was developed integrating SteamVR (*SteamVR su Steam*), a commercial tool for interfacing different VR devices, with Unity (*Unity Real-Time Development Platform | 3D, 2D VR & AR Engine*), a commercial platform for creating and operating interactive real-time 3D content, running on a personal computer. Unity allows developers to create immersive and interactive VR environments thanks to an intuitive interface and the possibility to create or modify object behaviours using C# scripts. Scripts can be used to implement new gameplay features, to respond to input from the player, to trigger game events, to create graphical effects or control the physical behaviour of objects in the game.

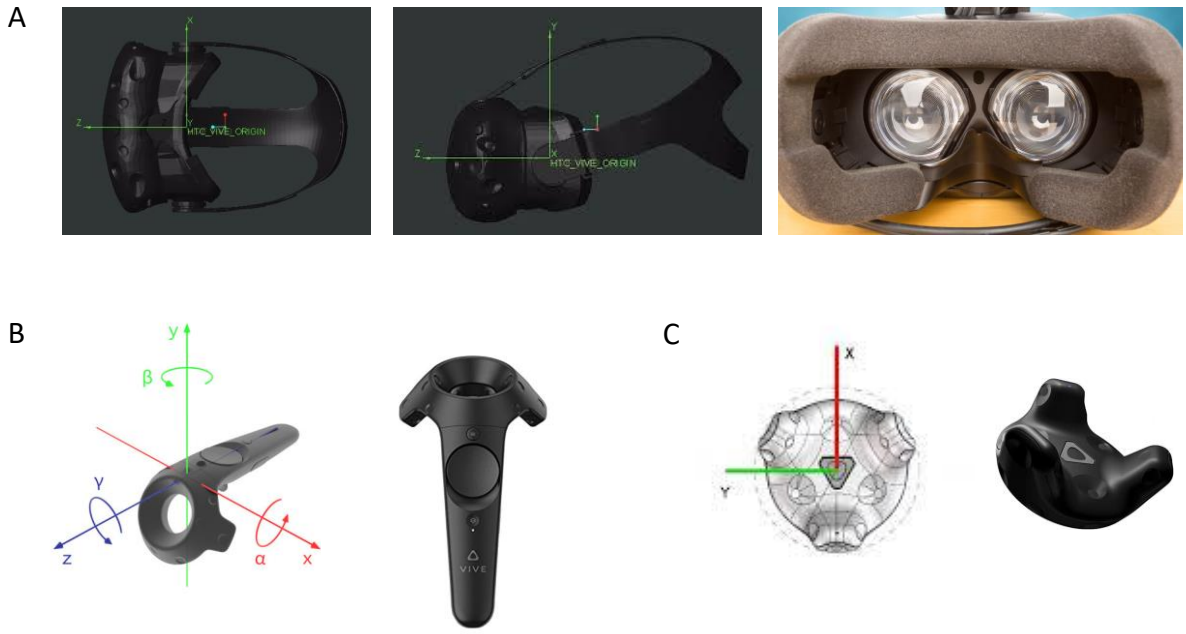

Figure 3.3. HTC Vive hardware components. (**A**) Headset, (**B**) Controller, (**C**) Tracker.

3.2.1.2. Micro-switch

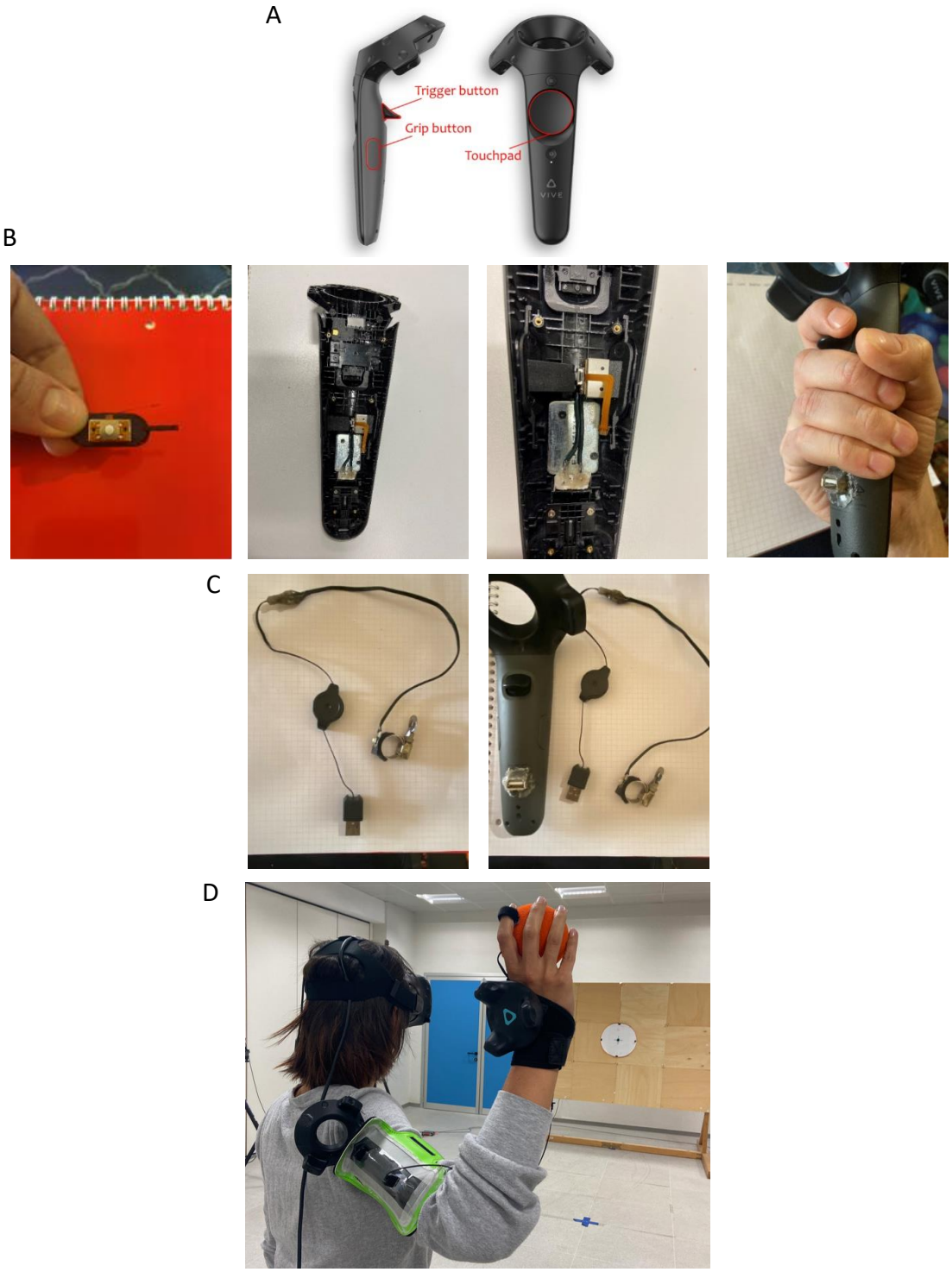

Figure 3.4. Development of ball release detection using a micro-switch integrated in the controller. (**A**) Controller buttons representation. (**B**) USB port integration. (**C**) Micro-switch and controller. (**D**) Micro-switch usage.

A micro-switch placed on participant's index finger pad was used to detect ball release during throwing actions in Real Throws operation mode. The sensor has been integrated in the controller through a connection to the grip button (Fig. 3.4A). An USB connector has been welded to the grip switch wires in the controller electronic board in order to use the controller integrated electronics to operate and communicate wirelessly with the PC (Fig. 3.4B). A 3.1 mm high light touch micro-switch which operates with low contact forces (0.5 N threshold) was placed on participant's finger pad with a velcro strap (Fig. 3.4C) and was connected through a spring-loaded extendable cable to the integrated controller placed on participant's arm (Fig. 3.4D). The extendable cable allows to adjust the length of the cable according to participant's arm length.

3.2.1.3. Webcam

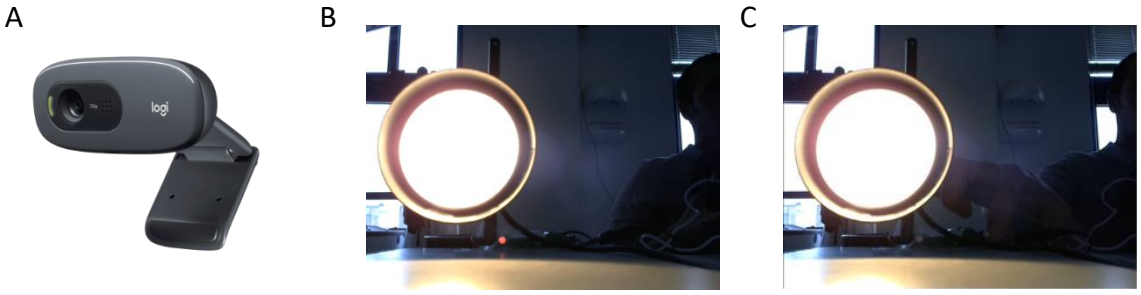

Figure 3.5. Webcam and synchronization delay time calibration procedure. (**A**) c270 Logitech webcam. (**B**) LED on after ball pickup event (hardware switch) and before the release event. (**C**) LED off during ball release event.

A low-cost webcam (c270 Logitech, 720p, 30 fps, Fig. 3.5A) has been integrated in the system, for the Real Throws operation mode, to detect ball impact on target board and to estimate ball impact to target centre distance. The Webcam recording process is based on the open-source SDK *CaptureManager* (*GitHub - Xirexel/CaptureManagerSDK*). The webcam integration into the system VR platform allows to record synchronized video triggered by the virtual ball pickup event and until the impact event. Both the events are related to the

virtual environment, and they are defined as the instant in which the virtual ball is picked up thought the switch placed on subject's finger (pickup) to the instant in which the virtual ball impacts with any virtual object (target, walls, floor, roof) in the virtual environment.

The development process included several tests aimed at finding the software configuration with the best performances defined as the amount of PC hardware resources used and the temporal delay between trigger event and video start recording. A validation dataset (22 trials) recorded with the optoelectronic system (see below) has also been performed in order to estimate impact spatial and temporal error estimations. In particular, using a process integrated in the Unity platform instead that an external process triggered by TCP communication allows to minimize the temporal delay between the trigger event and the start of recording. Some attempts were performed to record 3 webcams in parallel, but the amount of required CPU resources exceeded PC hardware capabilities. Moreover, in order to minimize the delay between the trigger events (pickup, impact) and the webcam recordings timing, the library has been modified to allow a continue streaming of the data. In particular, the modified version of the C# library *CaptureManagerUnityVideoAndAudioRecorder*.dll of the SDK starts a continuous video streaming from the webcam, at the beginning of the experiment and saves on the PC only when the events are triggered. The continuous streaming allows to solve the delay issue, recurring every trial, due to the time required to start and stop the recording process of the webcam.

A testing setup was developed, and 30 trials have been performed to evaluate the delay in video recording procedure (Fig. 3.5). The setup, consisting of the Vive system, the webcam and a LED, made it possible to calculate the difference between Unity and webcam data acquisition times. In particular, a LED was connected to the hardware switch in order to remain on until the switch is triggered (Fig. 3.5B switch turned on, 3.5C switch turned off). At the beginning of every trial the webcam starts to record a video of the LED connected to the switch. When the switch is triggered, the LED turns off and the temporal difference

between the pickup event recorded by Unity and the LED turning off frame can be evaluated.

3.2.1.4. Standalone cameras

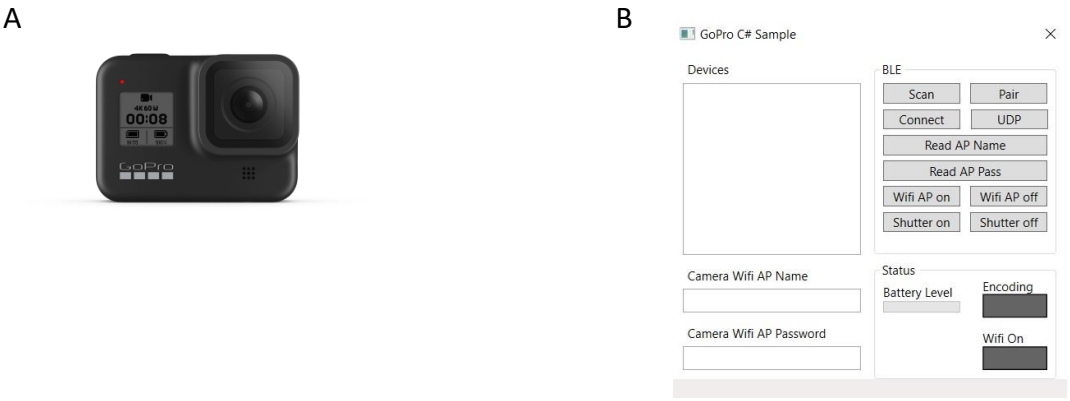

Figure 3.6. Standalone cameras. (**A**) GoPro Hero 8. (**B**) User interface.

Two standalone high-definition cameras (GoPro Hero 8, 1080p, 120 fps, Fig. 3.6A) have been integrated to record thrower's whole-body kinematic during the throwing action of both the virtual and real operation mode for an offline analysis. The cameras have been synchronized with the system through the Open GoPro API. In particular, the C# script based *GoProCSharpSample* demo (*GoProCSharpSample : Open GoPro*, s.d.) has been modified to discover, pair, connect and UDP communicate to the cameras via Bluetooth LE (BLE) through the UI (Fig. 3.6B).

3.2.1.5. Virtual environment and matching real experimental setup

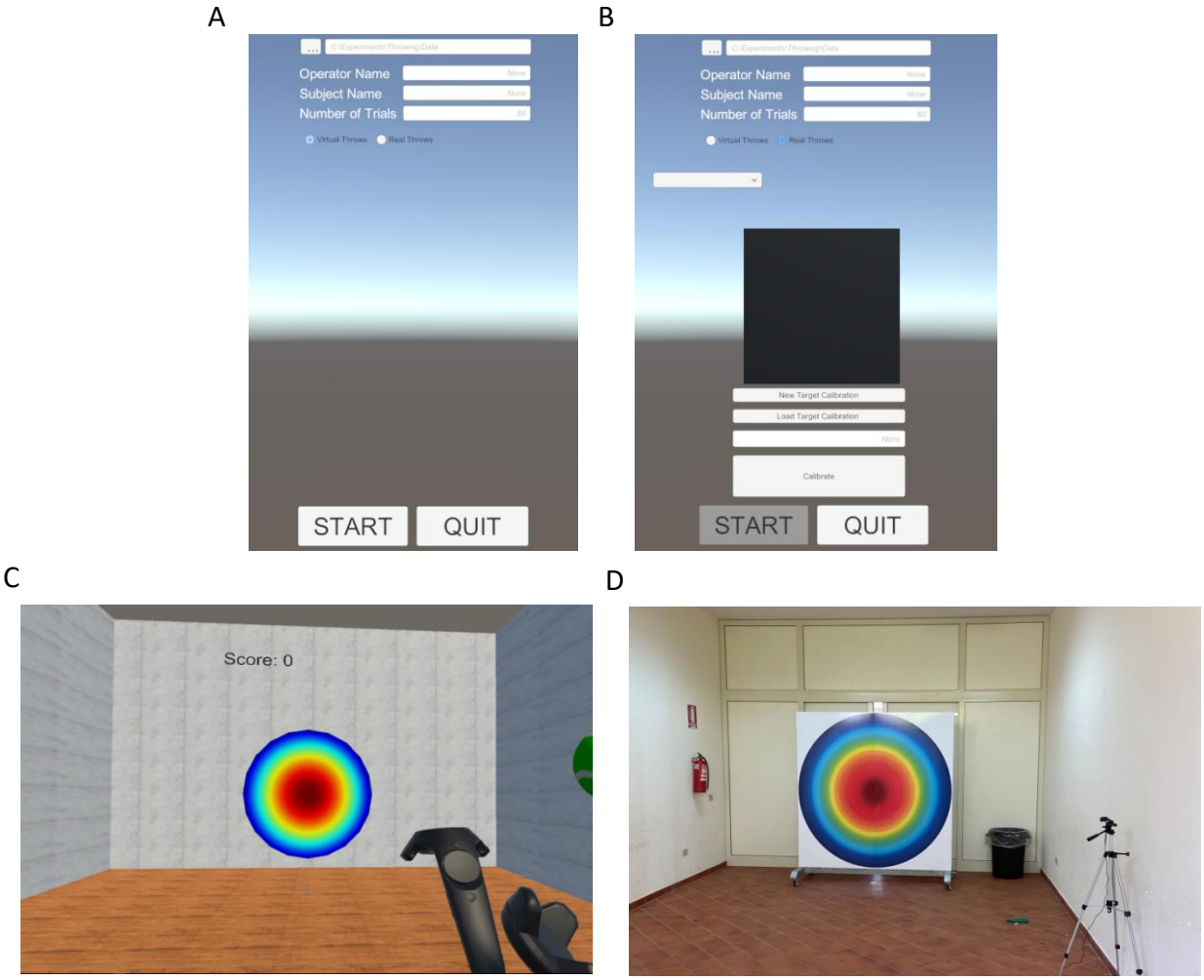

Figure 3.7. Environments and UI. (**A**) Virtual Throws operation mode UI selection. (**B**) Real Throws operation mode UI selection. (**C**) VR environment. (**D**) Real experimental setup matching the VR environment.

Two different environments have been developed, one for each operation mode. A user interface (UI) in Unity allows to select and define the operation mode, Virtual Throws (Fig. 3.7A) or Real Throws (Fig. 3.7B) and to set some of the experimental parameters as the saving directory, operator and participant names or IDs, and number of trials. The Unity platform is engaged in both operation modes to record hand kinematics and temporal events. In the VR environment (Fig. 3.7C), Unity also renders the virtual scenario and its

components, which consist in a target disc of 1 m radius placed at 6 m from the thrower with the centre of the disc at a height of 1.2 m from the floor, a ball of 0.045 m radius and a room.

When Real Throws is selected from the developed UI, it is possible to choose webcam parameters used during the experiment and to collect data for the real target calibration (see 3.2.2.1.2). The real experimental setup matching the VR environment (Fig. 3.7D) consists of a target board with 1 m radius target disc located at 6 m in front of the thrower at a height of 1.2 m from the floor and a ball with 0.045 m of radius. To create consistent lighting conditions regardless of the weather or the time of the day, all the windows in the room have been covered with black panels and 2 high-intensity LED light sources have been placed on the side of the target to supplement the room ceiling artificial illumination. The intensity and positioning of the LED light sources have been optimized to have a sufficient illumination of the target to ensure clear images in the webcam recordings resolution and adequate frame rate.

3.2.2. Experimental protocol

Specific experimental protocols to be used with the system has also been developed to investigate throwing actions in both real and virtual environments. According to these protocols, participants perform both throwing operation modes in the same experimental session.

In the Virtual Throws scenario, participants stand at the center of the room, wearing the headset and the motion tracking sensors (tracker) on the right hand's dorsum. The controller is held with the same hand and is used to pick up and throw the ball. When the controller (i.e. the hand) reaches close to the virtual ball, placed in a known and visible position for the participants, the participant can pick up the ball by pressing the controller trigger. Once the

ball is picked up, it remains attached to the center of the controller. To release the ball the participant must release the trigger. Then, the ball moves affected by gravity in VR. Initial position and velocity of the ball are taken from the controller position and velocity at the time of release. Once a collision is detected in the VR scenario, i.e., the ball contacts the target board or the floor/walls of the room, an impact event is saved and the position of the ball at that instant is considered as ball impact position.

In the Real Throws mode, participants grasp a real ball, which however is not tracked. At the time of pick-up, the participant presses the micro-switch onto the real ball and the Unity software starts the trial. The release event is gathered as the instant at which the switch is released, and the ball launched. Then, the ball flies freely in the laboratory. The time of impact, i.e. when the ball touches the target board (or the floor/walls), is identified by the webcam video offline. In this scenario, the ball trajectory is estimated offline from release and impact parameters. Therefore, accuracy of release and impact parameters is crucial to identify the trajectory the ball during its flight. Several methods have been compared to provide the best estimation of the release parameters. Impact detection has been performed with a webcam. All these estimates have been compared with real ball trajectories recorded with a standard motion capture systems to assess the validity of the approach.

3.2.3. Throwing parameter estimation

In the Virtual Throws operation mode, virtual ball pickup and release are detected by the trigger button on the hand-held controller. When the thrower presses the trigger button, the virtual ball attaches to the controller. Release parameters, as ball position and velocity are estimated from the samples of the position of the controller recorded until the time at which the trigger is released. Since the ball attaches to a specific position of the controller held in the participant's hand (Fig. 3.13) the throws are not natural and, because of the distance between the hand and the virtual ball, a new throwing strategy with the controller must be

learned. The ball trajectory from release to impact is simulated with Unity. Impact parameters are estimated from the simulated ball trajectory. A Gaussian error function has been implemented to provide the participant with a score related to the ball distance from the centre. A tracker is placed on the dorsum of the thrower's hand to be consistent with the Real Throws operation mode.

In Real Throws operation mode, real ball pickup and release are detected by the micro-switch placed on thrower's finger. Differently from the Virtual Throws operation mode, release parameters are estimated from the kinematic data from the tracker placed on the dorsum of the thrower's hand, when the switch is released. To estimate reliably the release position, a calibration procedure is required to estimate the position of the centre of the real ball in the tracker coordinate reference system (see 3.2.2.2.2). Impact parameters are estimated from the synchronized webcam which records the final part of the trajectory and the impact on the target. An image processing procedure allows to estimate ball impact point and distance from the centre of the target.

3.2.3.1. Impact parameters

While for the Virtual Throws operation mode, impact parameters (position and time) are estimated from the virtual simulated ball trajectory, for the Real Throws operation mode, impact parameters estimation is based on the synchronized webcam and an image processing procedure to estimate impact parameters from the acquired videos. The developed method, based on the Matlab Image Processing toolbox, requires several calibration procedures to achieve an accurate and reliable estimation of the ball impact parameters. In the next paragraphs the image processing and the developed calibration procedures are described.

3.2.3.1.1. Camera calibration

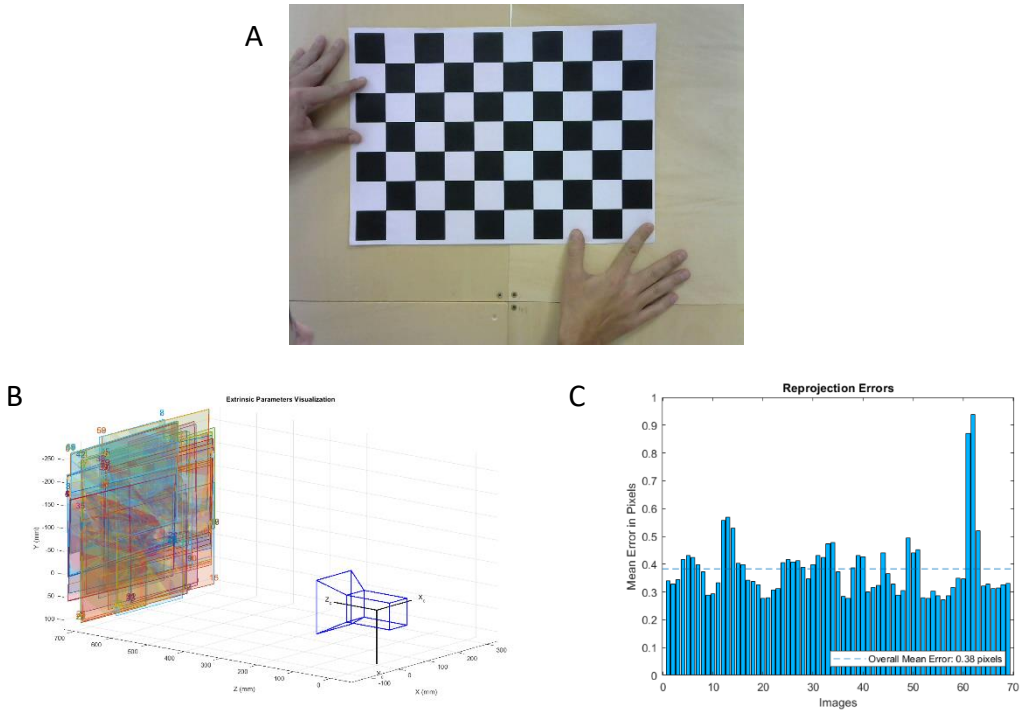

Figure 3.8. Camera calibration. (**A**) Calibration pattern. (**B**) Extrinsic camera parameter visualization. (**C**) Average reprojection error in each calibration image.

The camera calibration procedure estimates camera parameters, as intrinsic camera parameters (internal characteristics of a camera, such as the focal length, the optical center, lens distortion coefficients) and extrinsic camera parameters (position and rotation of the camera with respect to the calibration pattern) by using images that contain a known calibration pattern. The calibration of the intrinsic parameters is required to remove lens distortion effect from the image and it is performed only the first time a new camera is used. The webcam is placed in front of a planar surface perpendicular to the axes between the plane and the webcam, at a distance of 0.7 m. A video of the calibration pattern placed in different positions on the planar surface is recorded. A typical calibration pattern is an asymmetric checkerboard (Fig. 3.8A), where one side contains an even number of squares, both black and white, and the other contains an odd number of squares. The corners of the squares that lie inside the pattern are used as the control points. These corners can be detected on the 2-D calibration image automatically by using a corner detector algorithm.

By assuming the lower-right corner point of the top-left square of the checkerboard is the origin, we can also determine the 3-D world coordinates of the points by using the square size of the checkerboard. 69 frames have been selected from the video to calibrate camera parameters. To evaluate the accuracy of the estimated parameters, it is possible to plot relative camera and calibration pattern location (extrinsic parameters, Fig. 3.8B) and calculate the reprojection errors (Fig. 3.8C). Extrinsic parameters estimation allows to discover obvious errors in the calibration by plotting relative locations of the calibration pattern in the camera's coordinate system (Matlab function *showExtrinsics*). The extrinsic parameters consist of a rotation matrix, R, and a translation vector, t. The origin of the camera's coordinate system is at its optical centre and its x- and y-axis define the image plane. The intrinsic parameters include the focal length, the optical centre, also known as the principal point, and the skew coefficient. Radial distortion occurs when light rays bend more near the edges of a lens than they do at its optical centre. The smaller the lens, the greater the distortion. Tangential distortion occurs when the lens and the image plane are not parallel. The tangential distortion coefficients model this type of distortion reprojection errors provide a qualitative measure of accuracy. A reprojection error is the distance between a pattern key point detected in a calibration image, and a corresponding world point projected into the same image (Matlab function *showReprojectionErrors*).

3.2.3.1.2. Target calibration

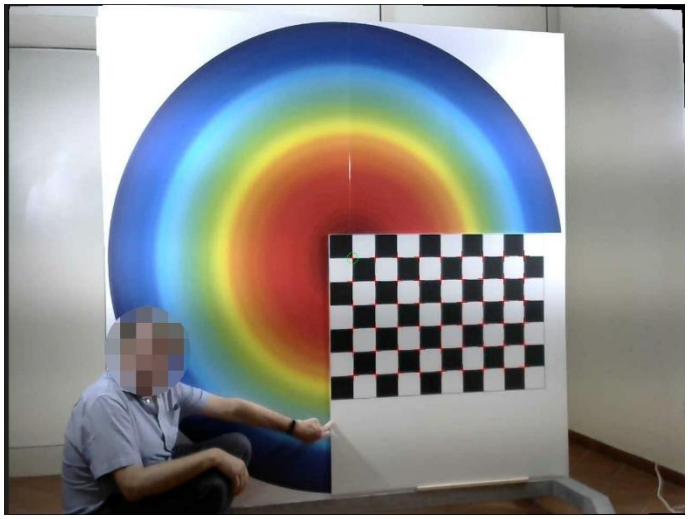

Figure 3.9. Target center calibration

A procedure has been developed to estimate the position of target centre with respect to the webcam. Target calibration is performed every time the camera or the target is moved. The procedure can be performed at the beginning of each session through the initial menu or, if no changes on webcam-target placement has occurred, a stored calibration can be loaded. The procedure based on the Matlab toolbox allows to record a video from the webcam of the target and the calibration pattern (10x10 cm) placed with the first corner of the pattern on the target centre. A 1 m radius circle is than plotted on the undistorted image and then the image is distorted according to the camera intrinsic parameters.

3.2.3.1.3. Room calibration

To align the VIVE coordinate system to the laboratory an offline calibration procedure has been developed. The calibration is a roto-translation of the data recorded in the VIVE coordinate reference system with respect to world (laborarory) coordinate reference system. Basically, it consists of recording the VIVE coordinates of the tracker at a known position and the VIVE coordinates of the target. To perform the room calibration the operator needs to press the button "r". A red text appears in the virtual environment above the target to alert the user. While the headset is placed on the floor in the zero position (which is

consistent with the virtual one thanks to the steamVR room calibration) and the tracker is placed on the floor 1 meter far away from the zero along the line which passes from the zero position and the target centre projection on the floor, the subject press and release controller trigger in order to start and stop position recording.

3.2.3.1.4. Ball trajectory detection

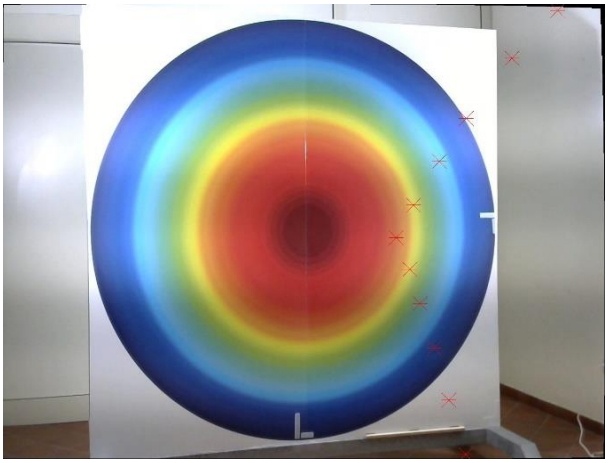

Figure 3.10. Movement recognition

An offline procedure allows to detect the ball trajectory from the video recorded by the webcam. Using the Matlab Computer Vision toolbox, using Gaussian mixture models, it is possible to determine whether individual pixels are part of the background or the foreground in order to compute a foreground mask (Matlab function *vision.ForegroundDetector*) and to compute statistics for connected regions in a binary image (Matlab function *vision.BlobAnalysis*) in order to define centroid, bounding box, label matrix, and blob count. To perform the foreground computation 50 frames and an initial model variance of 60 have been used for training background model (Fig. 3.10).

3.2.3.1.5. Estimation of ball impact position and distance from the target centre

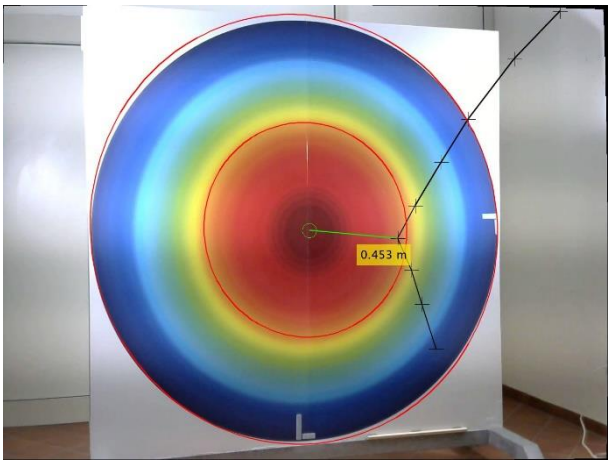

Figure 3.11. Impact detection

To estimate the impact point within the points of the ball trajectory detected with the Matlab Computer Vision Toolbox, an offline algorithm has been implemented. The algorithm considers a maximum number of points n from the first detected one, defines a set of n-1 vectors passing through each pair of detected points. The impact point is selected as the point at with there is the largest angular change between consecutive vectors. To prevent detection errors due to the ball bouncing on the floor after target impact, a procedure was implemented to consider only a maximum set n of detected point (n = 12) within a maximum distance d from the centre of the target ($d \leq 1$ m). The remaining detected points are not included in the impact detection algorithm. (Fig. 3.11). The distance between the impact point and the target centre is estimated from the laboratory coordinates of the points, estimated with the Matlab function *pointsToWorld*, which takes into account the intrinsic camera parameters (see 3.2.2.1.1) recorded and the extrinsic parameters (see 3.2.2.1.2).

3.2.3.2. Release parameters

Ball trajectories are characterized by several parameters: release time, position and velocity, impact time and position. Therefore, it is key to estimate ball release position and velocity

of the throwing action, especially for the Real Throws where there is no tracking of the ball. In the Virtual Throws operation mode, the virtual ball is attached to the controller centre, after pick-up. The ball release event time is detected as the time of release of the trigger button, and ball release position is estimated from the controller position and orientation at time of release. Instead, in the Real Throws operation mode, we want to estimate the ball release position and velocity from the tracker position and velocity at the time of release. The position of the ball with respect to the tracker has been calibrated with the procedure described below (see 3.2.3.2.1). The release event is detected by the switch connected to the controller, when the finger is lifted from the ball (see 3.2.3.2.2). Estimation of ball position and velocity at time of switch release is gathered from position and orientation of the tracker.

However, such estimated ball position and velocity, derived from tracker by the SteamVR software library, were found not to be reliable. In particular, the velocity of the tracker was different from the velocity computed through deriving position data. To test whether the initial conditions of the ball trajectory (i.e. position and velocity) were correct, we simulated the ball trajectory and compared its arrival location with the impact position of the real ball detected by the camera.

Thus, we decided to compute the initial ball velocity deriving its position online through a buffer of position data after the release event (see 3.2.3.2.3). However such approach was not sufficient to achieve an accurate estimation of the velocity. Several attempts have been made to achieve an accurate estimate of the velocity of the ball at release, given hand position and orientation. At first, we assumed that the release event detected by the switch was not correct. Therefore, we tested whether an earlier instant with respect to the release time would improve the accuracy of the estimation (Single Delta Method, see 3.2.3.2.4). Then, we decided to include drag into our simulation of the trajectory as we were indeed comparing a real ball (affected by drag) and a simulated ball path moving with constant accelerated motion. To this end, we estimated the drag in the room with the help of a

marker-based motion capture system, Optitrack (see 3.2.3.2.5). In all following simulations, air drag in ball trajectory motion is included.

Finally, we compared 4 methods to estimate release events and their resulting ball trajectories

1- Detection of fingers lifting by the micro-switch (Switch, see 3.2.3.2.6)
2- Detection of a zero in the acceleration of the ball in the vicinity of the switch release event (Zero Acceleration, see 3.2.3.2.7)
3- Simulation of the ball motion in the hand along different axes of a reference system attached to the hand starting at different times before the instant detected by the micro-switch (Multi Delta, see 3.2.3.2.8). The simulation assumes that the ball starts moving at different instant on each axis and that before the final release both hand acceleration and gravity are acting on the ball. Two optimizations have been considered:
    a. A unique set of three time delta was optimized for all trials (General Multi Delta).
    b. A set of three time delta was optimized for each trial (Individual Multi Delta).

We tested and compared the reliability of the methods on a dataset consisting of 18 throws performed by a thrower. Validation has been performed tracking the ball with a marker-based motion capture system.

3.2.3.2.1. Ball position calibration at pick up

Figure 3.12. Hand-ball distance calibration. The figure shows the calibration procedure required to estimate the participant-dependent distance between the ball and thrower's hand.

In the experimental setup, the real ball is not tracked during its flight. Ball position until the time of release is determined from the position of the tracker on the dorsum of the hand (assuming a fixed position of the ball with respect to the hand before release) and at the time of impact from the video recorded by the webcam as the position of the ball on the target board. In order to accurately estimate such positions and use them to estimate the ball trajectory during ball flight, a calibration procedure has been developed.

The hand position is tracked with the tracker device (see above). When the subject grasps the ball with their hand the ball has a constant offset with respect to the tracker attached to the dorsum of the hand (i.e. a fixed vector $\mathbf{x}_b^t$ indicating the ball position in the reference system of the tracker, indicated by the superscript t) depending on the shape and size of the hand. This offset is measured at the beginning of the experimental session. Then it is used to identify the position of the ball in the virtual environment (i.e., in Vive coordinates, $\mathbf{x}_b^v$). Subjects are instructed to grasp the ball always in the same way.

The calibration procedure works as follows. The real ball is placed in a position that can be measured using the Vive controller (see Fig. 3.12). Let be $\boldsymbol{x}_b^v$ such position. The position of the tracker is $\boldsymbol{x}_t^v$. The position of the ball in tracker coordinates will be

$$\boldsymbol{x}_b^t = R_v^t(\boldsymbol{x}_b^v - \boldsymbol{x}_t^v)$$

Equation 3.2. Virtual ball position estimation with respect to tracker position (offset).

where R_v^t is the rotation matrix which depends on the tracker orientation. Such offset is assumed constant and ball position in Vive coordinates during the trial will be represented as follows

$$\boldsymbol{x}_b^v = R_t^v \boldsymbol{x}_b^t + \boldsymbol{x}_t^v$$

Equation 3.3. Virtual ball position estimation until release event.

3.2.3.2.2. Analog micro-switch to detect release event

The analog switch estimates the time of ball release as switch release time and the position and velocity of the ball at release from the trajectory of the ball (tracked either by the Optitrack motion capture system for the validation experiments, see below, or by the Vice tracker attached to the dorsum of the hand and using the ball position calibration, see above) until that time. The position $\boldsymbol{x}_t^v$ and orientation $\boldsymbol{q}_t^v$ (Euler angles for Optitrack, quaternions for Vive) of the ball from pickup to 2 seconds after ball impact time $\boldsymbol{t}_{imp}$ are considered. An offline algorithm extrapolates Euler angles from quaternions (for Vive only), resamples and filters the samples (low pass 5th order Butterworth filter, cutoff frequency 10 Hz). The rotation matrix is extrapolated from the Euler angles and the position of the ball $\boldsymbol{x}_b^v$ in Vive coordinates is computed using the ball position offset recorded experimentally during hand-ball calibration procedure (see 3.2.3.2.1) and rotating frame by frame ball position

offset according to the tracker rotation matrix. Finally, system rotates virtual ball position, tracker position and rotation matrix in order to obtain a clockwise reference system.

3.2.3.2.3. SteamVR velocity estimation error

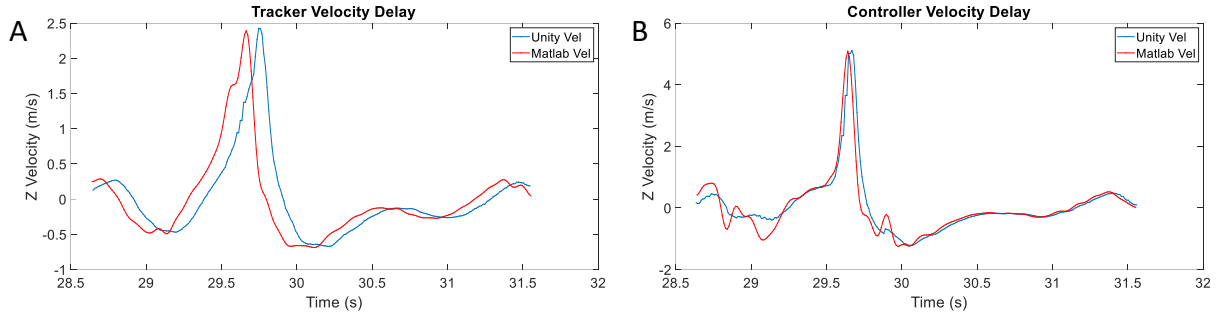

Figure 3.13. Controller and tracker velocity estimation. (**A**) Online tracker estimated velocity profile (blue line) and online reconstructed velocity estimated with Matlab from positions (red line). (**B**) Controller velocity estimations.

A systematic error has been identified using the SteamVR library. Using the method velocity of the class *SteamVR_Controller.Device*, tracker estimated velocity has a delay of 0.1 s with respect to the velocity estimated offline as the derivative of the position (SteamVR method *mDeviceToAbsoluteTracking* of the class *TrackedDevicePose_t*) with respect to time, while the controller has a delay of 0.022 s. In Fig. 3.13 it is possible to see the differences in the velocity profiles of the tracker (Fig. 3.13A) and of the controller (Fig. 3.13B) with respect to the velocity estimated offline with Matlab using the position samples. To improve velocity estimation, we implemented a new online method in Unity to estimate tracker velocity from tracker position. A buffer of 20 position samples (at 90 Hz sampling frequency) is used to estimate ball velocity at release. Position samples are stored in the buffer until the release event. After release, the ball disappears for 10 frames (i.e., during the trajectory estimation computation) and reappears after 10 frames in the estimated position. In Eq. 3.1A the virtual ball velocity $\dot{\boldsymbol{x}}(\boldsymbol{i})_b^v$ for the ith frame is estimated as the position numerical derivative. Where $\boldsymbol{x}(\boldsymbol{i}+\boldsymbol{1})_b^v$ and $\boldsymbol{x}(\boldsymbol{i}-\boldsymbol{1})_b^v$ are respectively the position of the ball at the ith+1 and ith-1 frame, while $\Delta\boldsymbol{t}$ is the temporal delta between each frame. Then, the position $\boldsymbol{x}(\boldsymbol{i})_b^v$ is estimated for

each axes component of $\boldsymbol{x}_b^v$ (Eq. 3.1B) at the given time t, which is in this case 0.111 s after the release (10 frames at 90 Hz sampling rate) (Eq. 3.1C).

$$\dot{\boldsymbol{x}}(\boldsymbol{i})_b^v = \frac{\boldsymbol{x}(\boldsymbol{i}+\mathbf{1})_b^v + \boldsymbol{x}(\boldsymbol{i}-\mathbf{1})_b^v}{2 * \Delta \boldsymbol{t}} \quad \text{A}$$

$$\boldsymbol{x}_b^v = [x_{comp}, y_{comp}, z_{comp}] \quad \text{B}$$

$$\boldsymbol{x}(\boldsymbol{i})_b^v = \begin{cases} x_{comp}(i_{rel}) + \dot{x}_{comp}(i_{rel}) * t \\ y_{comp}(i_{rel}) + \dot{y}_{comp}(i_{rel}) * t \\ z_{comp}(i_{rel}) + \dot{z}_{comp}(i_{rel}) * t + g * t^2 \end{cases} \quad \text{C}$$

Equation 3.1. Online velocity estimation method. Equations from position to velocity implemented online to overcome the delay of the SteamVR tracker velocity estimation.

3.2.3.2.4. Identifying release event before fingers lifting

To study the effect of release timing on ball trajectories an offline simulation method has been developed. The method allows to simulate the trajectory using as release parameters the values recorded from 1 to 9 frames (frame: 0.011 s) before the hardware switch release (Single Delta Method).

3.2.3.2.5. Ball trajectory simulation with air drag

To improve the accuracy of the ball trajectory estimated from the position and velocity of the ball at release, air drag was included in the ball motion equations. An air drag coefficient has been estimated from a validation dataset of 22 trials performed from a single thrower. We selected, in a range of values from 0.1 to 1, the drag air coefficient that allows to simulate the trajectory with minimal impact point error on the target with respect to the real impact point. Trajectory simulation starts at 0.1 s after release time as detected from the switch $\boldsymbol{t_r}$

and ends when ball arrives at target plane (x-z), placed at 6 meters from thrower. We used the equation of motion in a linear resisting medium for estimating the drag (Eq. 3.4).

$$T = \frac{gt}{v_0} \qquad \epsilon = \frac{kv_0}{g} \qquad \epsilon T = kt$$

$$\boldsymbol{R} = \frac{\hat{\boldsymbol{v}}_0}{\epsilon}\,(1 - e^{-\epsilon T}) + \frac{1}{\epsilon^2}\,(1 - \epsilon T - e^{-\epsilon T})\hat{\boldsymbol{J}}$$

$$\boldsymbol{V} = \frac{\hat{\boldsymbol{v}}_0}{\epsilon}\,e^{-\epsilon T} + \frac{1}{\epsilon}\,(e^{-\epsilon T} - 1)\hat{\boldsymbol{J}}$$

$$\boldsymbol{R} = \frac{g\boldsymbol{r}}{{v_0}^2}$$

Equation 3.4. Equation of motion in a linear resisting medium.

Where $\hat{\boldsymbol{v}}_0$ is the initial dimensionless velocity of projection. $\boldsymbol{R}$ and $\boldsymbol{V}$ are respectively the dimensionless position and velocity vectors at time $\boldsymbol{t}$. $\boldsymbol{r}$ is the dimensional position vector at time $\boldsymbol{t}$ and $\boldsymbol{k}$ is the air resistance coefficient constant.

3.2.3.2.6. Analog micro-switch with air drag

This method, based on the method analog micro-switch, simulates ball flight from t_r to t_{imp} using the equation of motion in a linear resisting medium used for estimating the air drag coefficient.

3.2.3.2.7. Searching for a zero in ball acceleration to determine release event

The Zero Acceleration method searches the time, in a range from 222 ms before t_r to 111 ms after, at which the acceleration of the tracker is equal to zero. From t_r to t_{imp}, trajectory is

simulated using the equation of motion in a linear resisting medium used for estimating the air drag coefficient.

3.2.3.2.8. Multi delta method: ball motion onset time is not coincident in all directions

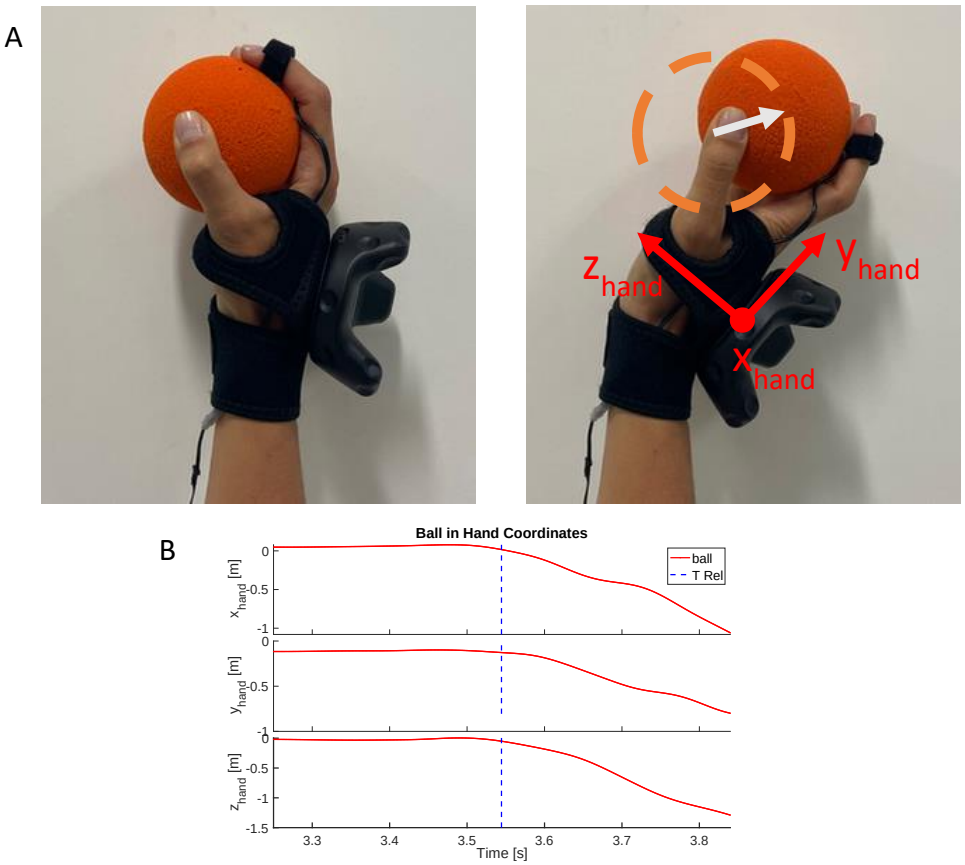

Figure 3.14. Ball-tracker interaction. (**A**) Ball movement during fingers opening. (**B**) Ball position in hand coordinates shows anticipatory movement respect to switch release time.

During the opening of the fingers the ball starts moving on the hand (Fig. 3.14A) and the actual onset of ball movement along the three axes of the Cartesian reference frame attached to the hand, may occur at different times (Fig. 3.14B). If we do not consider these motions, we cannot extrapolate accurately position and velocity at release. (NCM 2021, NER21).

The Multi Delta method searches for a time t_0, from t_r to 0.1 s before it, that allows to simulate the trajectory with the minimum average error of the simulated impact position with respect to the position recorded with the optoelectronic motion capture system:

$$\Delta \boldsymbol{T}^* = \text{argmin}_{j=1:J}\left(\Sigma_{i=1:nTrial}\left(||\boldsymbol{P}_{imp,i} - \widehat{\boldsymbol{P}}_{imp,ij}||\right)\right)$$
$$\widehat{\boldsymbol{P}}_{imp,ij} = F_{Forward\ Dynamics}\left(\Delta \boldsymbol{T}_j, Target, k_{air}, h(t)_i, t_{switch,i}\right)$$

Equation 3.5. Multi delta time estimation general solution (online implementation). The equation finds $\Delta \boldsymbol{T}^*$ minimizing the impact error between the simulation and the real impact point.

Where $\Delta \boldsymbol{T}^*$ is the general multi delta temporal array, $\Delta \boldsymbol{T}_j$ is one of the J possible delta combinations, $\boldsymbol{P}_{imp,i}$ is the impact estimated from the optoelectronic system ball for trial i-th, $\widehat{\boldsymbol{P}}_{imp,ij}$ is the impact estimated from multi delta algo using ΔT_i and $h(t)_i$ is the hand plane for trial i-th.

For each throw the method finds the times t_0 (3x1 vector) for each axis of the hand coordinates reference system at which the ball starts moving respect the hand. In the time interval between t_0 and t_r, the ball is subject to both the force applied by the hand and the gravity. Neglecting drag and Magnus effect for simplicity, the ball acceleration (**a**) in the hand reference system can be then modelled as

$$\boldsymbol{a} = \boldsymbol{a}_{hand} + R_{hand}^{-1}\boldsymbol{g} = \boldsymbol{a}_b^t + \boldsymbol{a}_g^t$$

Where:

$$\boldsymbol{a}_g^t = R_w^t \boldsymbol{g} - R_w^t \boldsymbol{x}_t^w$$

$$\boldsymbol{x}_r = \boldsymbol{x}_0 + \boldsymbol{v}_0(t_r - \boldsymbol{t}_0) + .5\boldsymbol{a}(t_r - \boldsymbol{t}_0)^2$$

Equation 3.6. Ball trajectory motion equation.

From $\boldsymbol{t_r}$ to $\boldsymbol{t_{imp}}$, the trajectory is simulated using the equation of motion in a linear resisting medium used for estimating the air drag coefficient.

The Multi delta method allows to estimate a unique t_0 solution for all trajectories, which can be used online to correctly estimate release time event and release parameters. However, the method can also be used offline to estimate the best t_0 for each trial, in order to obtain more accurate estimation of the throwing parameters.

$$\Delta \boldsymbol{T}^*_i = \text{argmin}_{j=1:J}\left(||\boldsymbol{P}_{imp,i} - \widehat{\boldsymbol{P}}_{imp,ij}||\right)$$

Equation 3.7. Multi delta time estimation individual solution (offline implementation). The equation finds $\Delta \boldsymbol{T}^*_i$ minimizing the impact error between the simulation and the real impact point for each trial.

An example of trajectory simulated with the Multi Delta General algorithm is shown in Figure 3.15. Release times found for each axis in hand coordinates (x_h medio-lateral axis on the palm plane, y_h normal to the palm, z_h proximal-distal axis on the palm) before the release time provided by the switch were: t_{0x} = -1 ± 31 ms, t_{0y} = -31 ± 38 ms, t_{0z} = -32 ± 44 ms. Simulated ball trajectories estimated with mean release times were more accurate than ball trajectories simulated with the hardware release as shown by the smaller error of impact location on the vertical board: 0.33 ± 0.13 m (estimated), 0.58 ± 0.11 m (switch).

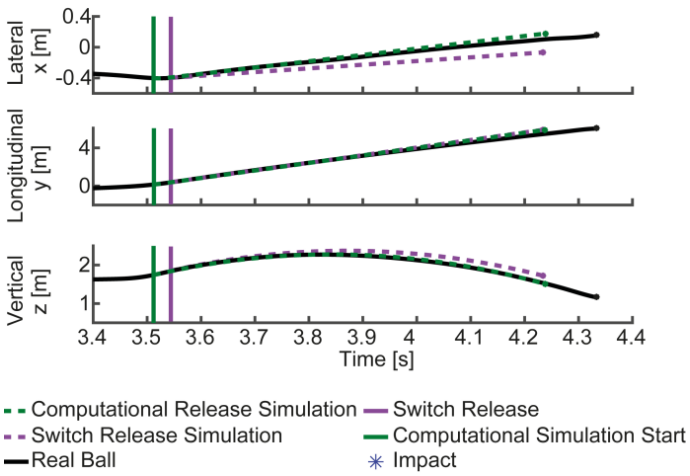

Figure 3.15. Real and simulated ball trajectories.

3.2.4. Validation using an optoelectronic motion capture system

Figure 3.16. Validation setup. Optoelectronic motion capture system.

An optoelectronic motion capture system (Flex 13, Optitrack, Natural Point, Inc., Corvallis, OR, USA) (Fig. 3.16) was used to validate the developed methods and algorithms and to compare them in order to find the most accurate method. The motion capture system, which tracks both the ball and the Vive motion capture sensors (tracker and controller) as rigid bodies, was used to assess the accuracy and precision of ball release position and velocity estimations of the different methods and of the ball impact position estimation obtained from the webcam video acquisition. To this aim, estimates of the release parameters

obtained with the Vive sensors and estimates of impact parameters obtained from the webcam videos were compared with the throwing parameters estimates obtained with the optoelectronic motion capture system.

3.3. Results

In this section the performance and reliability of the developed methods to estimate throwing parameters are presented. Some of the results are evaluated with ad-hoc developed procedure, while others with the validation procedure based on the optoelectronic system recordings.

3.3.1. Webcam performance and impact parameters validation

Several tests were made to estimate the delays in different operating conditions, in particular 4 different Windows operating conditions were tested, selected according to the priority of the process: no priority, high, normal and real time (Fig. 3.17A). From the results the real time priority seems to be the best, among those analysed, in terms of mean and sd delay (0.050 ± 0.013 (s)). The priority of the process must be set at the beginning of each experiment. Furthermore, to avoid further delays or higher standards, it is advisable not to use the PC resources for any other additional task during video recording. Figure 3.17B shows the values relating to each test of the session operating in real time conditions. From the calibration with the Optitrak motion capture system the mean impact point spatial error, computed as the difference between the position estimated from the webcam video and the position estimated by Optitrack, was 0.04 ± 0.02 m (Fig. 3.17D), a distance centre to impact error of -0.04 ± 0.02 m and a mean impact time error, computed as the difference between the time estimated form the webcam video and the time from Optitrak, of 0.03 ± 0.02 s (Fig. 3.17E) (Tab. 3.1).

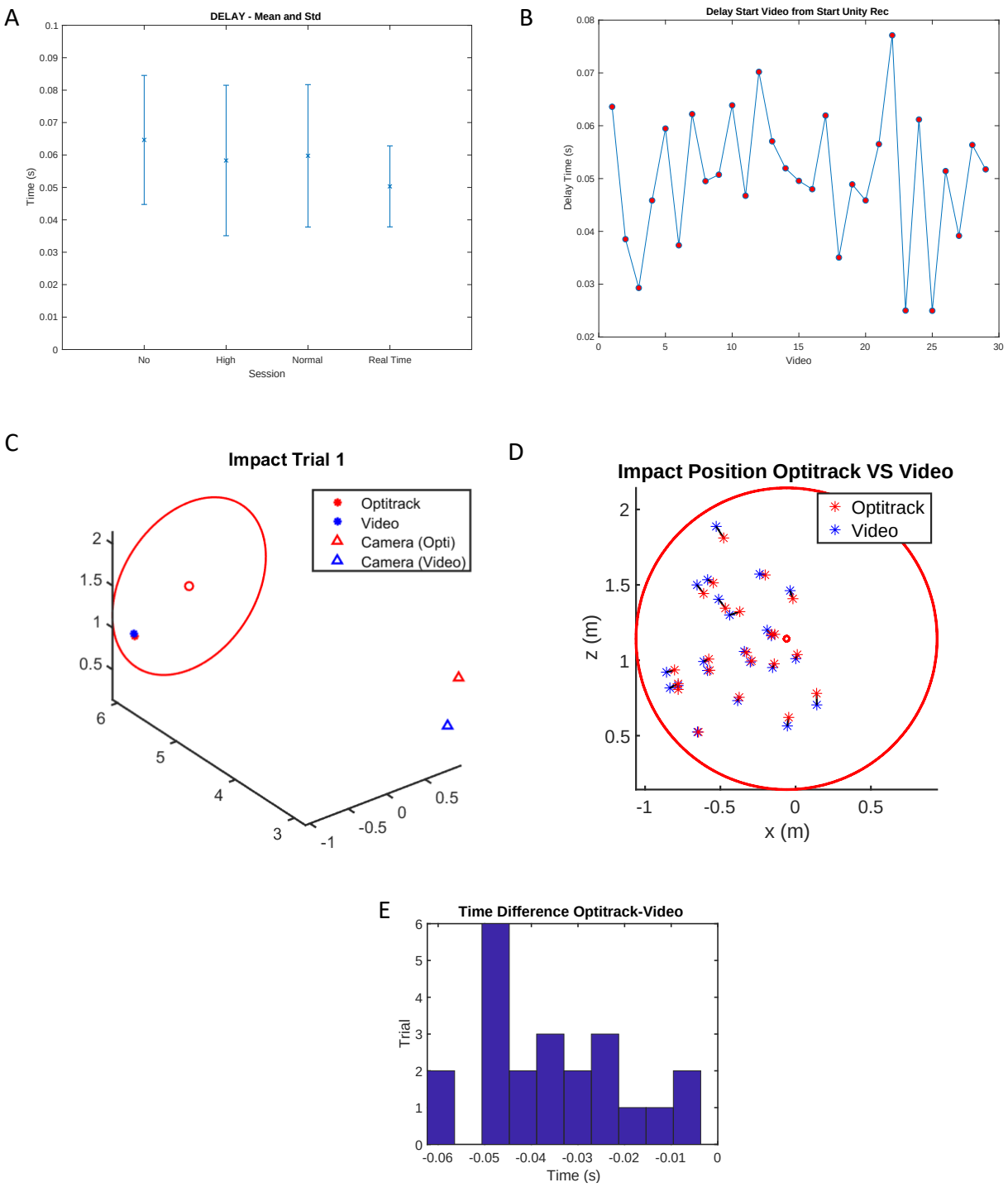

Figure 3.17. (**A**) Mean and sd delay between release time and video frame LED off on 4 different Windows process priority conditions: no priority, high, normal and real time. (**B**) Mean and sd delay between release time and video frame LED off on real time priority condition. (**C**) Example of visualization of impact points and camera position estimated by the 2 acquisition systems, optoelectronic and video. (**D**) Impact position estimation differences between the 2 system. (**E**) Impact time estimation differences between the 2 systems.

Impact point spatial error estimation Video VS Opti (*m*)	Impact point distance to center Video VS Opti (*m*)	Camera position estimation Video VS Opti (*m*)	Impact point temporal error estimation Video VS Opti (s)
0.04 ± 0.02	-0.04 ± 0.02	0.53	0.03 ± 0.02

Table 3.1. Results comparison between impact estimations of the two systems.

3.3.2. Release parameters estimation

In this subsection the accuracy and reliability of the developed methods to estimate release event and relative ball position and velocity are presented in an order of incremental complexity.

3.3.2.1. Single Delta Simulation

In Figure 3.18 the effect on ball trajectory of an anticipatory release is shown for the first trial of the dataset (10 trials from a single thrower). For each axis (x, y, z) ball trajectory and impact point components are shown for the real ball (green line), the virtual ball (red line) and the simulated one (cyan line). This simulation, in which the release happened 7 frames before the microswitch release event detection, as shown in the figure, was selected because it minimizes the impact (blue star) error with respect to the trajectory recorded with the Optoelectronic system. Moreover, the tracker trajectories recorded with the 2 systems are shown, real tracker (black line) and virtual tracker (blue line).

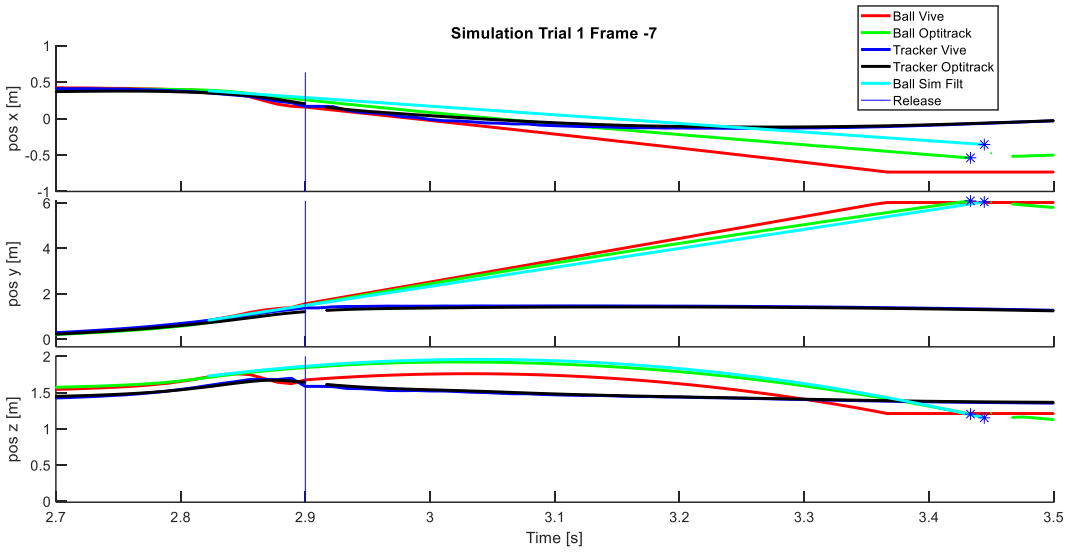

Figure 3.18. Single delta simulation. For each axes ball and tracker trajectories and impact points recorded with the optoelectronic system and the developed one are shown (red line: virtual ball, green line: real ball, blue line: virtual tracker, black line: real tracker). The ball simulated from an anticipatory release (cyan line) are shown from 1 to 9 frames before the hardware switch release (vertical blue line).

In Figure 3.19 the mean result for all trials is reported (10 trials). The figures show the mean difference between the values of release position and velocity and impact position estimated according to the single delta simulations and the values estimated by Optitrack for all the trials (mean) and for each single trial. Release parameters (release position and velocity) and impact parameters (impact position) are reported both as vectors for all the axes (left column) and for each axes (right column). The best mean impact estimation distance with respect to the real one 1.162 m, achieved with this method, which was obtained when the simulation starts from 0.056 s before the time of release of the hardware switch (Tab. 3.2). In Table 3.2 each row shows the result of a different optimization in which the delta parameter minimizes the error in the release position (first row, where the minimized value is indicated in bold), release velocity (second row), and impact distance (third row). The results indicated that a more accurate simulation is required and that a different release time is required for each component of the hand reference system.

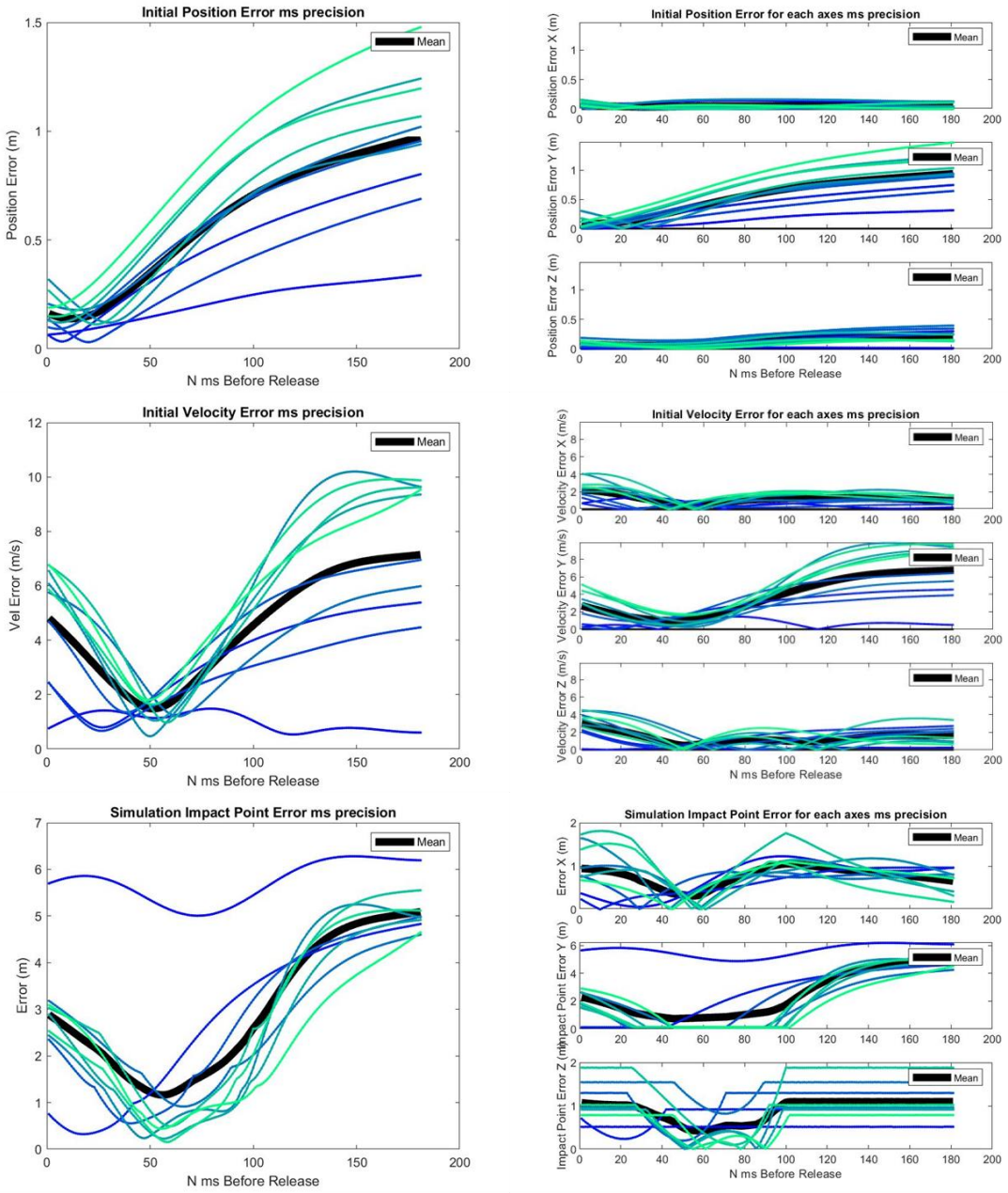

Figure 3.19. Ball trajectories from release to impact. Real ball (red trajectory) recorded from optoelectronic system, ball trajectory simulated with drag (green) and without (blue). The target of 1 m radius is placed at a distance of 6 meters from the thrower.

Delta Time [s]	Release Position [m]	Release Velocity [m/s]	Impact Distance [m]
0.012	**0.1389**	4.001	2.535
0.051	0.357	**1.483**	1.209
0.056	0.398	1.551	**1.162**

Table 3.2. Single delta throwing parameter estimation performances. Table shows the error between real throws and single delta simulations estimations for release position, velocity and impact position. The delta selected for each row is the one that minimize the bolded parameter.

3.3.2.2. Ball trajectory simulated with drag

Average performance in terms of impact point error, computed with a ball trajectory simulation including an air drag coefficient of k = 0.4425, with respect to impact measured with Optitrack was 0.100 ± 0.045 m, while it was 0.340 ± 0.102 m for ball trajectories simulated without drag. Average impact time difference was -0.005 ± 0.009 s for ball drag simulation and -0.069 ± 0.044 s for ball simulated without drag. Figure 3.20 shows an example of ball trajectories, from 0.05 s after the time of release switch to target impact time, recorded with Optitrack (red), simulated with drag (green) and without (blue).

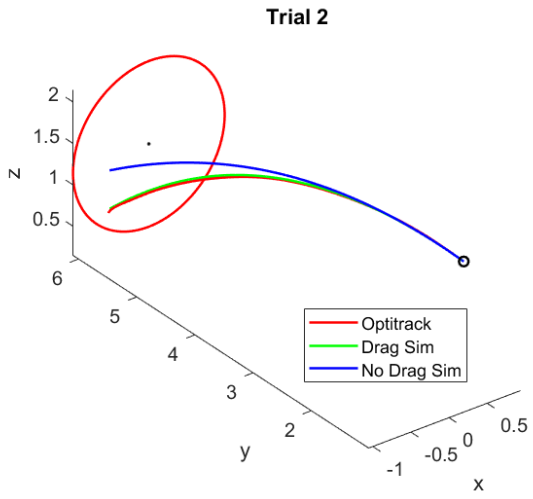

Figure 3.20. Ball trajectories from release to impact. Real ball (red trajectory) recorded from optoelectonic system, ball trajectory simulated with drag (green) and without (blue). The target of 1 m radius is placed at a distance of 6 meters from the thrower.

3.3.2.3. Comparison of methods for the estimation of ball release parameters

Release position parameters estimated with Multi Delta methods are closer, respect the other methods considered, to the parameters recorded with the optoelectronic system at switch release time. Fig. 3.21 shows average differences of release positions (Fig. 3.21A) and velocities (Fig. 3.21B) with respect to positions and velocities measured by Optitrack estimated by each method compared across the entire dataset (22 trials). Fig. 3.21C and D show respectively differences along the three different components of the position and velocity vectors. The Multi Delta offline method does not estimate release parameters better than the Multi Delta online method. The worse performance of the offline method with respect to online one may be due several factors. First, the Multi Delta method minimizes the impact error rather than the release parameters. Second, the comparison between parameters is performed at switch release time, which do not coincide with the real release

time. Third, release delta in multi delta online/general [0, 0.01,0.02] s is timely closer to the switch release time than the offline/individual deltas which can vary from 0 to 0.1 s before the switch.

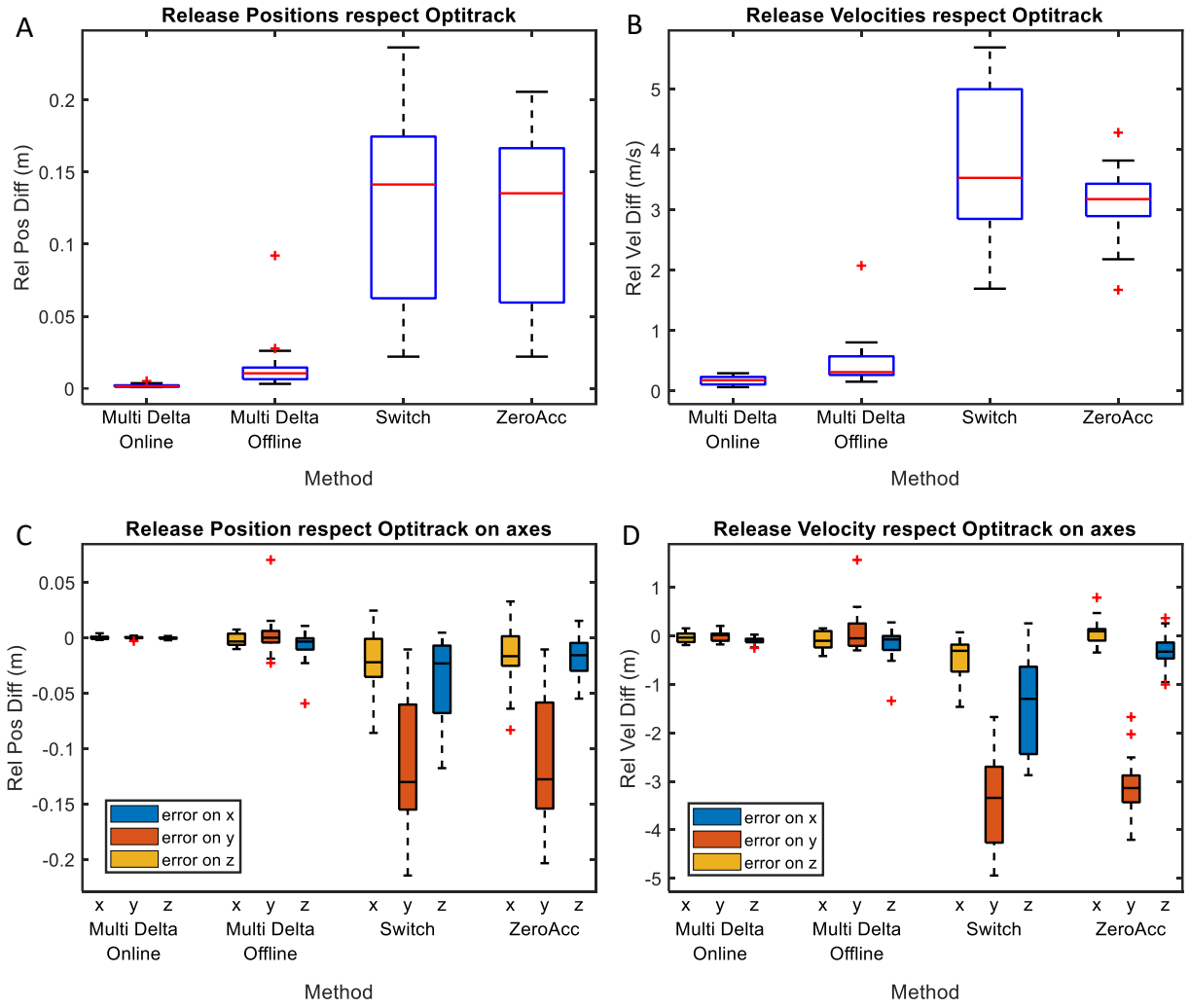

Figure 3.21. Methods average release parameters differences respect real one (Optitrack).

Method	Release position (mean ± sd) [m]	Release velocity (mean ± sd) [m]
Multi Delta Online	0.002 ± 0.001	0.173 ± 0.074
Multi Delta Offline	0.016 ± 0.02	0.47 ± 0.44
Switch	0.131 ± 0.066	3.837 ± 1.205
ZeroAcc	0.122 ± 0.056	3.131 ± 0.599

Table 3.3. Methods release parameters estimations reliability. Table shows the error between (mean and sd) real throws and the developed methods.

3.3.2.4. Impact performance

Average performance in terms of impact position error with respect to Optitrack is better for Multi Delta methods respect the other compared methods. The best performance was obtained for the Multi Delta Individual (Offline) method (0.047 ± 0.065 m). Fig. 3.22A shows the average error of ball impact position on the target plane. Fig. 3.22B shows errors along each coordinate axis. Fig. 3.22C show the average impact time error with respect to Optitrack.

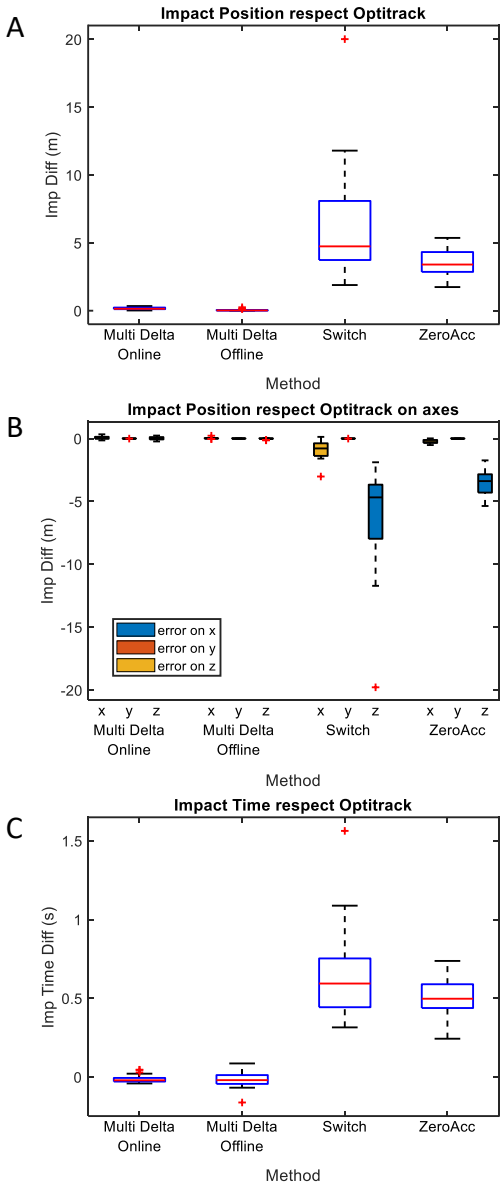

Figure 3.22. Methods average impact differences respect real one (Optitrack). (**A**) Average impact error for each method. (**B**) Average impact error for each method for each axis. (**C**) Average impact time differences respect real one.

Method	Impact position (mean ± sd) [m]	Impact time (mean ± sd) [s]
Multi Delta Online	0.154 ± 0.086	-0.011 ± 0.028
Multi Delta Offline	0.047 ± 0.065	-0.017 ± 0.054
Switch	6.303 ± 4.325	0.662 ± 0.301
ZeroAcc	3.459 ± 1.07	0.499 ± 0.125

Table 3.4. Methods impact parameters estimations reliability. Table shows the error between (mean and sd) real throws and the developed methods.

3.4. Discussion

Studying complex tasks, such as unconstrained ball throwing, can be challenging and expensive with the motion capture technologies available on market. In this chapter, a low-cost system, developed using a commercial VR platform, has been presented. The system allows to investigate virtual throws and real throws. The Virtual Throws operation mode allows to simulate throws in a VR environment and to study release (position and velocity) and impact (position on target and time) parameters, when throwing actions are controlled by the motion capture sensor integrated in the system (controller). Since throwing a virtual ball using a controller is not representative of naturalistic throwing, due to the unusual hand-controller interaction and ball dynamics, some hardware and software components have been developed and integrated in the system to record real throwing actions and to reliably estimate throwing parameters. An experimental setup, which reproduces the VR environment, has also been constructed. In the Real Throw operation mode, real ball release detection is controlled by a micro-switch and ball impact on the target is estimated by a synchronized webcam using an image processing procedure. Four methods to estimate release parameters have been developed and their accuracy has been assessed by comparison with the estimates provided by a second state-of-the-art optoelectronic motion capture system. A calibration procedure has been developed to customize the system on

subject's morphology (hand-ball distance calibration), a ball-hand model has been developed to take into account hand-ball interactions. A drag model has been used to simulate more accurately ball flight dynamic. Impact parameters estimation has been validated both with a calibration procedure, using a LED attached to the switch, and with the optoelectronic system synchronous recordings, to validate impact time and position accuracy.

The best release method, called Multi Delta individual has been evaluated with an optimization procedure, which finds for each trial and each axis of a coordinate system attached to the hand the temporal delay minimizing the impact point error, shows an impact spatial error of 0.047 ± 0.065 m and a release position and velocity error respectively of 0.016 ± 0.02 (m) and 0.47 ± 0.44 (m/s). Since the method require a different delay time for each axis and each trial, it is not possible to use it online as it requires an offline analysis. To overcome this limitation, a second optimization procedure called Multi Delta general, has been developed to allow the online estimation of the release parameter based on an offline estimation of a unique set of 3 different delays, one for each hand coordinate. With this method we found an average impact position error of 0.154 ± 0.086 m and release position and velocity errors respectively of 0.002 ± 0.001 m and 0.173 ± 0.047 m/s. It should be noticed that even if the second method has a higher impact error, it has lower release parameter error compared to the first one. This may be due to several reason. First, these methods minimize the impact error rather than the release parameters. Second, the comparison between parameters is performed at switch release time, which does not coincide with the real release time. Third release delta found in multi delta online/general [0, 0.01, 0.02] s is timely closer to the switch release time than the offline/individual deltas which can vary from 0 to 0.1 s before the switch.

The impact parameters estimation procedure based the webcam video had on average an impact position error of 0.04 ± 0.02 m, a distance centre to impact error of -0.04 ± 0.02 m, and a temporal delay of 0.03 ± 0.02 s. A mismatch with the temporal error found with the LED

procedure calibration (0.050 ± 0.013 (s) was found. It can be due to the time delay between the system and the optoelectronic one.

3.5. Conclusions

The developed system allows to study throwing and real-life complex tasks using a controlled experimental paradigm in a virtual environment and in a natural environment. In particular, the system can be used for studying unconstrained throwing without an expensive motion capture system in real and virtual scenarios. Future studies will investigate the effect of different throwing styles, strategies and learning capabilities of altered dynamic of ball flight (e.g. altering gravity or drag) and hand-ball interaction (e.g. simulating balls with additional degrees of freedom).

4. Development and validation of an innovative methodology for upper limb post-stroke rehabilitation based on Virtual Mirror Therapy

4.1. Introduction

Cerebral stroke is one of the main causes of disability in adults and involves, in many cases, a contralateral hemiparesis of the upper limb. This motor deficit, which occurs for 80% of patients in the acute phase and for 40% in the chronic phase, can be improved by involving patients in rehabilitation protocols with high-intensity and task-specific exercises (Cramer et al., 1997; Kwakkel et al., 2004; Veerbeek et al., 2014). Technological advances in recent years have provided new methodologies to support and favour the rehabilitation process by increasing its repeatability and intensity (Foley et al., 2012).

Rehabilitation systems integrated in virtual reality (VR) environments can provide more complex training scenarios than the traditional rehabilitation therapy. In addition, daily life activities can be simulated in an ecological and controlled manner thanks to the immersive properties of virtual headset devices. Thus, VR scenarios effectively increase patient's active participation and motivation in successfully performing the rehabilitation protocol (Domínguez-Téllez et al., 2020).

Recent advancements in the assessment methodologies have allowed to devise customized rehabilitation approaches, aimed at restoring specific components of the motor deficits. In particular, post-stroke motor deficits are characterized by specific patterns of muscle co-activation or pathological muscle synergies. Regarding muscle synergies, quantitative approaches have recently been developed for identifying motor coordination strategies in healthy subjects based on the decomposition of muscle activation patterns as a combination of physiological muscle synergies through factorization algorithms (Bizzi et al., 2008; d'Avella et al., 2006). When applied to muscle patterns recorded from post-stroke patients,

such decomposition approaches have revealed specific changes in muscle coordination (Cheung et al., 2009, 2012; Clark et al., 2010). Thus, the characterization of the alterations of the post-stroke muscle patterns by their decomposition as combination of muscle synergies can provide an indicator of the pathological state, with prognostic value on the functional recovery induced by a therapeutic intervention, which may be more accurate than the assessment obtained using clinical scales or quantitative measures based only on kinematic data.

In addition to the applications of VR and muscle synergies, myoelectric control is also a novel and promising approach for rehabilitation. Myoelectric interfaces have been mostly used for the control of actuators such as exoskeletons or prostheses (DiCicco et al., 2004; Liarokapis et al., 2013). Thanks to myoelectric interfaces, which decode the patient's intention through the residual myoelectric activity of the paretic limb, patients may generate voluntary movements through their spared cortico-spinal pathway and receive feedback (e.g. visual) thus establishing a closed loop system that promotes re-learning and encourages active participation, increasing motor coordination and muscle strength, and reducing spasticity (Song et al., 2013). The use of myoelectric interfaces for rehabilitation also aims at promoting neuroplasticity to reshape neuromuscular activity and to enhance motor learning, leading in some cases to the restoration of motor function.

The aim of the work presented in this chapter was to evaluate the effectiveness of a novel post stroke upper limb rehabilitation approach based on VR and myoelectric control. The approach is based on the use of a VR system (HTC Vive) for displaying virtual environments and an 8 channels myoelectric sensor (Myo Armband) available on the consumer electronics market for recording EMG signals. The development is the result of a collaboration with the Deutsches Institute of Robotics and Mechatronics Zentrum für Luft- und Raumfahrt e.V. (DLR) of Munich, Germany, which is the coordinator of a project (VVITA) funded by the Helmholtz Association e.V. (Germany).

The system allows to practice rehabilitation exercises that simulate the performance of daily life activities in immersive VR environments, providing real-time visual feedback on the movement of a virtual limb that reproduces and improves the movement of the paretic limb via a visor integrated into a wearable helmet. The movement of the virtual paretic limb is displayed based on the movement and electromyographic activity of both the impaired and the unimpaired limb recorded with the system integrated motion capture sensors and the wearable bracelets.

To validate the system, the effectiveness of VR neurorehabilitation therapy for the recovery of motor function is assessed through clinical and instrumental evaluations performed before, in the middle, and after the entire rehabilitation treatment. This chapter presents preliminary results of a pilot study currently ongoing at Fondazione Santa Lucia.

4.2. Methods

Figure 4.1. VVita Setup. (**A**) Virtual reality headset HTC Vive. (**B**) EMG bracelet Thalmic labs Myo. (**C**) Motion capture HTC Vive tracker sensor. (**D**) Motion capture HTC Vive controller sensor. (**E**) Laptop connected to the system. (**F**) One of the two HTC Vive base stations. (**G**) Adjustable table. (**H**) Therapist. (**I**) Physiotherapist.

The experimental setup included a VR system with a head-mounted display, two wearable hand trackers, two arm bracelets for EMG signals recordings, and a table with adjustable height. An experimenter assisted by a therapist performed the training sessions and the clinical evaluations.

4.2.1. VR system + Trackers

The Vive system (HTC Europe Co. Ltd, Slough, Berkshire, U.K), includes two base stations (Fig. 4.1F) emitting infrared pulses which create a "room scale" tracking area where the position of the headset (Fig. 4.1A) and the trackers can be measured with sub-millimeter precision (Bauer et al, 2021). The headset displays the interactive virtual scenario designed

for the performance of a virtual bimanual reaching task, at a refresh rate of 90Hz, with a 110° field of view, and with a display resolution of 1080×1200 pixels per eye. Two Vive trackers (Fig. 4.1C), are placed on the dorsum of the participant's hands and used to control a virtual hand for reaching the virtual targets. The trackers are also used to record hands kinematics during the task for offline analysis. The Vive system is integrated via SteamVR with the Unity Engine running on a personal computer (Fig. 4.1E).

4.2.2. Virtual environment

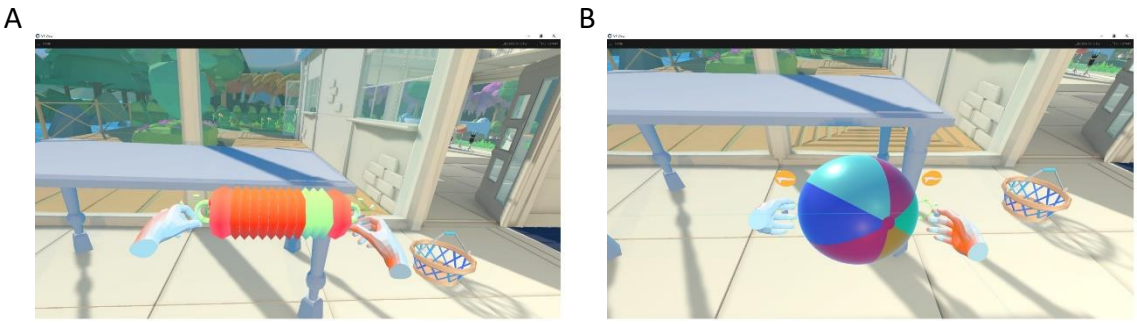

Figure 4.2. Virtual environment. The virtual environment consists of a room in a house with a desk and two different objects, a concertina (**A**) and a beach ball (**B**), that the participants is instructed to reach with both hands.

The virtual scenario reproduces a familiar environment with a table in front of the patient, a virtual representation of the hands of the patient and the objects to be reached and grasped bimanually (Fig. 4.2). A calibration procedure, based on the Vive controller (Fig. 4.1D), allows to match the position and the size of the virtual table with respect to the real one. Two different objects are used as targets. For each object a different hand gesture is required to complete the reaching action: for the concertina (Fig. 4.2A) the fingers must be closed (fist gesture) while for the ball (Fig. 4.2B) the finger must be opened (hand opening gesture).

4.2.3. Myoelectric bracelets

Electromyographic activity is recorded from patient's forearm muscles by Myo armband sensors (Thalmic Labs, Ontario, Canada) placed on both patient's forearms (Fig. 4.1B). The Myo armband, is composed of eight small plastic parallelepipeds connected with a plastic band. Metal electrodes placed on face of the parallelepiped in contact with the forearm skin and connected to a differential amplifier record the surface electromyography (EMG) signals associated with the contraction of the different forearm muscles. A calibration phase uses a machine learning method (Gijsberts et al., 2014) to build an EMG to activation mapping used to decode three different gestures (relaxed, fist, extended) and to control the virtual hands during tasks execution.

4.2.4. Algorithms for controlling the virtual limbs

Controlling the virtual limbs requires two different methods: one to estimate hand position (proximal control) and one to estimate hand gesture (distal control). Proximal control uses the kinematic recorded by the trackers, whereas distal control uses the EMG recorded by the Myo armband.

The virtual unimpaired limb (VUL), represented with as the position and orientation (pose) of a virtual hand, reproduces the position and orientation of the real unimpaired limb (RUL) via the tracker placed on the dorsum of the hand. The VUL gesture activation, defined as the kinematic configuration of the fingers, is estimated using the EMG signals gathered from forearm muscles of the unimpaired limb using iterative Random Fourier Features Ridge Regression (iRR-RFF) (Patel et al, 2017) and displayed at the VUL hand as finger flexion angles.

The virtual impaired limb (VIL) can be controlled by real impaired limb (RIL) pose and gesture or by a weighted combination of the RIL and the RUL (Eq. 4.1), where F is a fixed

and task-dependent transformation, labelled "stiff coupling", which consists in a reflection with respect to a vertical plane passing from the start position and centre of the target.

$$\boldsymbol{x_{VIL}} = \alpha_p \boldsymbol{x_{RIL}} + (1 - \alpha_p)\, F[\boldsymbol{x_{VUL}}]$$
$$\boldsymbol{q_{VIL}} = \alpha_d\, \boldsymbol{q_{RIL}} + (1 - \alpha_d)\, \boldsymbol{q_{VUL}}$$

Equation 4.1. Virtual impaired hand position and gesture estimation equations.

The difficulty of the task is controlled by two parameters for both hand pose (proximal) and hand gesture (distal) that can be adjusted during training: "agency" α and "capability" β. The α parameter, ranging between 0 and 1, determines the contribution of the RIL movement to the VIL movement, i.e., how much *agency* the real limb has on the virtual one. Such parameter is adjusted separately for the proximal control (α_p) and, for distal control (α_d). If α is 1, the VIL reproduces exactly the pose and gesture (estimated from EMGs) of the RIL. This condition allows a participant with no impairment to intuitively perform the bimanual reaching task in the virtual environment. However, if a participant is unable to reach the target with the RIL but can do so with the RUL, the movement of the VIL will be improved by the weighted combination of movement of the VUL. For instance, the higher α_p, the closer the VIL pose will be to the RIL pose rather than to the reflection of the RUL, while the higher α_d, more directly the VIL hand gesture will be controlled by the RIL rather than mirroring the VUL gesture.

The coefficient β, also ranging between 0 and 1, is adjusted according to the *capability* of the patient, and determines the maximum target distance for the proximal control β_p, and the difficulty of performing a gesture for the distal control β_d. For instance, if β_p is 0 the targets are placed as close to the body as possible and if β_p is 1 they are places at the edge of the patient's peri-personal space. The higher proximal β_p gets, the further away the patient must reach. β_p is estimated for each limb during the first initial maximum amount of movement calibration procedure. Similarly, the required activation of the hand (β_d) can range from 0

to 1. If the value is smaller, less muscle activation is required to achieve a successful gesture, whereas for higher values, a stronger muscle activation is required.

The therapy is administered in different days, each day is defined as a session. During each session the patient must perform a series of blocks, each consisting of 12 bimanual reaching and grasping movements towards objects in different target locations $\mathbf{x}_{tar} = \mathbf{x}_{tar}[r, \theta, h, \beta_p]$, where r is the distance from the mean hand position at start posture to the target centre, θ is the target azimuth and h is the target height.

After each block, both proximal and distal agency (α_p, α_d) and capability (β_p, β_d) are adjusted by the therapist, according to a patient's performance score $\pi_j = \pi(t_1, ..., t_{Tj})$ in that block (j-th, composed of T_j trials) in order to obtain a task success rate of approximately 70-90%. In this way the patient is motivated to try to improve his/her performance but is not frustrated by too many failures. So, when the score is higher than 90% (11 or more successful trials over 12 trials in a block) the difficulty is increased. When the score is between 70 and 90% (9-10 successful trials over 12 trials) the difficulty level is not changed. When the score is lower than 70% (8 or less successful trials over 12 trials) the difficulty level is decreased.

The distance (r) of the target is adjusted according to β_p as the fraction of maximum distance recorded during calibration phase ($r = \beta_p r_{max}$); the direction (θ) is selected randomly within a given set of targets and the distance (r) as the fraction of maximum distance recorded during calibration phase ($r = \beta_p r_{max}$) (Fig. 4.3). The required level of muscle activation (grasp intensity) follows a similar law rule with a difficulty adjusted by β_d.

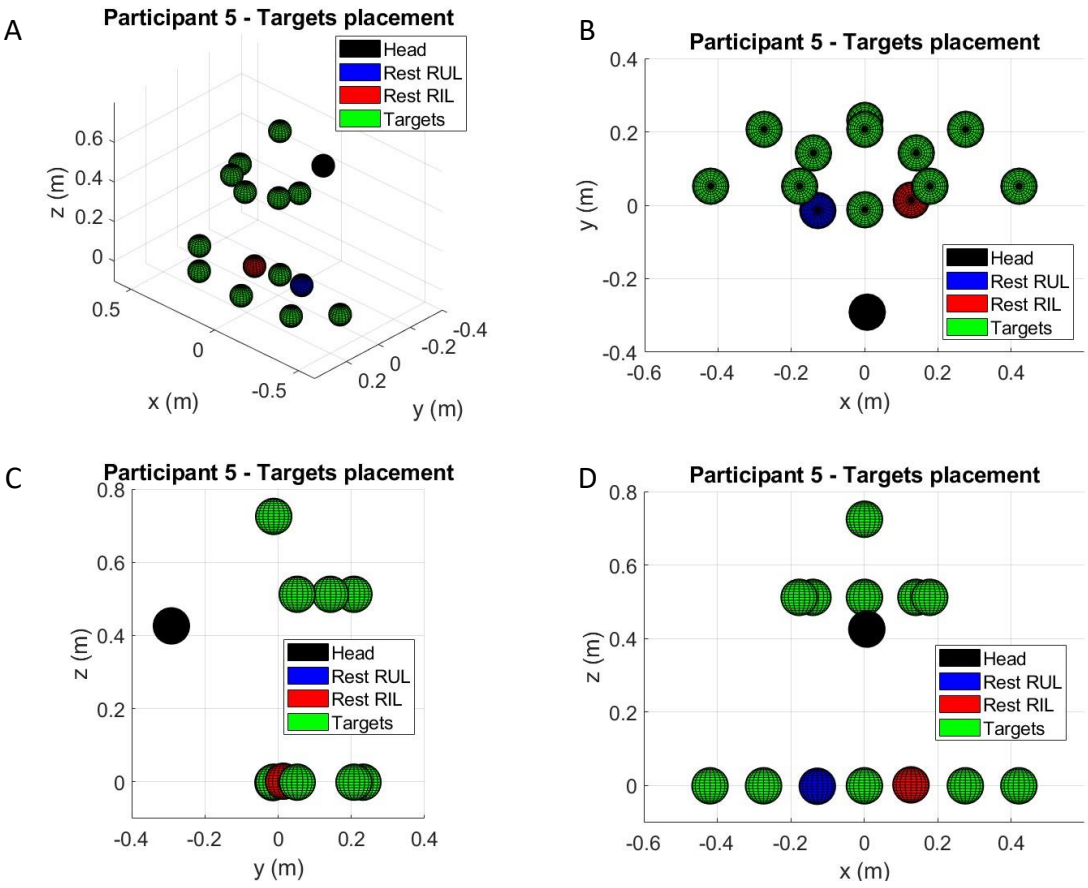

Figure 4.3. Targets placement. Figure shows an example of targets placement for participant 5 when β_P is equal to 1. For each panel a different view (**A**) 3D view, (**B**) top view, (**C**) lateral view, (**D**) frontal view of all the 12 targets (green spheres), the head (black sphere) and RUL (blue sphere) and RIL (red sphere) resting poses.

4.2.5. User-centred development of the setup and the protocol

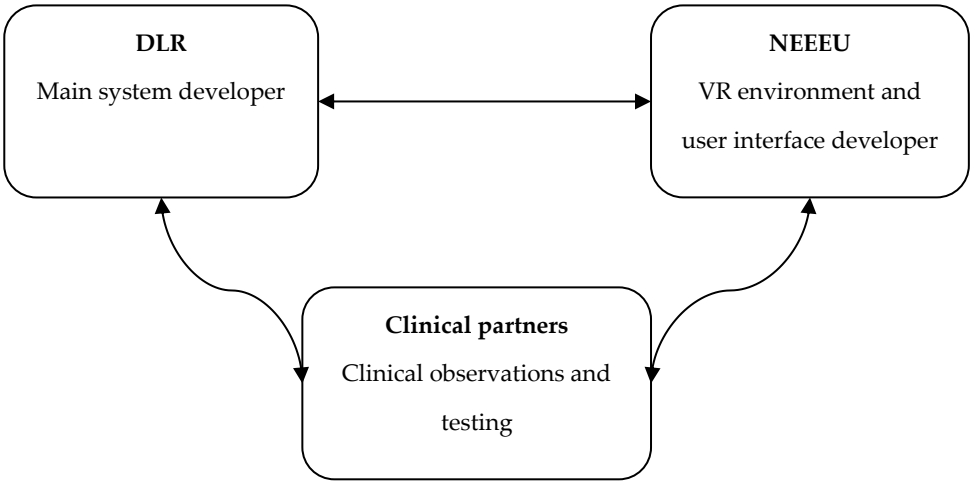

Figure 4.4. User-centered scheme.

The system has been developed as an application to stroke rehabilitation of the VR platform originally developed for upper amputee phantom limb pain treatment within the VITA project also led by the DLR team, coordinated by Prof. Claudio Castellini (Researcher at DLR and Professor at Friedrich-Alexander-University of Erlangen-Nürnberg). The new project (VVITA), is coordinated by the DLR team, which is the main platform developer and has expertise on decoding of upper limb/forearm muscle signals to predict hand movements, and involves NEEEU (NEEEU Spaces GmbH, Berlin, Germany), which collaborates on the design and development of the virtual environment and the user interface, and several clinical partners including the IRCCS Santa Lucia Foundation (FSL, Rome, Italy) in collaboration with the University of Messina (UniMe). The FSL-UniMe team has contributed to both the development the stroke rehabilitation protocol and to the validation of the system with stroke patients.

A user-centred approach, based on involvement of both technical developers, motor control neuroscientists, neurologists, therapists, and patients, has been implemented in the development of the stroke-specific application of the VVITA system. The training activities,

the assistive algorithms and the user interface have been developed and selected through several iterations between all the partners (Fig. 4.4). After the initial analysis of the patients' needs and rehabilitation goals, a simple bimanual reaching task has been selected as the main training activity and the use of a "virtual mirroring" approach, using both kinematic signals for hand pose and EMG signals for hand gesture, has been defined as the key assistive element to enhance functional recovery. Initially, 3 different assistive algorithms were considered (stiff coupling, rubber band and trajectories) and implemented for pilot testing. Each method affects in a different way influence the control modality and the guidance of the unimpaired upper limb to the impaired limb. The stiff coupling method reflects the pose of the RUL with respect to a vertical plane passing from the start position and centre of the target. In this case, the impaired side can be thought of as directly coupled to the unimpaired side: if the RUL moves to the right side, the VIL follows this movement to the right. With the rubber band method, the RUL is mirrored with respect to the mid-sagittal plane as in a classical mirror therapy: if the RUL moves towards the lateral direction, the VIL also moves towards the lateral direction in the contralateral side. The trajectories method projects the RIL along a predefined VIL path according to the path length of the RUL on a predefined VUL path. The path is pre-recorded from the RUL and mirrored to the impaired side.

After pilot testing and several meetings with all partners, the first method (stiff coupling) has been selected to be used in the experimental phase. The amount of assistance provided by the reflection of the unimpaired limb is controlled by the α_p parameter, which has also been introduced as a separate parameter from α_d the during the development after some iterations between the partners to accommodate for different level of proximal and distal impairments in different patients. Also, the difficulty of the task, adjusted by the β_p and β_d parameters, has been integrated in the system and the random displacement of the 12 targets in the virtual space and their orientation have been specially chosen to follow clinician partner requests.

The interaction with the therapists has also been instrumental to the development of therapist a custom user interface (UI) to be used during the training sessions to monitor the signals from the sensors and guide the patients while they are immersed in the VR environment performing the reaching task. The UI allows to visualize the required data as the muscle activity, the VR view seen by the patient and task performances. It also allows the therapist to select the difficulty level of the exercise choosing the desired assistive parameters.

4.2.6. Training protocol

The experimental study to assess the efficacy of a 2 months of treatment and it has been designed taking into account the results of a one-month pilot study performed on 4 stroke patients, 2 chronic and 2 subacute. During the experimental study, each patient was treated for 2 month, 3 times for week, 30 minutes for each session. During each session the patient performed as many blocks of reaching trials as possible. In the middle of the session, the patient was asked to remove the helmet and to take a 3 minute break. Target placement was selected randomly for each block within the 12 possible target positions. At the beginning of each session, patients were asked to perform the maximum range of movement first with the unimpaired limb and then with the impaired one to offline quantify the motor function recovery. The maximum amount of movement (range of movement) recorded during the first session of each patient was used to characterize target placement for all the sessions and to define target placement distance with respect to the resting poses. The objects were rotated around a vertical axis such that the handle of the lateral side of the object was closer to the patient frontal plane, allowing for a more natural bimanual reaching movement. Since the target handles rotation method depends on the maximum range of movement calibrated at the beginning of the treatment and some anthropometric parameters as the shoulder width for each patient, it was not always possible to rotate the targets. Both targets, concertina and ball, were alternatively shown to the patient in order to perform a different

hand gesture each time (fist and extension). For each trial, maximum duration was of 20 seconds, since we noticed that 30 seconds, used during the pilot study, was too long, especially when patients could not successfully reach a certain target, leading to excessive fatigue. The reaching movement was considered successful when both virtual hands were closer than 0.05 m to the center of the target handles and the required gesture was maintained for 1 s. Feedback on the success in hand placement and gesture maintenance was provided to the patient in the VR. The color of the target handles changed from orange to green when the virtual hands position was within the tolerance. A small representation of the required gesture disappeared when the virtual hand gesture was correct. Finally, when both the correct position and the gesture were achieved the object color turned green progressively (Fig. 4.2A), indicating in this way the holding time.

4.2.7. Participants and inclusion criteria

A total of twenty post-stroke patients will be enrolled in the experimental study. Inclusion criteria are age, between 18 and 80 years, gender, male and female suffering from upper limb deficiency following ischemic or hemorrhagic stroke confirmed by CT or MRI, which has occurred at least 1 year before (chronic phase) the beginning of the treatment. UL-Fugl-Meyer scale rate between 14 and 54, Medical Research Council (MRC) scale rate greater or equal to f2 for the shoulder and f1 for the elbow. No toxin treatments in the previous 2 weeks from the beginning and during the treatment.

Exclusion criteria are Modified Ashworth Scale (MAS) greater than 3, Mini Mental State Examination (MMS) grater or equal to 24, absence of orthopedic neurological and rheumatological pathologies that can cause upper limbs sensorimotor deficits. Patients are randomly assigned into two groups: an experimental group and a control group. Randomization takes into account neuromotor deficit severity (moderate and severe) and the age. Inclusion criteria have been selected according to the pilot study results.

As the recruitment of participants and the experimental sessions are ongoing, in this chapter preliminary results of the analysis of 7 participants included in the experimental group are presented. Table 4.1 reports some details of these.

Patient	Age	Gender	Stroke Type	Affected limb	Language deficit	Time since stroke (years)	Session N°
P1	60	M	Ischemic	Left	No	12	24
P2	71	F	Ischemic	Left	No	2	21
P3	38	F	Ischemic	Left	Yes	24	21
P4	48	M	Hemorrhagic	Left	No	28	18
P5	70	M	Hemorrhagic	Right	No	7	20
P6	50	M	Ischemic	Left	No	2	22
P7	64	M	Ischemic	Right	Yes	2	24

Table 4.1. Participants included in the preliminary analysis. The table reports for each participant some patient's informative data as the age, gender, time from stroke and type of stroke. Fugl-Meyer index scores for T_0, T_1 and T_2 are also reported to quantify the functional recovery evaluated with one of the used clinical scales.

4.2.8. Clinical and instrumental evaluations

Clinical and instrumental functional recovery indicators were considered. Upper-limb Fugl-Meyer clinical scale has been used for the evaluation of upper limb functionality. This scale is based on existing knowledge about recovery patterns in stroke. In the motor scale of the Fugl-Meyer assessment, items are based on the ontology and stages of stroke recovery described by Twitchell and Brunnstrom respectively (Gladstone et al., 2002; Sanford et al., 1993). The Fugl-Meyer Assessment scale is an ordinal scale with 3 points for each item. If the subject is unable to complete the task, the item receives a score of 0. When the work is partially finished, a score of 1 is awarded, and when it is successfully completed, a score of 2.

With regards to the instrumental indicators, thanks to the sensors integrated in the VR system, kinematic variables and overall task performances have been recorded. In particular, the score performance, which was kept within a given range by the protocol, was investigated together with the assistance parameters to evaluate therapist's operational behavior. Moreover, the maximum speed achieved during the task execution and the maximum range of movement achieved in each session during the initial calibration were estimated for each limb.

In this preliminary analysis, both the clinical and instrumental evaluations were investigated at the beginning (T_0), at midterm after 12 sessions (T_1), and at the end (T_2) of the rehabilitation protocol.

4.2.9. Statistical analysis

The dependence of the overall assistance level, Fugl-Meyer index, and maximum speed on the different sessions (*Se*) was tested with a linear mixed model (LMM) that accounts for interindividual variability by including the participant as a random effect. The experimental factor (*Se*), was treated as a fixed effect with categorical (dummy) variables. Data were fitted with the model:

$$Y = u_0 + \alpha_0 Se + \epsilon \quad (1)$$

where u_0 represents the individual intercept and accounts for inter-individual differences; the coefficients α_0 represents fixed-effect slopes, thus the modulation of the response variable by the factor *Se*. As data represent a continuous variable, they were fit with a LMM (Matlab, function *fitlme*). Estimation of model parameters were based on the maximum likelihood using Laplace approximation.

4.3. Results

As the study is still ongoing, in this section preliminary results are reported from 7 participants of the experimental group. Control group and the remaining experimental group participants are still performing the rehabilitation protocol.

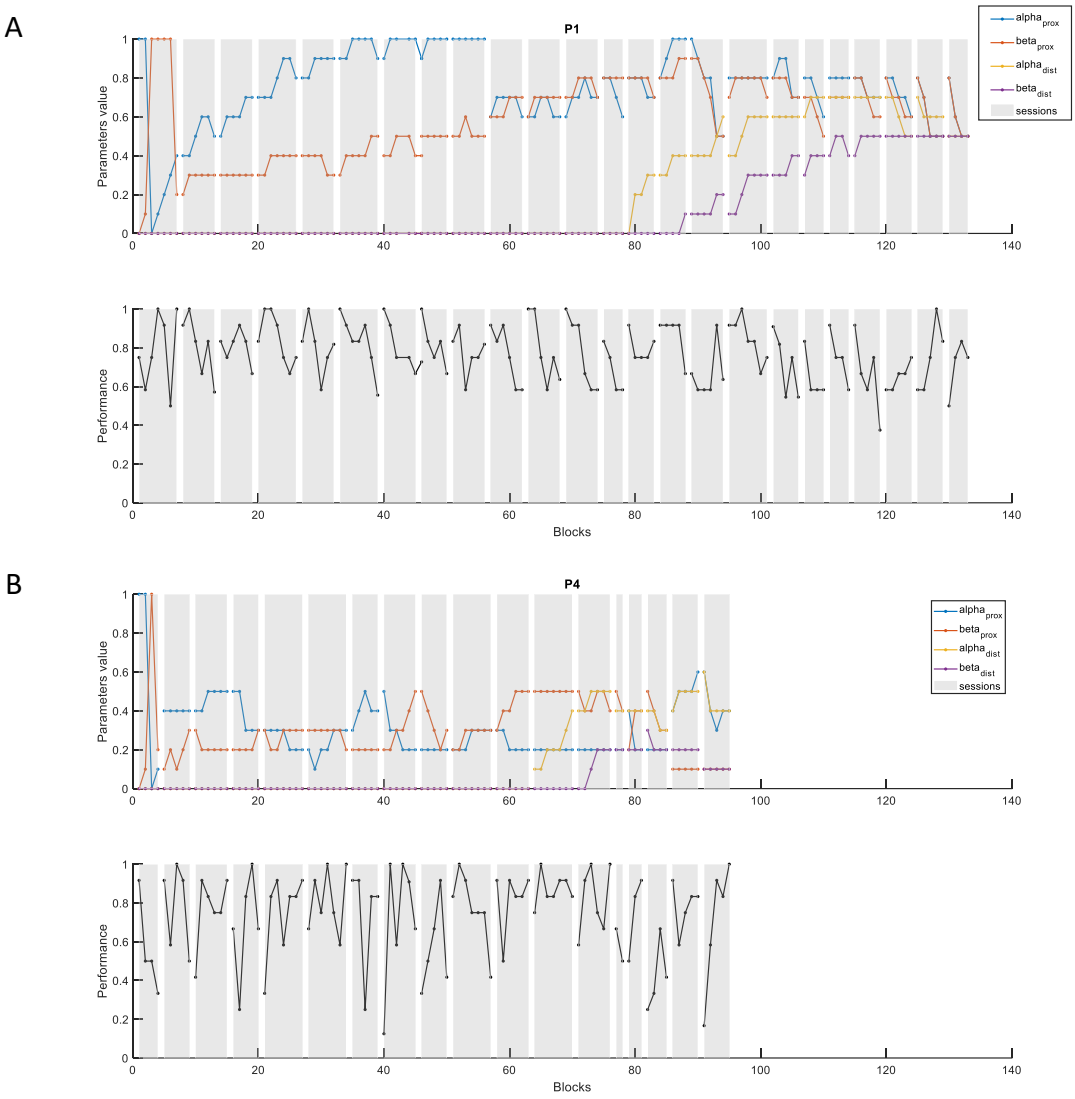

Figure 4.6. Blocks parameter selection and performance. Each panel shows for each participant and each block the 4 assistance parameters (α_p, β_p, α_d, β_d) used and the participants' performance (number of successful trials over number of trials) for patient 1 (**A**) and 4 (**B**).

The assistance parameters (α and β, proximal and distal) were adjusted after each block see paragraph 4.2.4). In Fig. 4.6 the assistance parameters and the performance for patient P1 (A) and patient P4 (B) for each block across all the sessions are reported. P1, who had a

higher level of residual functionality and P4, who had a lower level of residual functionality, were selected to illustrate the assistance parameter selection in the case of low and high upper limb impairment. As the performance graphs show, when the value is smaller than 70% or higher than 90% the difficulty is decreased or increased by adjusting the assistance parameters accordingly. The therapist was successful in keeping the level of performance around 70-80%, as shown in the figure.

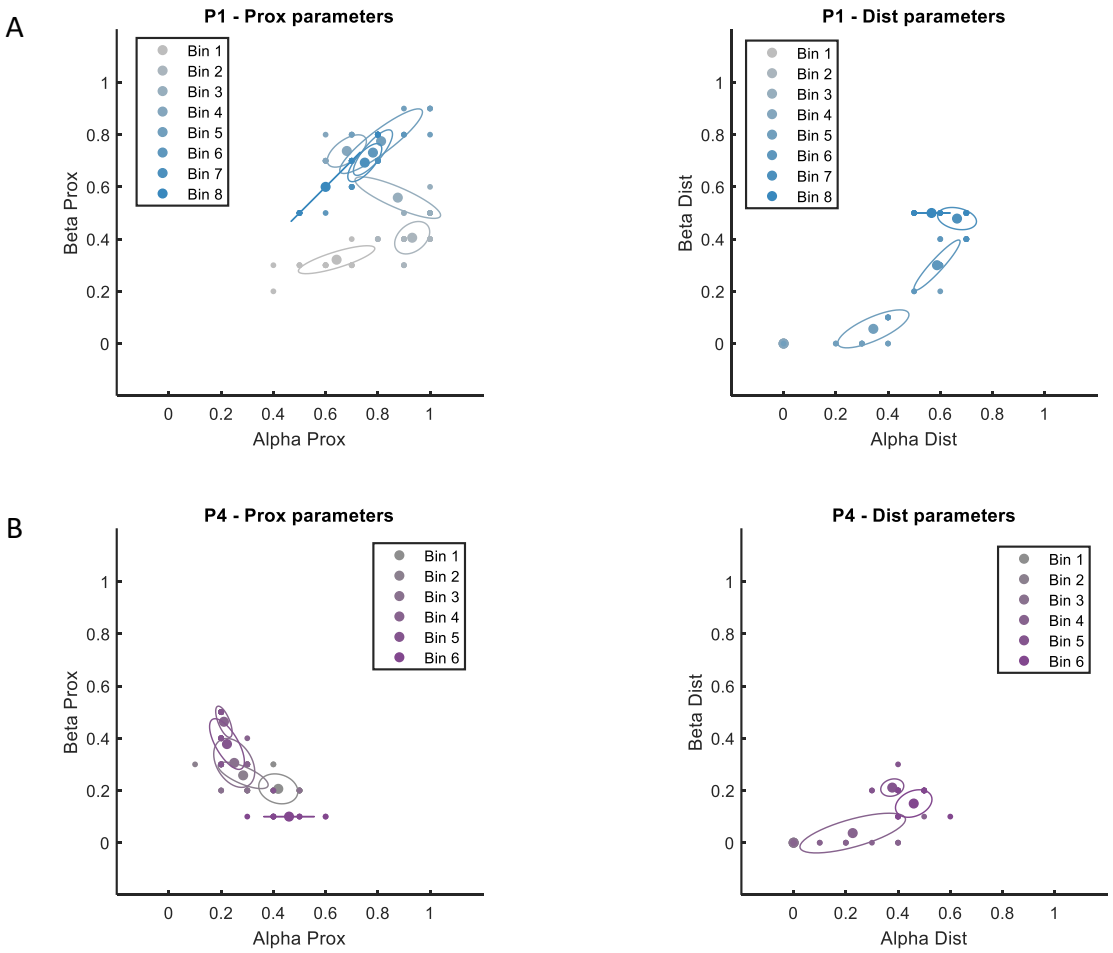

Figure 4.7. Parameters distribution. Figure shows for P1 (**A**) and P4 (**B**) assistance proximal (left column) and distal (left column) parameters distribution. For each bin (3 sessions), the mean value (ellipse center) and the standard deviation (ellipse principal axes) are reported. Color saturation represents the temporal evolution of the distribution.

As example of the parameter distribution used during the rehabilitation protocol is shown in Fig. 4.7 for P1 (A) and P4 (B). For each patient, the proximal (left column) and the distal

parameters distribution (right column) are reported. For each time bin, which correspond to 3 consecutive sessions, the center of the ellipse corresponds to the mean of the values of the α and β parameter in that bin, whereas the principal semiaxes correspond to the parameters covariance. Color saturation shows the temporal evolution of the parameter distribution. The figure shows a clear difference between P1 and P4. For the patient P1, both parameters are closer to one, i.e., indicating less assistance, than for P4, who was less impaired than P4. Moreover, for P1 the parameters over time tend to become closer to 1 than for P4. This indicates that, for the same performance, P1 was able to perform with a greater task difficulty with respect to P4. However, since the therapist can modulate task difficulty changing both proximal and distal assistance parameters, an overall assistance index is required to uniquely define the tasks difficulty.

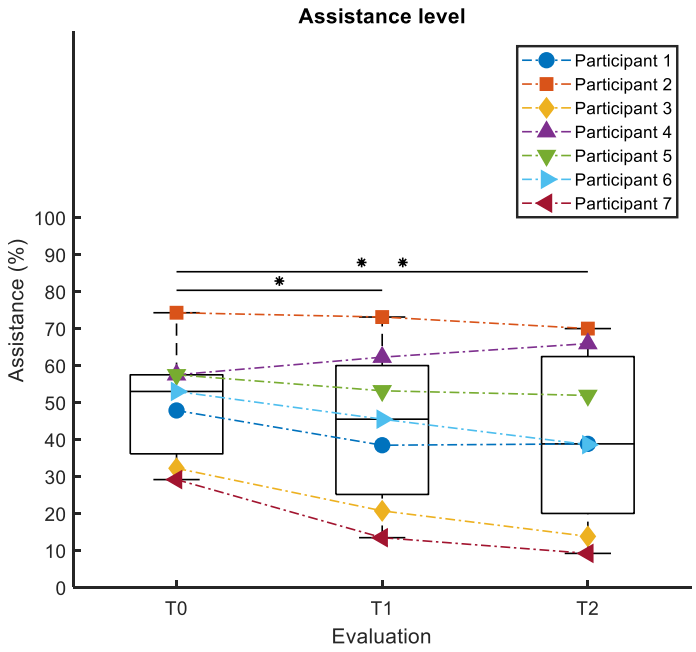

Figure 4.8. Assistance level. Figure shows for the first (T_0), midterm (T_1) and last (T_2) session the overall assistance level for each patient (different colors and symbols) and for all the patients (boxplots). Statistical difference significance is reported as *** = 0.001, ** = 0.01 and * = 0.05.

The overall assistance level, defined as 1-(α_p + β_p + α_d + β_d)/4, decreased for all the patients except for patient 4 (Fig. 4.8, different colours and symbols). The boxplots representing the distribution of the assistance level across all patients are shown for the initial evaluation session at T_0 (mean ± sd = 50 ± 16 (%)), the midterm evaluation session at T_1 (mean ± sd = 44 ± 21 (%)), and the final evaluation session at T_2 (mean ± sd = 41 ± 24 (%)).

Assistance data were fitted with the LMM model of Eq. 1 (see 4.2.9) (R^2 = 0.96), which revealed a significant main effect of session (p = 0.007). Statistical difference between each session is reported in the figure as *** = 0.001, ** = 0.01, * = 0.05. Significant difference between T_0 and T_1 sessions (p = 0.021) and T_0 and T_2 (p = 0.002) were found, while the difference for T_1 and T_2 was not significant (p = 0.313).

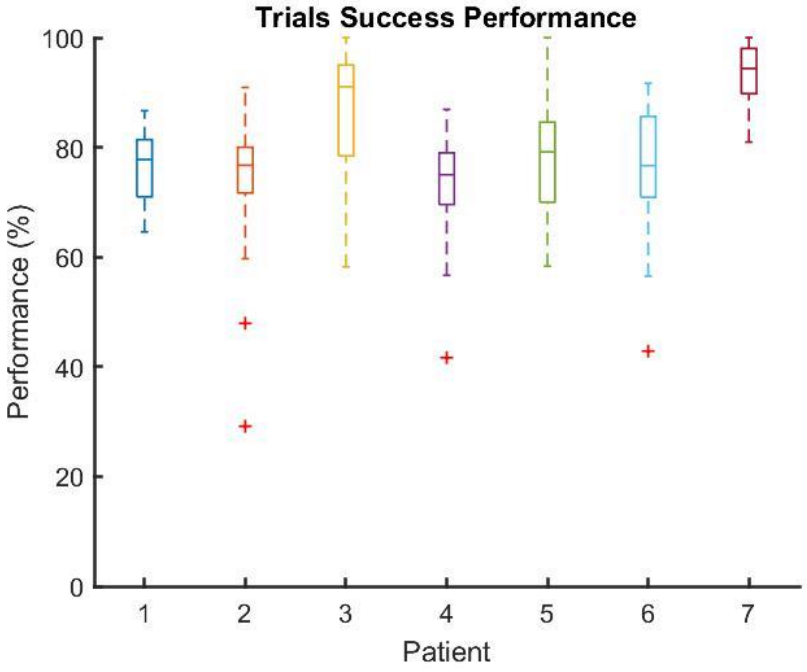

Figure 4.9. Overall reaching performances. Overall reaching performance is shown in the figure as percentage of successful trials over all trials for each patient.

The therapist was instructed to change the assistance parameters in order to maintain performance at around 70-80% in each block. Figure 4.9 shows the overall reaching performance for each patient. The performance, reported as percentage of successful trials

with respect to all performed trials for all sessions, had a mean value across all patients of 79.5 and a standard deviation (sd) of 10.23, which confirms therapist's correct management of task's difficulty. Table 4.2 show the performance (mean ± sd) for each patient.

Patient	P1	P2	P3	P4	P5	P6	P7
Performance (mean ± sd)	76.5 ± 6.7	73.2 ± 13.8	87 ± 11.2	72.8 ± 11	77.5 ± 10.9	76.5 ± 12.1	93.4 ± 5.6

Table 4.2. Participants' performance. The table reports mean and standard deviation of the performance for each patient.

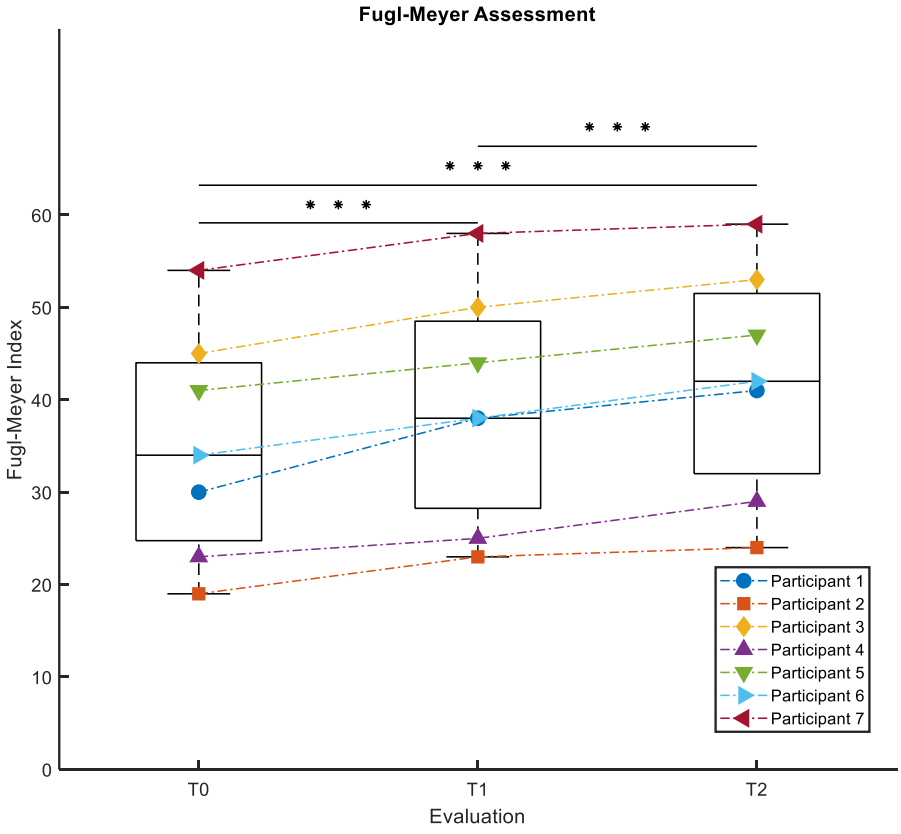

Figure 4.10. Clinical evaluations. Figure shows the first (T_0), midterm (T_1) and last (T_2) upper limb motor function clinical evaluation for each patient (different colors and symbols). The maximum score in upper limb motor function is 66. Statistical difference significance is reported as *** = 0.001, ** = 0.01 and * = 0.05.

Each participant was evaluated clinically at the beginning (T_0) of the rehabilitation protocol, after 12 sessions (T_1) and at the end (T_2). The Fugl-Meyer assessment scale, which has 3 points (index: 0, 1, 2) for each item of the upper limb motor function assessment, has been assessed by the physiotherapists to evaluate the efficacy of the rehabilitation protocol in the treatment of the stroke upper limb hemiparesis. Figure 4.10 shows the evolution of the Fugl-Meuer motor function assessment index for each patient (different colors and symbols) for each evaluation (T_0, T_1, T_2).

The mean and sd of the Fugl-Meyer index over all the patients is reported in the boxplot for the first T_0 (35.1 ± 12.4), midterm T_1 (39.4 ± 12.6) and the last T_2 (42.1 ± 12.4) sessions.
For each patient the motor function upper limb score increases during the temporal evolution of the rehabilitation protocol (Tab. 4.3).

Fugl-Meyer assessment index data were fitted with the LMM model of Eq. 1 (see 4.2.9) (R^2 = 0.99), which revealed a significant main effect of session ($p = 8.22\times10^{-9}$). Statistical difference between each session is reported in the figure as *** = 0.001, ** = 0.01, * = 0.05. Significant difference between T_0 and T_1 sessions ($p < 10^{-5}$), T_0 and T_2 ($p < 10^{-8}$) and T_1 and T_2 ($p < 10^{-3}$) were found.

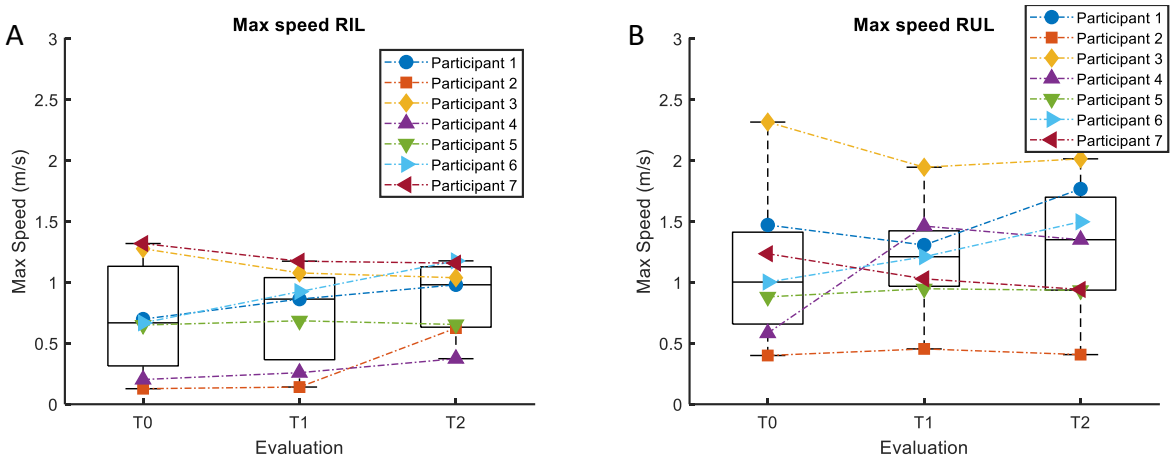

Figure 4.11. Maximum speed. Figure shows the maximum speed for the RIL (A) and the RUL (B) for the first (T_0), midterm (T_1) and last (T_2) session each patient (different colors and symbols) and for all the patients (boxplots).

Maximum speed was estimated for RIL and RUL in each trial to evaluate its evolution during the rehabilitation protocol. The average maximum speed values for each limb for all patients are shown in Fig. 4.11 for the first session T_0 (RIL: 0.7 ± 0.5, RUL: 1.1 ± 0.6), the midterm session T_1 (RIL: 0.7 ± 0.4, RUL: 1.2 ± 0.5) and the last session T_2 (RIL: 0.9 ± 0.3, RUL: 1.3 ± 0.6). Maximum speed data were fitted with the LMM model of Eq. 1 (see 4.2.9) (RIL R^2 = 0.88, RIL R^2 = 0.84), which revealed a non-significant main effect of session for both limbs (RIL p = 0.15, RUL p = 0.51). Non-significant difference between T_0 and T_1 sessions (RIL p = 0.7, RUL p = 0.6), T_0 and T_2 (RIL p = 0.1, RUL p = 0.2), and T_1 and T_2 (RIL p = 0.1, RUL p: 0.5) were found.

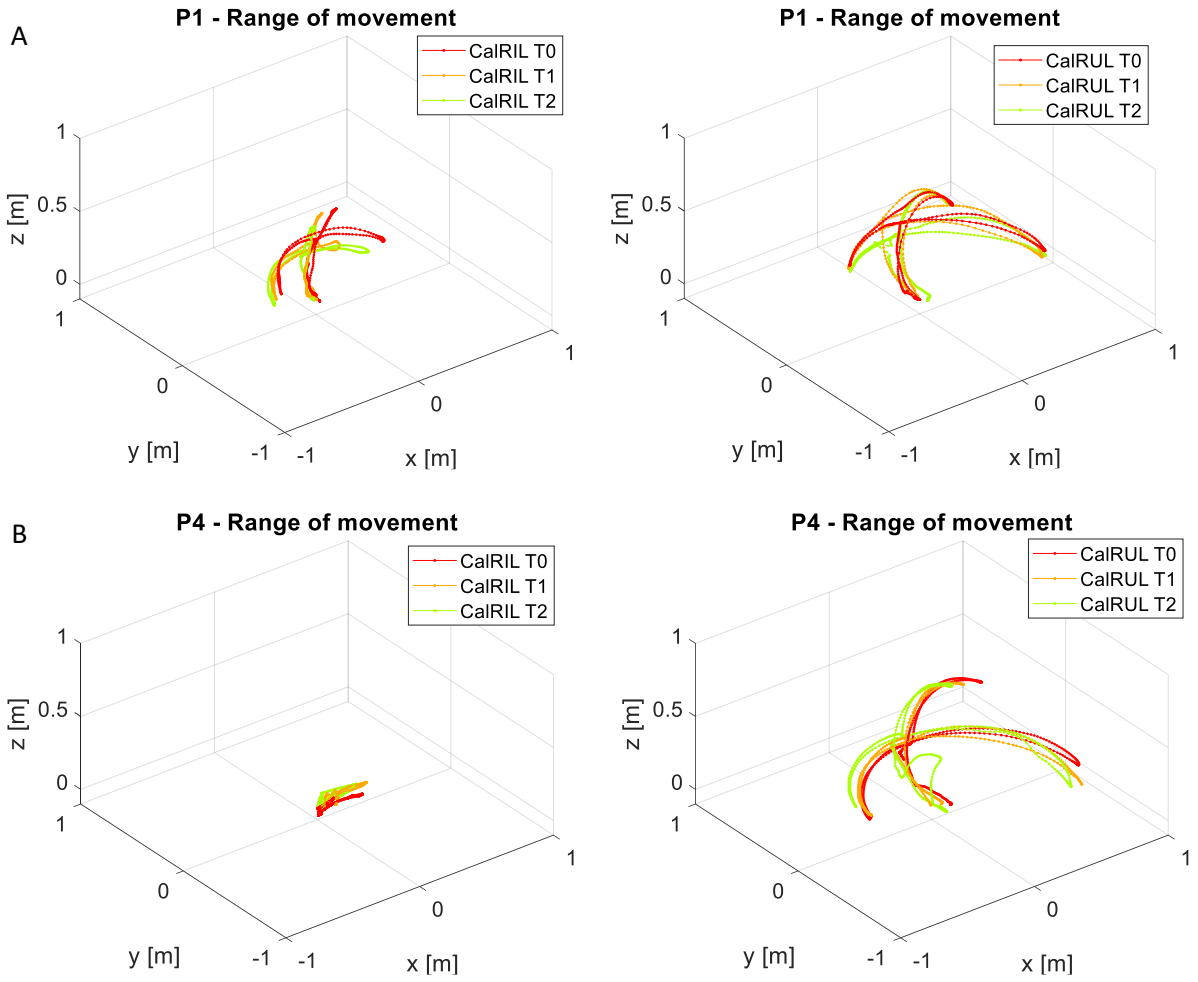

Figure 4.12. Range of movement. Figure shows for patient P1 (**A**) and P4 (**B**), the RIL (left column) and the RUL (right column) maximum range of movement for the T_0 (red line) T_1 (orange line) and T_2 (green line) evaluations.

Finally, the range of motion was assessed on the movement calibration performed at the beginning of each session. Figure 4.12 shows for P1 and P4 the maximum range of movement recorded at the beginning of T_0 (red line), T_1 (orange line) and T_2 (green line) sessions with both RIL (left column) and RUL (right column).

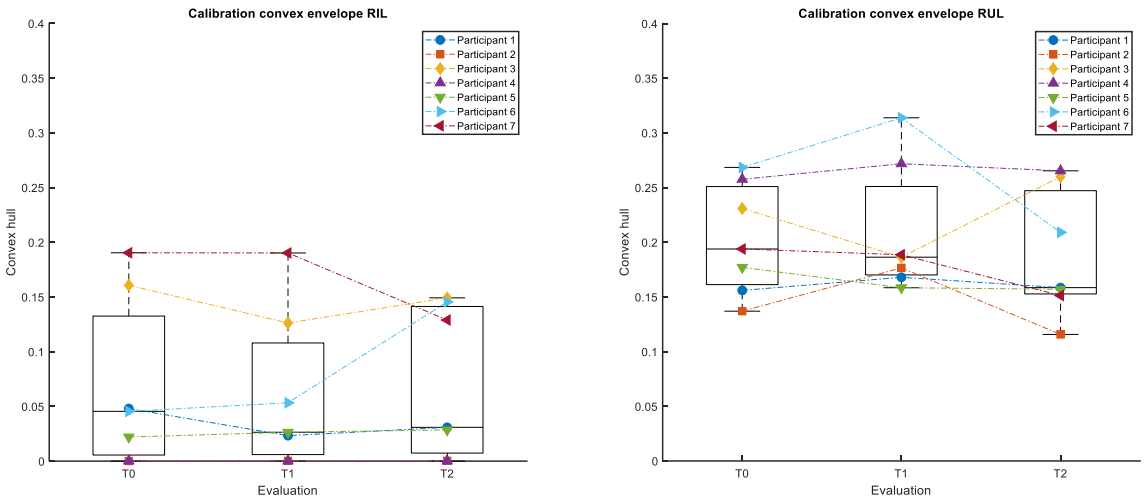

Figure 4.13. Maximum calibration movement achieved volume estimation. Figure shows the convex hull estimated for RIL (left column) and RUL (right column) initial range of movement calibration for the first (T_0), midterm (T_1) and last (T_2) session each patient (different colors and symbols) and for all the patients (boxplots).

To quantify the range of movement, an estimation of the volume of the convex hull of the trajectories recorded during the initial calibration was obtained (Matlab, *convhull* function). Fig. 4.13 shows the average RIL (left column) and RUL (right column) convex hull volume values for each limb for all patient for the first session T_0 (RIL: 0.1 ± 0.1, RUL: 0.2 ± 0.1), the midterm session T_1 (RIL: 0.1 ± 0.1, RUL: 0.2 ± 0.1) and the final session T_2 (RIL: 0.1 ± 0.1, RUL: 0.2 ± 0.1). Convex hull volume data were fitted with the LMM model in Eq. 1 (see 4.2.9) (RIL R^2 = 0.89, RIL R^2 = 0.78), which revealed a non-significant main effect of sessions for both limbs (p RIL = 0.8, p RUL = 0.3). Non-significant difference between T_0 and T_1 sessions (p RIL = 0.6, p RUL = 0.7), T_0 and T_2 (p RIL = 0.9, p RUL = 0.3), and T_1 and T_2 (p RIL = 0.5, p RUL: 0.2) were found.

4.4. Discussion

The developed system allows to perform a novel rehabilitation protocol for post stroke upper limb motor recovery in a controlled virtual environment. The system is based on commercial technologies and allows to perform bimanual reaching movements in a VR environment while assisting the patient's impaired upper limb movements with the kinematic and forearm EMG of the unimpaired limb. The use of a VR or gaming-based systems (Karamians et al., 2020) and assistance parameters, aims at overcoming some of the limitation of a conventional rehabilitation therapy. First, the system allows to continuously monitor functional motor recovery indicators, thanks to the instrumental evaluations. Second, the system enhances the motivation of the patient to perform the tasks and to complete the therapy, thanks to the assistance procedure which allow to maintain the difficulty of the task at the appropriate level throughout the therapy. In particular, the assistance parameters, adjusted by the therapist block by block depending on performance, set the amount of contribution of the unimpaired limb to the kinematic (proximal assistance) and to the hand gesture (distal assistance) to the impaired one.

The new system is based on a system originally developed by the DLR team for amputees which has been modified according to the indication provided by clinical and technical partners during several user-centred development iterations. A pilot study involving 4 patients, 2 chronic and 2 sub-acute, has been conducted for one month to test the feasibility of the proposed rehabilitation protocol and to setup the system and patient's inclusion criteria for the main study. The ongoing main experimental study aims at characterizing the effectiveness of the provided rehabilitation therapy, comparing the functional recovery of the experimental group with that of a control group performing an equal amount of conventional therapy. At the end of the experimental study, twenty chronic stroke patients will have been recruited in the study, 10 in the experimental and 10 in the control group. The experimental group performs for 2 month every week, 3 times for week, 20 minutes of

VR mirror therapy rehabilitation, while the control group performs a conventional upper limb rehabilitation of the same amount of time.

The first preliminary analysis conducted on 7 participants of the experimental group aimed at assessing the compliance of the therapist's behaviour with the experimental protocol. The therapist was instructed to change assistance parameters at the beginning of each new block according to the performance of the previous block. The instruction was to increase assistance when the block performance was smaller than 80% (9/12 trials) while decrease assistance when performance was greater. We found an average overall performance of 80% ± 10% (sd), which confirms therapist's correct implementation of the experimental protocol.

The functional recovery was then assessed both with clinical and instrumental evaluations performed at the beginning (T_0), midterm (T_1) and at the end (T_2) of the rehabilitation process. To assess the effectiveness of the therapy in enhancing motor recovery, a clinical evaluation index (Fugl-Meyer assessment scale) and two kinematic indexes (the range of movement in the calibration performed at the beginning of each session and the maximum speed achieved during the tasks execution) recorded at T_0, T_1 and T_2 were considered. A significant increase in the upper limb motor function Fugl-Meyer score was observed when comparing the 3 different temporal clinical evaluations. In contrast, this preliminary analysis did not reveal a significant increment in the instrumental indexes. A possible explanation of a mismatch between the clinical and the instrumental evaluations could be due to the small number of patients included in the analysis or to a lack of sensitivity of the specific kinematic metrics used to quantify motor recovery. In the future a more extensive analysis will be required to identify additional metrics based on instrumental data adequate to assess the effectiveness of the rehabilitation therapy. One key advantage of instrumental evaluation metrics is the possibility to obtain an objective and operator-independent evaluation, overcoming one of the limitations of the clinical scales.

Finally, when the experimental study will be completed, a key analysis will compare both clinical and the instrumental evaluations between the experimental and the control groups in order to provide a reliable assessment of effectiveness of the developed VR rehabilitation protocol with respect to the conventional therapy. Moreover, for the experimental group additional analysis will be used to assess the upper limb motor function recovery in terms of limb kinematic and forearm residual muscle activity. For instance, a specific analysis on the hand speed profiles, could lead to identify the presence of several peaks which are often related to movement corrections (Cirstea et al., 2000) occurring because of poor motor planning, variation in motor execution, or task constraints. Moreover, movement smoothness is characteristic of coordinated human movements, and stroke patient movements seem to grow more smooth with recovery (Rohrer et al., 2002).

4.5. Conclusions

A VR mirror therapy has been developed for rehabilitation and assessment of upper limb motor function of hemiparetic chronic stroke patients. The system developed by the DLR in collaboration with the Fondazione Santa Lucia and the NEEEU allows to perform bimanual reaching movements in a controlled environment. A one-month pilot study has been condicted with 4 stroke patients and a main study involving 20 stroke patients is still ongoing. Preliminary results from the analysis of 7 patients of the experimental group have demonstrated an increase in the clinical evaluations scale but additional analyses will be required to assess more systematically indicators of the functional recovery on the instrumental data. Further analysis of the complete dataset will compare both the clinical and instrumental evaluations of the experimental with respect to the instrumental group. These preliminary results provide an initial encouraging indication that the system can be used by patients with stroke upper limb hemiparesis for allow upper limb motor rehabilitation in a controlled environment and to record instrumental data to assess the functional recovery. In the future, the system could become a powerful yet affordable

rehabilitation system to be used in a clinical environment or in a teleoperation scenario directly at patient's home, without any physical intervention of any operator.

5. Toward the development of a Virtual Mirror Therapy using myoelectric control with many muscles

5.1. Introduction

The collaboration between the University of Messina (UniMe), IRCCS SantaLucia Foundation (FSL) and the Deutsches Institute of Robotics and Mechatronics Zentrum für Luft- und Raumfahrt e.V. of Munich (DLR) established for the development and validation of the VVITA system (see chapter 4), aimed at developing a new version of the VVITA system for assisting stroke survivors to improve their motor performance in a bimanual reaching tasks using virtual reality (VR) making a more extensive use of myoelectric control. While in the original VVITA system the EMG signals recorded from the forearm muscles were used to estimate hands gesture, the aim of this new project was to use EMG signals recorded from several muscles of the entire upper limb to estimate hands position. Basically, the role of myoelectric control in VVITA is limited to a few forearm muscles involving only in distal limb movements (e.g., hand closing and opening), while in the new system the focus of myoelectric signal decoding is on the proximal limb movements (e.g., reaching) to exploit the full potential of myoelectric control. As a first step towards the development of the new system, I did an internship at DLR laboratories, where I assessed the feasibility of an approach based on using many forelimb muscles to estimate the hand position, taking advantage of the expertise of the DLR group in myoelectric control and non-linear estimation methods and working under the supervision of Prof. Claudio Castellini.

The goal of this work presented in this chapter is to provide a proof-of-concept of learning assistance using myoelectric control on healthy participants as a model for motor rehabilitation of stroke survivors. The novel assistance approach is thought to extend the capabilities of the existing VVITA system by using myoelectric signals from several muscles acting on one upper limb together with kinematics from the other limb to assist bimanual reaching of virtual objects. The key idea is that myoelectric control on the paretic limb of

stroke survivors may enhance motor recovery because it provides salient feedback on the muscle patterns than need to be re-learned. The feedback on the position of the hand in VR will incorporate an assistance enhancing task performance, thus motivating the patient to continue practicing the exercises. As for VVITA, the level of assistance will be continuously adjusted during the training sessions to maintain a level of performance that motivates the patient to keep practicing. The assistance will depend on the similarity between the muscle patterns generated by the patient when attempting to perform the reaching movement and reference muscle patterns (based on those recorded from the unaffected limb or from healthy participants), thus providing salient feedback on the functional muscle patterns required to perform the task. Moreover, as in VVITA, the mirrored kinematics of the unaffected limb will be used to further enhance performance and keep the patient engaged in the task. In the proof-of-concept validation with healthy participants, the impairment in the generation of functional muscle patterns will be simulated in VR as a perturbation of the hand position estimated from EMGs. Such perturbation is meant to represent a simple model of motor impairment due to stroke simulated in a healthy participant.

The key goal of this initial development is to identify a model with the minimum complexity necessary to obtain an adequate kinematic approximation from the EMG signals. Therefore, model characterization is the core and the most challenging aspect of the project, for this reason the development has required a data analysis phase, in which different machine learning methods have been considered and the best one has been selected comparing the positional estimation errors from an existing reaching database (d'Avella et al., 2006). The first model application consists in extending to 3D movements the linear mapping used in the isometric VR setup used at FSL (Berger et al. 2013) to estimate hand position from EMG signals for several points and several directions for each point. This extension thus implies mapping EMG signals onto hand acceleration rather than isometric force.

Typically, surface electromyography allows to control only a few degrees of freedom. Due to the high dimensionality of human upper limb movements and to the negative influence on control performance of several factors which may change myoelectric signals over time,

such as muscle fatigue, conductivity changes, electrode displacement, differences in the patterns produced by the user or changes in the position and the velocity of the arm (Fougner et al., 2011), linear models may not be sufficient to model adequately the relationship between EMG signals and acceleration especially when using reduced, low-resolution, set of commercially available EMG electrodes.

More sophisticated machine learning techniques may have the potential to overcome these limitations. Therefore, two different machine learning approaches have been proposed (Gijsberts et al., 2014): (1) an incremental regularized variant of least-square regression defined as incremental ridge regression (RR), which allows to balance the trade-off between minimizing the errors and regularizing the solution and continual adaptation to the changes in the signals thanks to occasional updates with a modest amount of novel training data and, (2) a combined incremental RR with Random Fourier Features (RR-RFF) (Rahimi and Recht, 2008b) to solve non-linear problems. Incrementality performance of the methods, one important feature of these methods in addition to the non-linear modeling, has not be investigated and is not presented in this chapter.

To conduct such proof-of-concept validation, I performed both hardware and software development and integration. I developed a novel myoelectric control approach to estimate hand position from EMG signals recorded from many upper limb muscle extending machine learning approaches developed at DLR for the estimation of hand gestures. I then conducted a preliminary analysis of existing reaching data to validate the approach. To record the EMG signals needed to estimate hands positions, a more sophisticated EMG recording system with higher number of sensors was required. A wireless 16 channels system (Trigno, Delsys Inc., USA) has then been integrated in the VR system to replace the 8 channels EMG myoband acquisition system (Thalmic Labs, Ontario, Canada). A new VR environment and acquisition software was also developed to perform the experimental validation.

The main aim of this chapter is to report the methods developed for the estimation of hand position from EMG signals and the results of the preliminary analysis performed on the unimanual reaching database previously recorded at FSL (d'Avella et al., 2006) to validate the feasibility of the proposed approach. Several analyses were performed to estimate the best machine learning method and the optimal parameters which allow to reliably predict the desired outcomes. The online validation and the new version of the VVITA software will not be presented and discussed in this chapter, since some such developments are still ongoing.

5.2. Methods

This section first introduces the proposed approach to estimate hand position from EMG signals and to overcome the possible limitations of the approach in an online usage. Three different regression methods, standard linear regression and two machine learning methods, have been considered. Then, an offline validation procedure to test the feasibility of the proposed approach is presented. The procedure has been developed to identify the regression method and the signals preprocessing parameters with the minimum complexity necessary to obtain an adequate kinematic approximation from the EMG signals.

5.2.1. Upper limb end-point estimation from EMG

The proposed approach, extending the existing VVITA system (see chapter 4), combines assistance from the mirrored kinematics of one upper limb with the predicted kinematics from EMG signals from many muscles of the same limb. EMG signals collected from up to 16 muscles of one arm (denoted as 1) $[m_1(t)]$ are used to estimate the instantaneous hand position either directly or along a pre-recorded trajectory $\{f[m_1(t)]\}$. Such estimated hand position is combined, as for the current VVITA system, with the recorded position of the

real hand $[x_1^R(t)]$ and the mirrored position of the other hand $\{T[x_2^R(t)]\}$ to provide visual feedback in the VR $[x_1^V(t)]$:

$$x_1^V(t) = \delta\{\alpha x_1^R(t) + (1-\alpha)T[x_2^R(t)]\} + (1-\delta)f[m_1(t)]$$

where x_1^V and x_2^V indicates respectively the virtual position of hand 1 and 2 in VR and x_1^R and x_2^R the position of the real hands. m_1 indicates the electromyographic activity of recorded from the muscles of limb 1. T indicates a mirror transformation of the kinematic of limb 2. f indicates the model, to be developed, with the minimum complexity necessary to obtain an adequate kinematic approximation. δ and α represent the coefficients through which it is possible to select the type and amount of movement assistance provided to limb 1. The combination coefficients are meant to be adjusted manually during the training.

This approach assumes that it is possible to estimate hand position from EMG signals approximately yet reliably and with an adequate accuracy without a realistic musculoskeletal model. The idea is to test the feasibility of extending the approach for myoelectric control of a virtual end effector in isometric condition based on a linear mapping of EMG into force applied to a point mass developed at FSL (Berger et al., 2013) to the estimation of hand position during bimanual reaching movements. The mapping is estimated at different locations and smoothly interpolated with the workspace. The motion of the end-effector is then simulated as a point mass subject to a force estimated from EMGs.

An estimation of hand position from EMG signals during reaching movements starting from several initial positions and towards target in several directions for each position can be achieved by approximating the hand as a point mass and finding, at each starting position, a local map H_P between muscle activities and accelerations. This simple approach extends the method used in isometric conditions in which the local map is between muscle activities and acceleration.

$$F(t) \simeq H_p(x, \dot{x})m \tag{1}$$

$$F(t) = Mass_{arm}\ddot{x} \tag{2}$$

$$\ddot{x} \simeq \frac{F(t)}{Mass_{arm}} \simeq \frac{H_p(x, \dot{x})}{Mass_{arm}} m = H_p{}'m \tag{3}$$

$$H_p' = \frac{H_p(x, \dot{x})}{Mass_{arm}} \tag{4}$$

$$\ddot{x} \simeq H_p{}'m \tag{5}$$

Where matrix H_P is the position dependent mapping between muscle activity m and force f, estimated in the isometric approach using linear regression. $x, \dot{x}, \ddot{x}$ are the position, velocity and acceleration vectors of the end effector (hand) and M_{arm} is the mass of the arm. From the second law of dynamics, an equation which relates the acceleration to the force and consequently a relation between acceleration and muscle activity can be found.

To develop the model a calibration procedure is required. A task in an initial calibration phase consists of multiple point-to-point unimanual reaching movements towards different targets in a 3D space. To estimate H_P, at a specific initial position p, a linear regression (LR) can be applied to fit muscle activity to hand acceleration. To find a mapping H incorporating the dependence on the initial position, it is possible to interpolate all the position specific maps H_P (Sharif Razavian, 2017). An alternative way, to estimate H_P, is to use machine learning approaches to find a non-linear relation between acceleration and muscle activity. Incremental machine learning methods enforcing regression (Gijsberts et al., 2014) using a 16 or higher dimensions input space, i.e., one coordinate for each EMG electrode, and the acceleration as set of real values for the regression can also be used.

Therefore, in this project the reconstruction performances of the LR method were compared with an incremental variant of RR, which represent a regularized variant of least-squares regression and with RR-RFF, a non-linear incremental learning method which combine incremental RR with Random Fourier Features. The analysis presented in this chapter will

investigate the effect of the different models without studying the effect of the incrementality.

RR method builds a linear model of the input space x (Eq. 6). Given a training set of m real-valued input-output pairs $x_i \in \mathbb{R}^n, y_i \in \mathbb{R}$, RR determines the optimal weight vector $\widehat{\boldsymbol{w}}$ that minimizes the Eq. 7, where λ is a hyper-parameter that balance the tradeoff between minimizing the errors and regularizing the solution.

Since the practical use of RR is limited due to its linearity a kernel-based approach was developed (Gijsberts et al., 2014). In the Kernel Ridge Regression (KRR), the limitation is circumvented using the so-called kernel trick, which allows the algorithm to be performed implicitly in a potentially infinite dimensional feature space. As consequence the model takes the form of a weighted summation of kernel evaluations with the training samples (Eq. 8). Kernels drastically increases the capacity of RR, but at the cost of a dependency on the number of training samples of the computational requirements for predictions and incremental updates. This dependence can be avoided by approximating the kernel function with a finite dimensional feature mapping as for instance a finite number of random samples in the Fourier domain of shift invariant kernel functions (Eq. 9), which produce an unbiased estimate of a kernel if $\boldsymbol{\omega}$ has an appropriate distribution and b is drawn from a uniform distribution from 0 to 2π. The kernel approximation can be made more precise by averaging multiple RFFs $\boldsymbol{z_\omega}$, so that for D features it isis Eq. 10, where each feature z_i independently draws an individual ω_i and b_i. Therefore, to make RR non-linear, it thus sufficient to replace each input vector $\mathbf{x_i}$ with its random projection z($\mathbf{x_i}$). The accuracy of the algorithm approximation will increase as the number of feature D, but at the cost of a higher computational requirement.

$$f(x) = w^T x \tag{6}$$

$$\arg\min_{\boldsymbol{w}} \frac{\lambda}{2}\|\boldsymbol{w}\|^2 + \frac{1}{2}\sum_{i=1}^{m}(y_i - f(x_i))^2 \tag{7}$$

$$f(x) = \sum_{i=1}^{m} c_i k(x, x_i) \tag{8}$$

$$\boldsymbol{z_\omega}(\boldsymbol{x}) = \sqrt{2}\cos(\boldsymbol{\omega}^T \boldsymbol{x} + b) \tag{9}$$

$$\boldsymbol{z}(\boldsymbol{x}) = \frac{\mathbf{1}}{\sqrt{\boldsymbol{D}}} [\boldsymbol{z_1}(\boldsymbol{x}), \dots, \boldsymbol{z_D}(\boldsymbol{x})]^{\boldsymbol{T}} \tag{10}$$

Hand position $\hat{x}(t)$ is estimated through numerical integration. If this simplification does not provide an appropriate estimate, a more accurate forward dynamics model can be taken into account as indicated in Eq. 11. The equation represents a mass spring damper system with an additional gravitational component g. M_{cursor} is point mass whose position in VR is represented by a spherical cursor and b and k are respectively the coefficient of the damper and of the spring. Finally, the estimated position (Eq. 12) can be used both directly (black line) or can be amplified (red line) and/or projected into a pre-recorded reference trajectory (blue line), to give VR feedback.

$$H\big(x(t)\big)m(t) \simeq f\big(x(t), \dot{x}(t), m(t)\big) = M_{cursor}\ddot{x} + b\dot{x} + k(x - x_0) + M_{cursor}g \tag{11}$$

$$P_{x_{ref}}(\hat{x}) = x^V(t) \tag{12}$$

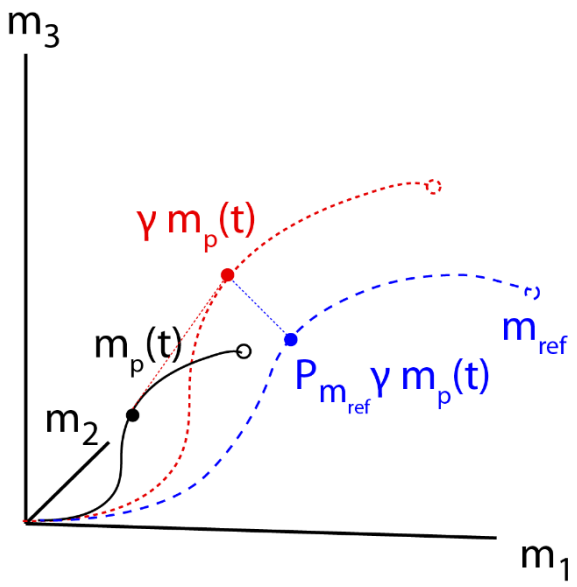

Figure 5.1. Transformation of estimated trajectory. To assist the movement in a certain direction, a vector $\boldsymbol{x_{ref}}$ is identified. The vector can be used to project the instantaneous trajectory into its direction in the kinematic space $\boldsymbol{P_{x_{ref}}\gamma x_p(t)}$. If it is necessary, $\boldsymbol{\gamma}$ can be used to scale $\boldsymbol{x_p}$ size before projecting on $\boldsymbol{x_{ref}(t)}$.

5.2.2. Offline validation analysis

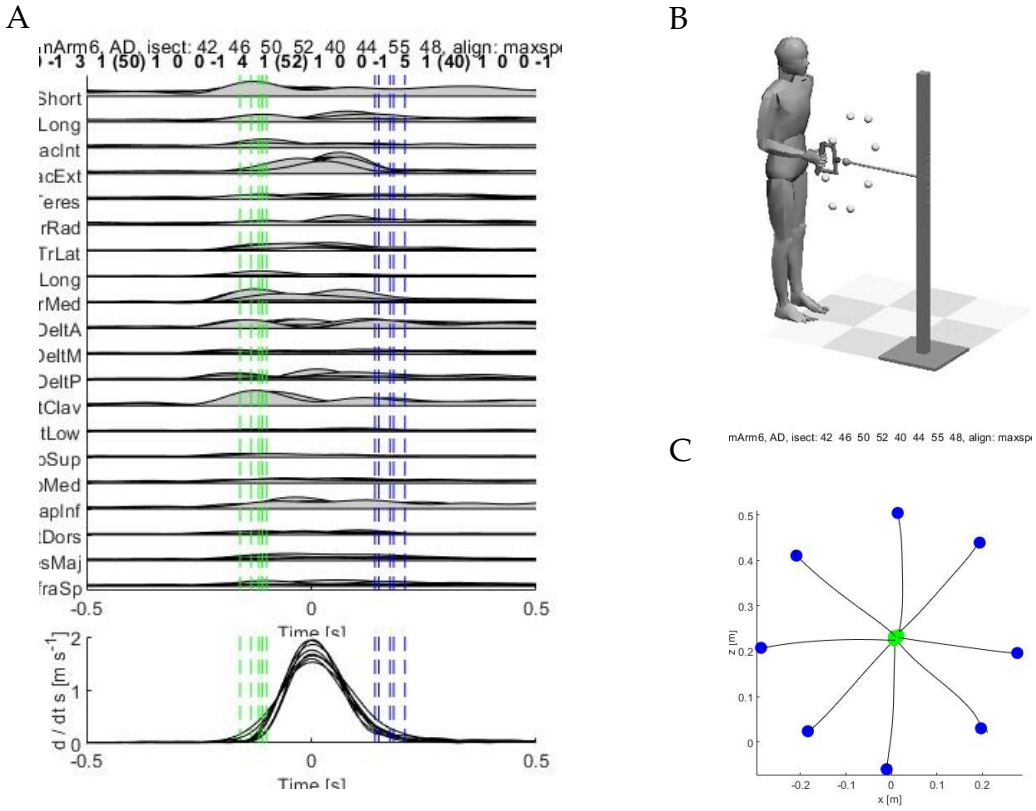

Figure 5.2. Example of one trajectory for each of the 8 frontal targets and the relative EMG signals previously recorded at FSL (d'Avella et al, 2006). (**A**) top panel shows the pre-processed EMG signals and for each trial the movement onset (green vertical dashed lines) and offset (blue vertical dashed lines) time events. (**A**) bottom panel shows the kinematic velocity profile for each reported trial and the onset and offset events. (**B**) shows the experimental setup: standing subjects performed fast-reaching movements from a fixed starting position (corresponding to a posture with the arm vertical along the body and the forearm horizontal) to eight targets in the frontal plane (centre-out movements). (**C**) shows the kinematic of the 8 selected trials from centre (green sphere) to targets (blue spheres).

To validate the feasibility and reliability of the proposed approach, an off-line validation analysis was performed using EMG and kinematics data for point-to-point reaching movements previously collected at FSL (d'Avella et al., 2006). Standing subjects performed fast-reaching movements from a fixed starting position (corresponding to a posture with

the arm vertical along the body and the forearm horizontal) to eight targets in the sagittal plane and eight targets in the frontal plane (center-out movements) and fast-reaching movements from the peripheral targets back to the starting position (out-center movements). From the collected data, the eight targets in the frontal plane were selected (Fig. 5.2B). For each trial only the center-out movement kinematic from the starting position (Fig. 5.2C, green sphere) to each target (Fig. 5.2C, blue spheres) was selected to be used as data for the validation analysis. Five repetitions for each target were performed. The position of a marker placed on a sphere attached to a handle gripped by the participant was acquired with an electromagnetic motion-tracking system (Fastrak, Polhemus, Colchester, VT) while the EMG from 20 muscles (latissimus dorsi, teres major, infraspinatus, trapezius inferior, trapezius medial, trapezius superior, pectoralis clavicular, pectoralis low, deltoid anterior, deltoid medial, deltoid posterior, biceps short, biceps long, brachii internal, brachii external, pronator teres, brachioradialis, triceps lateral, triceps long, triceps medium) were acquired with two 16-channel EMG systems (Bagnoli-16, Delsys, Boston, MA). Both kinematic and EMG raw data were pre-processed. Kinematic data recorded at 120Hz were filtered with a low pass Butterworth filter (cutting frequency = 10Hz, order = 5) and normalized to the maximum norm of the kinematic vector (3 channels) found for each trial. EMG data recorded at 1000Hz were first high pass filtered (Butterworth, cutting frequency = 10Hz, order = 4) and then rectified. EMG signals were also low pass filtered and resampled at 120Hz to match kinematic sampling frequency. The cut-off frequency of the applied low pass filter was identified maximizing the goodness of the fit (R^2) between the acceleration estimated from the recorded position and the acceleration predicted from EMG signals with the different methods. To prevent the negative impact on the estimation of any delay between the time samples of the kinematic and EMG data, the optimal time difference between the two dataset was identified. The optimal time difference selected was that maximizing the R^2 of all compared methods.

The validation analysis aimed at comparing three different regression methods, i.e. a simple linear regression (LR), a ridge regression (RR), and a machine learning method based on

ridge regression and random Fourier features (RR-RFF), to estimate hand acceleration from recorded EMGs. The validation relied on a cross-validation approach. The different regression models were fitted on random subsets of the data and their prediction performances tested on the rest of the dataset. For each target, 3 repetitions were selected to train the regression models (3 trials x 8 targets = 24 trials) and 2 repetitions were selected to test the predictions (2 trials x 8 targets = 16 trials). The entire dataset was randomly partitioned 10 times and the procedure repeated to achieve a more robust assessment of model performance.

5.2.3. Validation of the regression model

Once the best model was found, its predicted acceleration was integrated twice to compute the estimated position. In the following, I will refer to this predicted position as modPos. To validate the estimation, modPos was compared with the recorded position (truePos). To quantify the effect of data noise on the integration and derivation procedures, the acceleration estimated deriving twice truePos was integrated twice in order to obtain the position (estPos). The different end point positions, for each trial of the testing dataset were compared in terms of angle error and positional error.

5.2.4. Statistical analysis

The dependence of the estimate of the position (Y) on the estimation method (*Md*) and on the target (*Ta*) and therefore the movement direction was tested with a linear mixed models (LMM). The experimental factors were treated as fixed effect factors with categorical (dummy) variables. Data were fitted with the model in Equation 13.

$$Y = u_0 + \alpha_0 Ta + \beta_0 Md + \epsilon \quad (13)$$

where u_0 represents the individual intercept, the coefficients α_0 and β_0 represent fixed-effect, thus the modulation of the response variable by the experimental factor *Ta* and *Md*. As the predicted position is a continuous variable, data were fit with a LMM (Matlab, function *fitlme*) using maximum likelihood with Laplace approximation.

5.3. Results

Several analyses were performed to characterize the feasibility of the estimation process and to find the best parameters to reliably predict hand acceleration and consequently hand position from EMG signals recorded from upper limb muscles.

The first analysis allowed to identify the best cut-off frequency for the low-pass filter applied to the EMG signals after a high-pass filter (Butterworth 4^{th} order, cut-off frequency 10Hz) and rectification and the best delay between EMG and kinematics samples. In figure 5.3, ten different cut-off frequencies, from 1 to 10 Hz in steps of 1 Hz (different line colours), were used to low-pass filter (Butterworth) the EMG signals. For each of the 3 predicted variables (3 components of the hand acceleration), the mean of the goodness of the fit R^2 for all compared ML methods and training datasets obtained with the cross-validation approach, is reported as a function of the temporal shift applied at the EMG (Fig. 5.3A, B, C). Due to the temporal delay induced by the acquisition system during signals recordings, and to the electromechanical delays due to the muscle excitation-contraction process, the prediction may not be reliable. Therefore, EMG signals were shifted forward with respect to the kinematics by 0.1s to find the best delay which maximize the cross-validation R^2 for all the ML methods.

Since the regression was performing poorly especially for the RR (max $R^2 = 0$) and RR-RFF (max $R^2 = 0.024$) methods, the same analysis was performed with EMG data normalized to the maximum norm of each vector of EMG samples (Fig. 5.3D, E, F). All the analyses were performed from the onset to the offset of the movement (see Fig. 1 green and blue dashed lines). Tab 5.1 shows, for both the normalized data and not, the highest R^2 values found for each regression method in the spanned range of the parameters. RR-RFF shows the best performance in terms of goodness of the fit when the regression was performed with the normalized data and when the EMG signals were low-pass filtered with a 5 Hz cutoff

frequency Butterworth filter and shifted by 0.1s. These optimal values of the parameters (EMG filtering cutoff frequency and temporal shift) were used for further analyses.

A

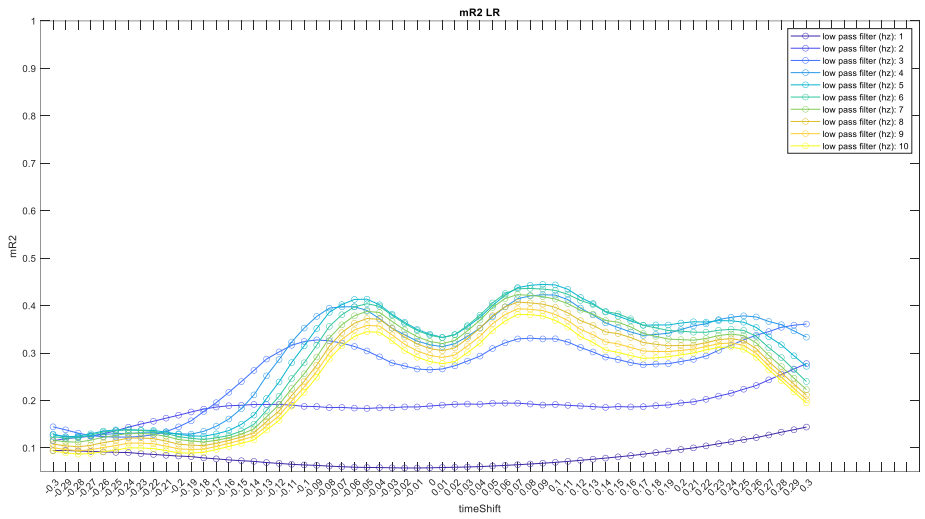

B

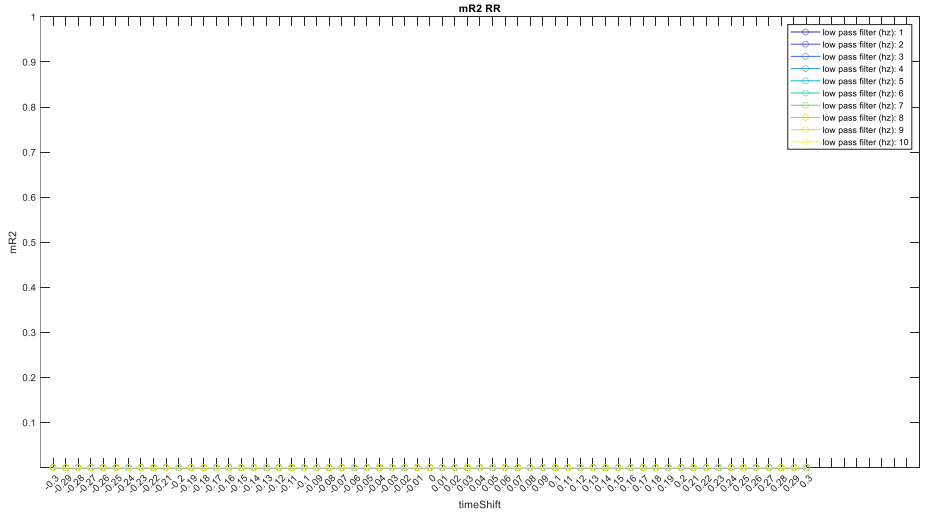

C

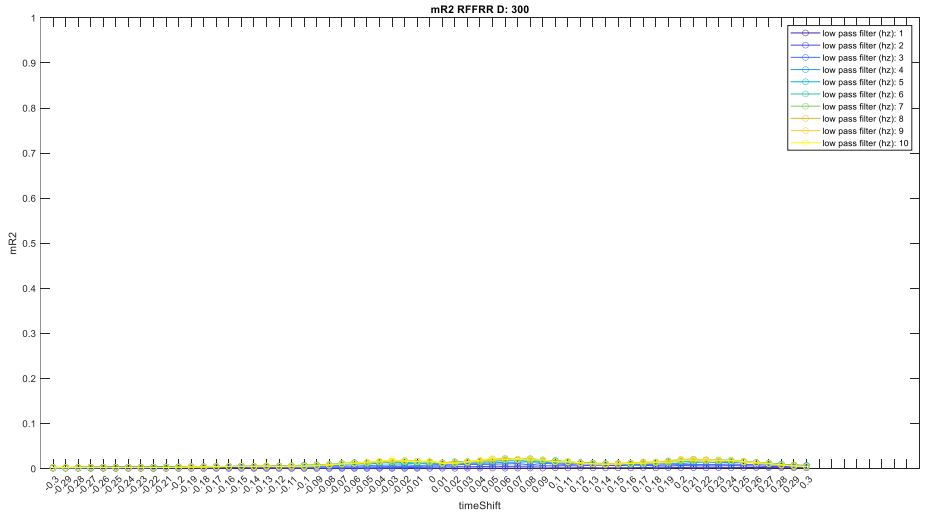

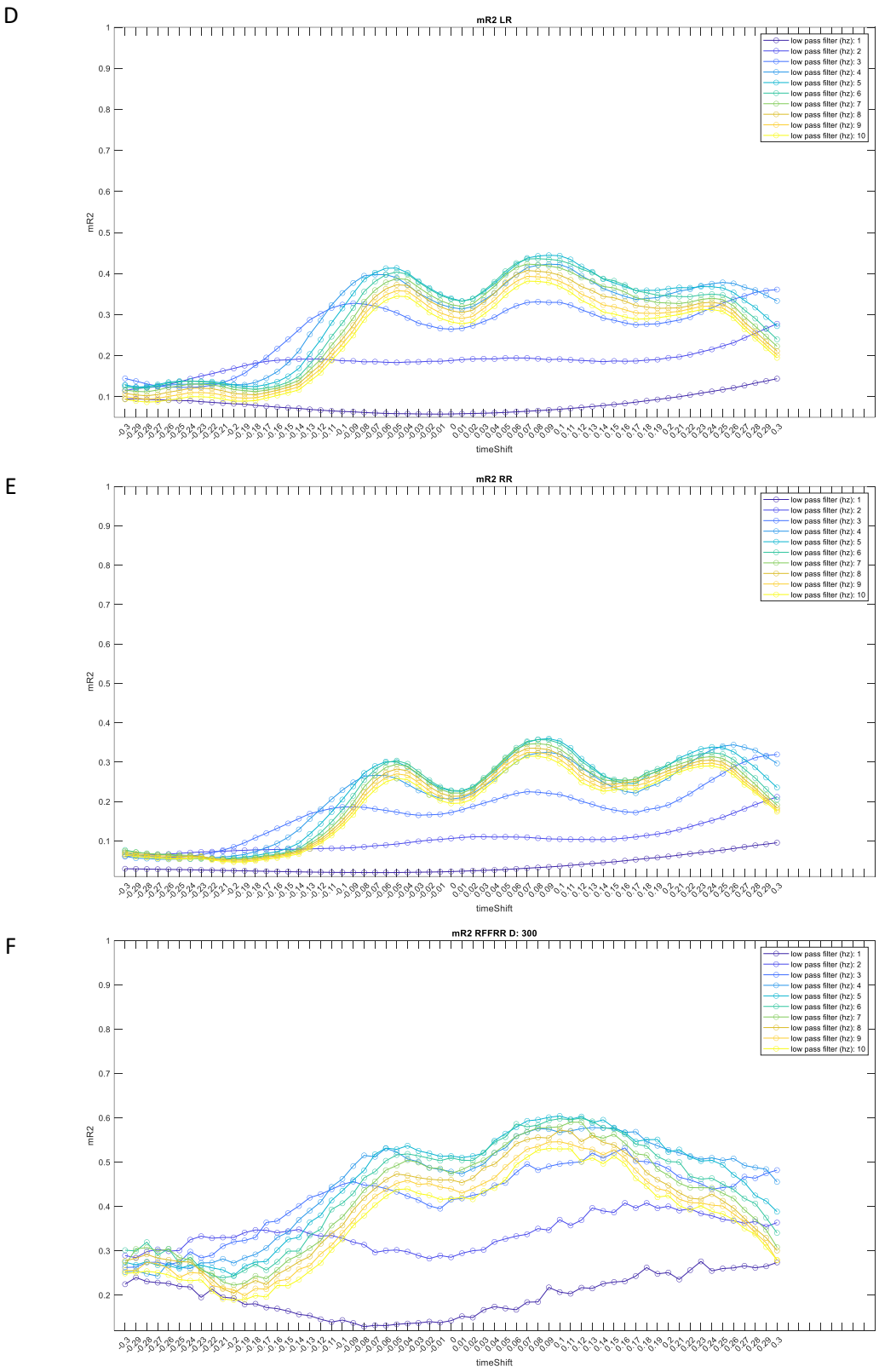

Figure 5.3. Span filter and temporal delay. The figure shows the simulation process used to define the best Butterworth low pass filter cutting frequency and the time shift to apply to the EMG signals. (**A**, **B**, **C**) represent the results for the three methods: LR (**A**), RR (**B**), RR-RFF (**C**) for the non-normalized data, while (**D**, **E**, **F**) represent the same results for the normalized data. The spanned cutting off frequency were from 1 to 10Hz with a step size of 1Hz, while the spanned temporal shift were from -0.3 to 0.3s with a step size of 0.1s.

	Not normalized data			Normalized data		
Max R2	0.445	0	0.024	0.445	0.36	0.604
Filter Low Pass (Hz)	5	10	10	5	5	5
Temporal shift (s)	0.09	0.07	0.07	0.09	0.09	0.1

Table 5.1. Span filter and temporal delay. Table shows the low pass filter cutting frequency and temporal shift parameters which maximize R^2 for both the not normalized (left column) and the normalized datasets (right column).

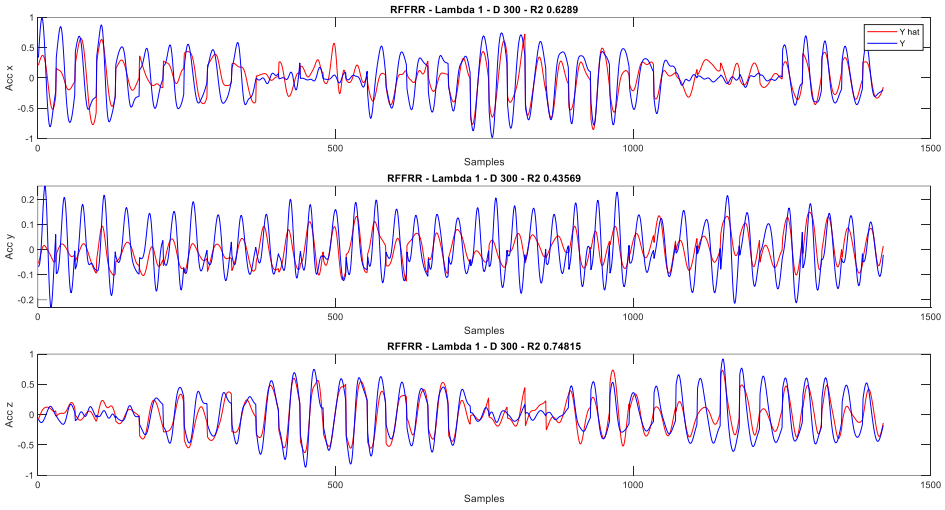

Figure 5.4. Example of RR-RFF acceleration reconstruction. The figure shows the acceleration estimated with the low pass filter cutting frequency and the temporal shift parameters found with the first simulation process (red line) and the acceleration given by the second derivative of real recorded position (blue lines) for the 3 Cartesian axes (x, y, z).

Figure 5.4 shows the acceleration reconstruction performed with the selected pre-processing parameters. Each of the 3 components of the hand acceleration computed by numerical differentiation of the recorded position samples (blue line) and predicted by the RR-RFF method (red line) are plotted for one of the cross-validation datasets.

To study the feasibility of an online estimation process where the prediction should independently discriminate between movement and resting phase, a larger temporal interval was considered in order to include in the prediction both resting and reaching phases. A new analysis was performed starting from a given time interval *t* before and after movement onset and offset (green and blue dashed lines Fig. 5.1). Table 5.2 shows the R^2 found for each method and for each time interval considered. The best result for all the methods was obtained with a time interval equal to zero. However, since the analysis aims at finding the best procedure to predict reliable estimations in an operative scenario, the delta time selected was t = 0.1s, which balances the trade-off between performance reconstruction and temporal interval width.

***t* (s)**	**0**	**.05**	**.1**	**.2**	**.3**	**.4**
Max R^2 for LR	0.445	0.379	0.336	0.294	0.266	0.245
Max R^2 for RR	0.36	0.315	0.285	0.257	0.237	0.222
Max R^2 for RR-RFF	0.604	0.55	0.508	0.461	0.436	0.419

Table 5.2. Span temporal delay. Table shows the R^2 performance for the different temporal interval considered.

Next, an analysis was performed to define the optimal hyper parameter λ, i.e. maximizing the goodness of the fit, in both the RR and RR-RFF methods. Figure 5.5 shows the mean R^2, computed on both training (blue lines) and testing datasets (red lines) for several λ values selected from 0 to 3 with a step size of 0.1. For each condition (training or testing) and each method, the λ value which maximize the R^2 was selected to estimate the acceleration and the prediction evaluated on one of the testing datasets was shown in Figure 5.5.

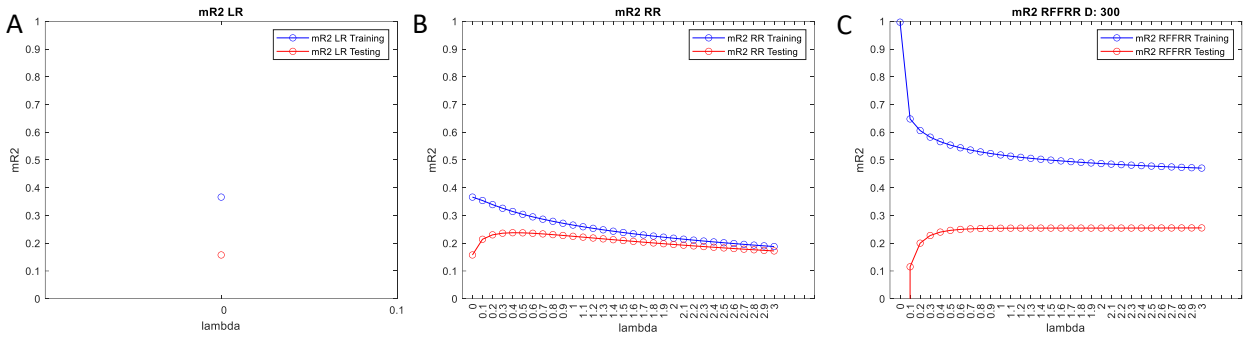

Figure 5.5. Span lambda. Figure shows the mean R^2 for the three methods LR (**A**), RR (**B**), RR-RFF (**C**) obtained with the simulations estimated pre-processing parameters for both the training dataset (blue circles) and the testing one (red circles).

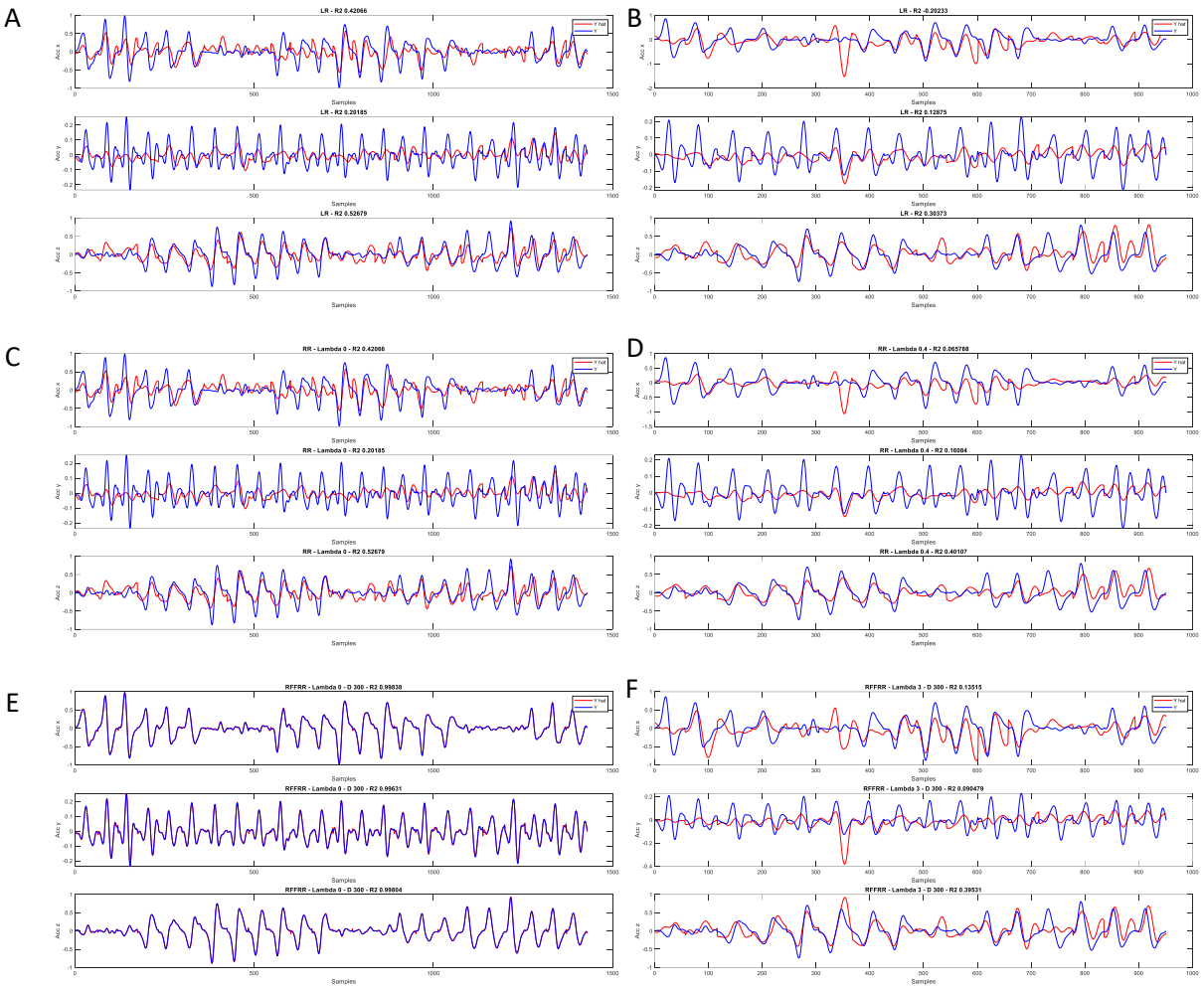

Figure 5.6. Best acceleration reconstruction with respect to the R^2 performance estimated spanning lambda from 0 to 3 (step size 0.1). Figure shows the R^2 performances for the machine learning methods: LR (**A**, **B**), RR (**C**, **D**), RR-RFF (**E**, **F**). Left column reports an example of reconstruction for one of the training datasets selected, while right column shows the reconstruction for one of the testing dataset selected. Each plot in the figure shows the acceleration estimated with the parameters found with the previous processed simulations (red line) and the acceleration given by the second derivative of real recorded position (blue lines) for the 3 Cartesian axes (x, y, z).

RR-RFF was the best method in terms of goodness of the fit both for the training and the testing datasets. Therefore, a final analysis was performed to find the optimal choice for the Gaussian basis functions bandwidth σ, used in the RR-RFF method. The simulation spanned several values for σ from 0 to 0.2 with 0.05 step size. Moreover, to span a larger λ interval the simulation also spanned the values from 0 to 1500 with step size of 100 (Fig. 5.7A). A more detailed simulation, spanning with a smaller step size the values around the most

performing ones in terms of goodness of the fit, is shown in Fig. 5.7B. The maximum R^2 for the training datasets was 0.689 found with σ equal to 0.135 and λ equal to 200, while the maximum R^2 found for the testing datasets was 0.397 with σ equal to 0.136 and λ equal to 390.

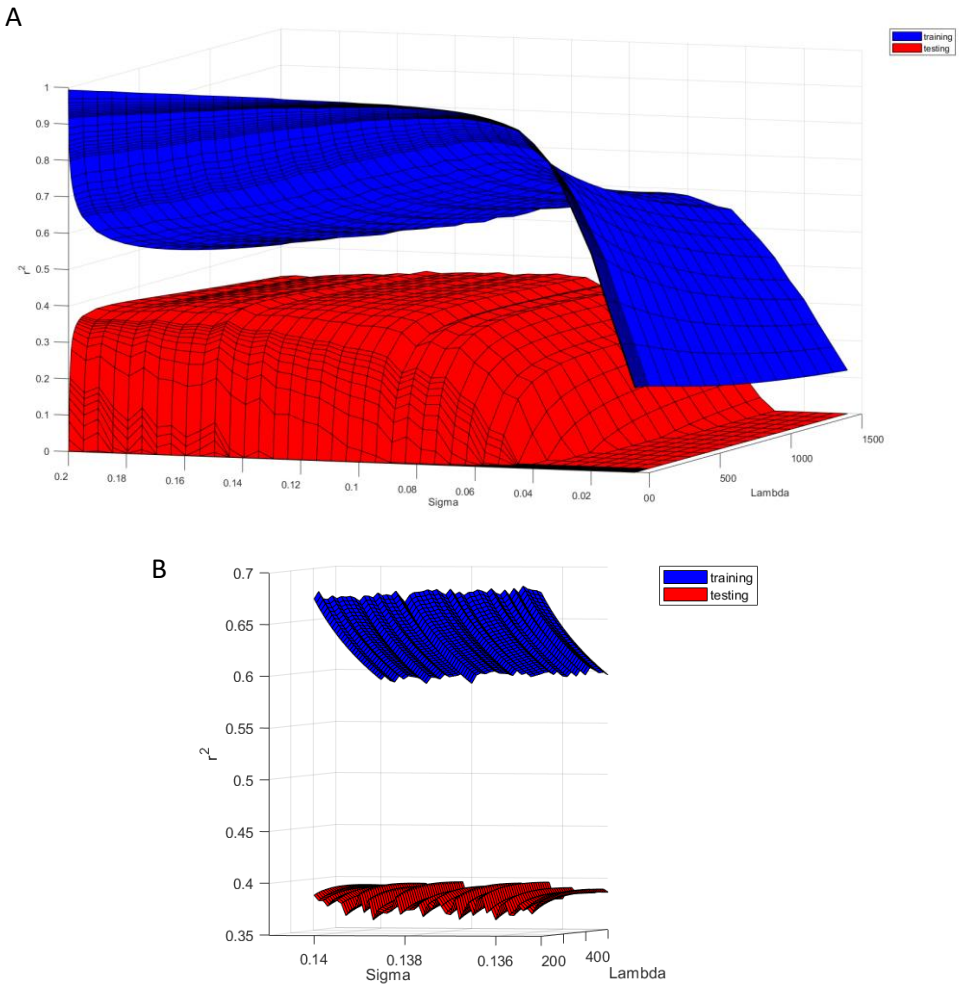

Figure 5.7. Span sigma and lambda. Figure shows the R2 performance for the last simulation, which spans simultaneously the sigma and lambda parameters. (**A**) Larger parameters span. (**B**) Specific span selected to maximize the goodness of the fit.

Lastly, *modPos*, the position reconstructed integrating the predicted acceleration was compared to *estPos* the position estimated integrating the acceleration estimated from the real position and to *truePos* the real position for one of the testing datasets. Fig. 5.8 shows, for one of the testing datasets, two examples of estimated trajectories. Fig. 5.8A shows a good example of *modPos* estimated trajectory (red line), while Fig. 5.8B shows an example

of poor reconstruction. The figure shows in the left column a 3D plot of the estimated trajectories, from the starting point (green sphere) to the target (blue sphere), while right column shows single axis components.

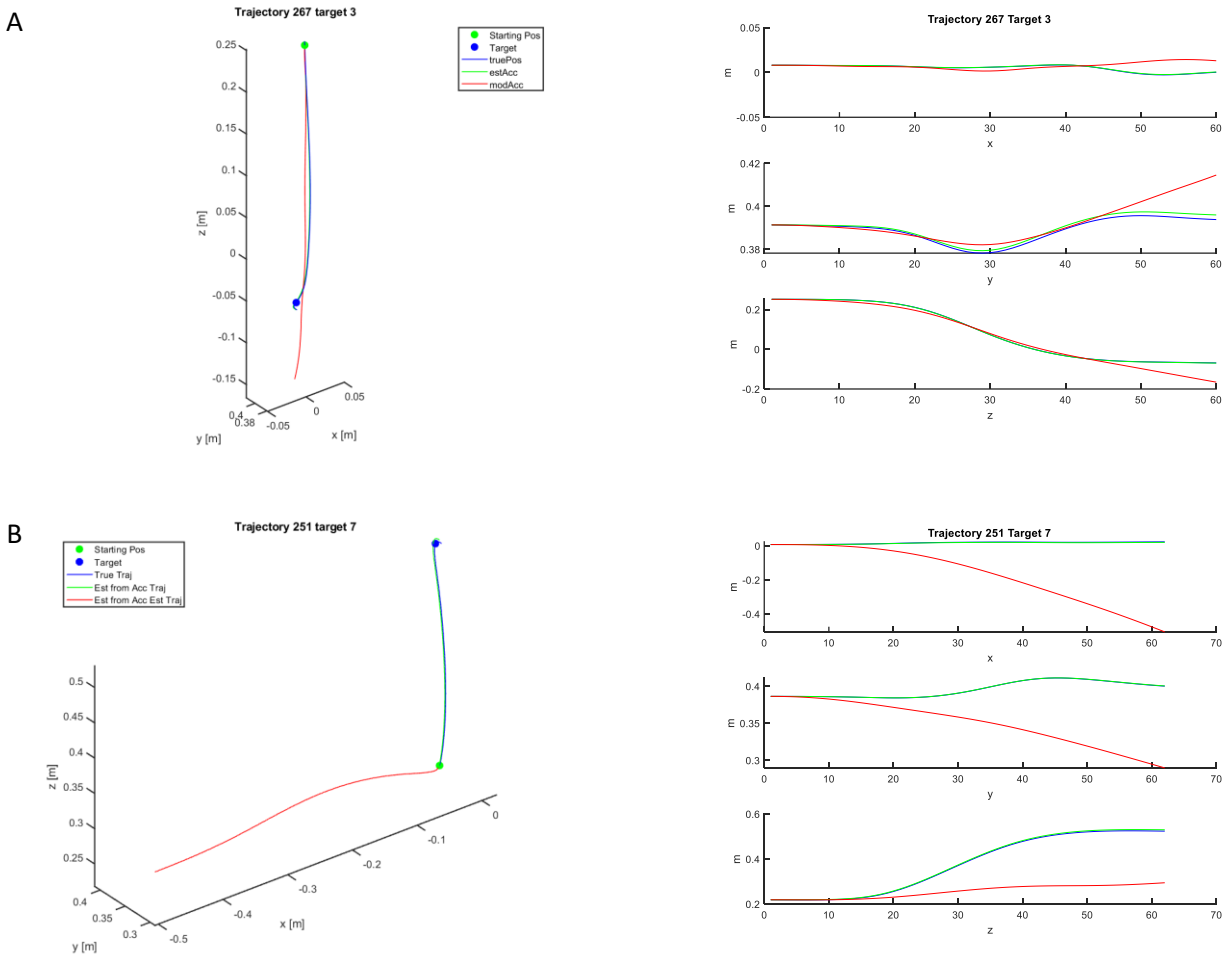

Figure 5.8. Trajectory reconstruction. Figure shows position reconstruction examples for one of the testing datasets created to perform the analysis. (**A**) Example of good modPos estimation (red line). (**B**) Example of bad modPos estimation (red line). For each row the left column shows in a 3D plot the estimated trajectories (truePos blue line, estPos green line, modPos red line) from the starting point (green sphere to the target (blue sphere). Right column shows the estimated trajectories for each axis.

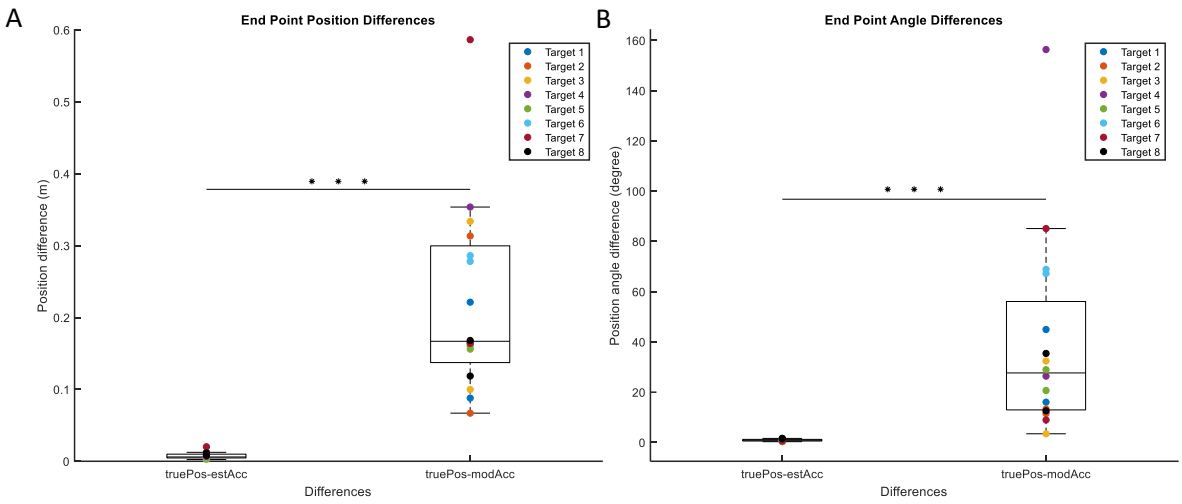

Figure 5.9. End point estimations error. (**A**) End point position differences shown as the difference between the truePos and the estPos end points (truePos-estPos) and the difference between the truePos and the modPos (truePos-modPos). (**B**) End point angle differences shown as the end point angle error between the truePos end point vectors and the estPos end point vector (truePos-estPos) and the angle error between the truePos end point vector and the modPos end point vector (truePos-modPos). Different colors dots show different targets. Statistical difference significance is reported as *** = 0.001, ** = 0.01 and * = 0.05.

The mean spatial error, on the trials of one of the testing datasets, between *truePos* and *estPos* (mean ± sd = 0.007 ± 0.005 (m)) and between *truePos* and *modPos* (mean ± sd = 0.222 ± 0.132 (m)) is shown as boxplot in Fig. 5.9A. Mean spatial error data were fitted with the LMM model in Eq. 13 (R_2 = 0.66), which revealed a significant main effect of sessions ($p < 0.001$). Statistical difference between methods is reported in the figure as *** = 0.001, ** = 0.01, * = 0.05. No statistical differences were observed for between targets ($p = 0.48$).

Fig. 5.9B shows the mean end point angular error computer between *truePos* and *estPos* vectors (mean ± sd = 0.91 ± 0.42 deg) and between *truePos* and *modPos* (mean ± sd = 40 ± 39 deg) trajectories for each trial of the testing dataset. Mean end point angular error data were fitted with the LMM model in Eq. 13 (R^2 = 0.49), which revealed a significant main effect of session ($p < 0.001$). Statistical difference between methods is reported in the figure as *** = 0.001, ** = 0.01, * = 0.05. No statistical differences were observed for between targets ($p = 0.26$).

The angular error and the position error were larger when position was estimated with our model. However, for some targets the estimation was closer to the *truePos*.

5.4. Discussion

The research that I have conducted during my internship at DLR has contributed to the initial development of a new version of the VVITA system, which allows to perform a virtual mirror therapy for the rehabilitation of stroke patients' the upper limb, based on the use of a VR system and myoelectric control. The new system aims at extending the capabilities of the current VVITA system, allowing the reconstruction of the upper limb movements using EMG signals from many upper limb muscles. Therefore, the aim of this work was to evaluate the feasibility and reliability of the approach using machine learning methods and a high number of muscles to perform myoelectric control of reaching movements in VR.

In this chapter, a validation analysis on an unimanual reaching dataset previously recorded at the FSL (d'Avella et al., 2006) was presented. The analysis aimed at assessing the feasibility of the approach and to define which regression method better predicts the kinematic from the EMG, in order to be used online in a VR scenario in the next step of development. I used and compared 3 different regression methods to locally approximate the hand as a point mass and to find a local map H_P between acceleration and muscle activities. The first and simplest method considered was linear regression (LR), the second was a regularized variant of the LR called ridge regression (RR), while the third one was a non-linear machine learning method called ridge regression with random Fourier features (RR-RFF), which combines the RR with random Fourier basis functions. Several analyses, based on a cross-validation procedure, allowed to establish the feasibility of the approach, to estimate the most reliable method and to find signal preprocessing and machine learning parameters, which perform best in terms of goodness of the fit R^2.

The first analysis evaluated EMG pre-processing parameters. While for the kinematic, signals were only filtered (low pass Butterworth, cutoff = 10Hz, order = 5) to preprocess data, for the EMG I needed to find the optimal low-pass filter cutoff frequency to apply, after high-pass filtering (Butterworth, cutoff = 10Hz, order = 5) and rectifying the signals, to obtain the best prediction. Moreover, I found that due to the different delays in the acquisition of EMG and kinematic data to the electromechanical delays due to the muscle excitation-contraction process, a temporal shift was required to align the kinematic with the EMG and to obtain the best reconstruction. The analysis also investigated the effect of data normalization. Therefore, through these analyses I found that the best preprocessing procedure for the EMGs was to apply after the high-pass filter and the rectification, a low-pass filter with a 5 Hz cutoff frequency. I also found that a temporal shift of 0.1 s between kinematic and EMG data was the optimal value needed in order to obtain the best reconstruction. Finally, while no differences were observed for the LR method, normalizing data to the maximum norm for each vector of EMG signal at each time sample, improved the performance of the RR and RR-RFF methods (Fig. 5.2).

The second analysis reproduced an online operative scenario where the regression is be performed on a larger time interval than the one used in the first analysis, which is defined as the time interval between movement onset and offset. Therefore, I performed a cross-validation analysis where I spanned several time interval ranges enlarging the movement onset to offset range. I found that a extending the time interval before movement onset and after movement end by 0.1 s was a reasonable trade-off between performance reconstruction and width of time interval.

After evaluating the best pre-processing parameters, I performed a third analysis to define the optimal regularization parameter λ which maximize the goodness of the fit. I found that the best mean R^2 evaluated on both the training and the testing datasets, which were obtained with a cross-validation approach, was achieved with the RR-RFF method (Fig. 5.4). I then decided to select and use the RR-RFF method to predict the position of the hand and

to refine the research of both the optimal λ parameter and the Gaussian basis functions bandwidth σ. Therefore, I performed a final analysis to simultaneously estimate both the optimal values for λ and σ parameters. The best result obtained for the training datasets was $R^2 = 0.689$ found with σ equal to 0.135 and λ equal to 200, while the maximum R^2 found for the testing datasets was 0.397 with σ equal to 0.136 and λ equal to 390. The accelerations predicted with the RR-RFF method (*modPos*) were integrated to obtain hand position and the reconstruction was compared with the real one (*truePos*) and the one estimated from the acceleration estimated directly from the real position (*estPos*). The comparison between the end point spatial error and angular error on one of the testing datasets. A mean end point spatial error of (mean ± sd = 0.007 ± 0.005 (m)) between the truePos and estPos and a mean spatial error of (mean ± sd = 0.222 ± 0.132 (m)) between *truePos* and *modPos* were estimated. Statistical differences between the errors were noticed ($p < 0.001$). No statistical differences were observed for the different targets. A mean end point vector angle error of (mean ± sd = 0.91 ± 0.42 deg) between the truePos and estPos trajectories and a mean end point vector angle error of (mean ± sd = 40 ± 39 deg) between truePos and modPos trajectories were estimated. Statistical differences between the errors were noticed ($p < 0.001$). No statistical differences were observed for the different targets.

The overall results highlight some of the limitations of the approach. However, for some trials the quality of the estimation is acceptable in terms of spatial and angular error of the end point vector. Moreover, the proof of concept aims to study the feasibility of the approach to estimate movement intentions to be projected and scaled onto a reference trajectory or assisted by the kinematic of the other limb as for the virtual mirror therapy described in Chapter 4. Another possibility to improve estimation performances is to exploit the incrementality of the RR-RFF method in order to update the model in with new samples for the most deficient movement directions.

These analyses allowed to identify the optimal parameters to reconstruct hand position from upper limb EMG signals during reaching movements. The next step is to test the procedures

in an online scenario on healthy subjects, using a modified version of the VVITA software to validate the method and to estimate the usability and reliability of the system. The estimated position will be used directly to perform first unimanual and then bimanual reaching. As planned, if the reconstruction will not be reliable enough to be used online to accomplish the task, the reconstructed signal will be amplified and/or projected into a pre-recorded reference trajectory to give VR feedback. Moreover, as real time forward dynamic, the mass spring damper system with an additional gravitational component described in 5.2.1.2 could be used. Finally, if the system will provide a reliable target and position dependent kinematic estimation, an interpolation process (Sharif Razavian, 2017) could be applied to all the target specific maps H_P to find a unique mapping H between EMG and acceleration. Incrementality of the RR-RFF method, which was not investigated in this project, will also be taken into account to maintain a stable level of performance (Gijsberts et al., 2014).

6. Development and validation of a low-cost system for measuring maximum bite force

Based on:

De Pasquale, P., Rubino, E., Borzelli, D., Peditto, M., Nastro Siniscalchi, E., De Ponte, F. S., Oteri, G., & d'Avella, A. (2022). A Low-Cost Wireless Bite Force Measurement Device. Materials (Basel, Switzerland), 15(11), 4000. https://doi.org/10.3390/ma15114000

6.1. Introduction

Maximum bite force (MBF) is an indicator of the functional state of the masticatory system (Bakke, 2006). Individual MBF has been used to evaluate jaw muscle functionality and activity and the therapeutic effect of prosthetic devices (Calderon et al., 2006); it is considered important in the diagnosis of the disturbances of the stomatognathic system. For example, MBF in patients with symptoms of temporomandibular disorders (TMD) is lower than in healthy subjects (Molin, 1972). However, MBF may vary substantially across healthy subjects because it depends on several anatomical and physiological factors: gender, age, general physical structure (height and weight), cranio-facial morphology, pain, and occlusal factors (Fernandes et al., 2003). MBF estimation is also affected by the mechanical characteristics and measurement technique of the recording device (Koc et al., 2010). Indeed, a large variability has been found when recording MBF with different devices (Tortopidis et al., 1998) and in the sensitivity, i.e., the slope of the load-response curve, of different sensors (Testa et al., 2016).

Moreover, due to the oral cavity morphology, the biomechanical characteristics of the mouth are not homogeneous, and the position of the force transducer relative to the dental arch also affects MBF, as the more anteriorly MBF is recorded, the smaller is the maximum force achieved. Indeed, from the literature, it is well known that MBF varies in different regions of the oral cavity (Ferrario et al., 2004), with different anterior vertical jaw openings (Manns et al., 1979), and that bilateral clenching is larger than unilateral (Van Der Bilt et al., 2008). As a result of the effects of all these parameters, MBF values reported for the molar

region of healthy young adults may vary in a wide range across studies: 113-1692 N (Waltimo & Könönen, 1993), 446-1221 N (Koc et al., 2010), 216-740 N (Singh et al., 2011), with lower values reported for the incisal region: 108-293 N (Hellsing, 1980; Linderholm & Wennström, 1970; Singh et al., 2011; Waltimo & Könönen, 1993). A previous study stated that when masseter muscle activity levels were kept constant, MBF varied with bite opening, and the maximum MBF was recorded with an anterior vertical jaw opening between 15 and 20 mm (Manns et al., 1979). There has also been disagreement about MBF differences between men and women. In some studies, no difference between genders was detected, whereas, in other studies, men produced greater bite forces than women (Bakke et al., 1990; Garner & Kotwal, 1973; Helkimo et al., 1975; Singh et al., 2011; Waltimo & Könönen, 1993).

Several technologies and techniques have been used to record MBF. At present, most of the devices use strain-gauge, piezoresistive, piezoelectric, and pressure-sensitive force transducers. Strain-gauge transducer devices, consisting of a metal plate or fork whose deformation leads to resistance changes, have been proven to be highly sensitive, accurate, and capable of operating with a large measuring range. However, it is still difficult to record a true MBF due to discomfort and the fear of breaking the edges of the teeth when biting the hard surface of the transducer (Van Eijden, 1990; van Steenberghe & de Vries, 1978; Verma et al., 2017). Moreover, for the maximal incisal region force recording, "pain in teeth" might be the major limiting factor for expressing MBF (Waltimo & Könönen, 1993), and since the surface of the recording devices is usually made with hard materials, an uncomfortable and hazardous feeling may be perceived by many subjects (Fernandes et al., 2003). Placement of the sensor relative to the force application point may also affect measured MBF due to the mechanical leverage caused by the metal plate of the bite fork used in the strain gauge transducer (Braun et al., 1996; Gu et al., 2021). Piezoresistive transducer devices, consisting of a crystal silicone material that changes resistivity with the applied force, have been proven to be highly sensitive, thin, light-weight, and cheap but less accurate than strain gauge devices (Gu et al., 2021). Piezoelectric transducers use the piezoelectric effect of a material to convert the pressure into an electric signal. These devices are generally very thin

(0.1 mm) and can be used to record MBF in subjects with minimal jaw opening, but they are limited by a narrow range and low sensitivity and flexibility of the sensor (Gu et al., 2021). Pressure-sensitive devices consist of a chamber filled with fluid or air and a pressure gauge, which measures chamber pressure. Since the bite element is soft, the advantage of using these devices is that MBF can be recorded safely and comfortably; however, they are less reliable with respect to the other device types (Gu et al., 2021). Pressure-sensitive film devices consist of a pressure-sensitive sheet, which changes color according to the applied pressure. Due to their thinness, these devices do not interfere with the occlusion; however, they cannot perform continuous measurements, and they need analytical equipment to analyze the data (Gu et al., 2021).

One critical open issue concerning MBF recording is that despite several devices and techniques that have been developed, a standardized measurement method that is also easy to use and reliable is still lacking (Dýraçoðlu et al., 2008). Most of the developed devices can record force levels in the range of 50–800 N with an accuracy level of 10 N (Fernandes et al., 2003; Manns et al., 1979; Verma et al., 2017). Moreover, because of the inherent variability in placing the sensor in the patient's mouth, highly repeatable measurements of individual bite force are challenging (D. Flanagan et al., 2012), especially in the premolar or molar region (Testa et al., 2016). Another important aspect of MBF measurement devices is their cost and complexity. For example, servo-controlled motors or load cells mounted on a customized dental device have been used to investigate motor function and evaluate bite force. However, due to the complexity and costly technical procedure, these approaches are more suited for research purposes than for routine clinical examination (Testa et al., 2016).

Three-dimensional printing or additive manufacturing is a process for making 3D objects from a 3D model. The technology consists of an additive process in which successive layers of material are laid down under computer control. Nowadays, thanks to the development of affordable 3D printing technologies, rapid prototyping using 3D printers has become widespread and has a wide range of applications in several fields, such as research engineering and the medical industry. An important advantage of 3D printing is the ease of manufacturing any object of any shape with the same characteristic in any part of the world

from a 3D model as the stereolithographic STL file format, which is the standard format currently used for 3D printing (Gokhare & Raut, 2017).

The aim of the present study was to develop a novel device for the estimation of the maximum bite force that could be built in-house at a low cost and would allow recording multiple standardized incisal maximum bite forces with adequate reliability and repeatability. A comparative analysis of several force sensors, estimation techniques, and maximum expression influential factors led to the selection of the most suitable force transducer for high range reliable measurement, the design of a sensor interface allowing to express MBF in the most physiological jaw separation, and the development of methods allowing the standardization and repeatability of the measurements across multiple experimental sessions and subjects, taking into account subject's morphology. Safe operation characteristics, cost effectiveness, ease of use, and the possibility to build it in-house make the device a useful tool for investigating the masticatory system functionality of adults in a clinical and non-clinical setting for diagnosis and/or monitoring of the therapy of patients with muscular and/or orthopaedic TMD and also in affordable telemedicine scenarios. The open-source software and CAD designs are made freely available to enable easy replication of the device.

6.2. Materials and Methods

A bite force measurement device consisting of a force sensor, placed in between two 3D printed ergonomic forks and connected to a read-out system interfaced through a wireless link to a personal computer was developed (PC) (Fig. 1). A reusable silicone mold, customized for each participant, provides the interface between the forks and the subject's teeth. Thanks to the mold interface and to an offline procedure, it is possible to estimate the device placement within the oral cavity and the distance of the force transducer from force application points. A model was developed to describe the physical interactions between the masticatory system and the device. A calibration procedure was implemented, and three sets of data were collected with both the device and an accurate industrial force transducer as reference. A linear regression analysis was performed on the first dataset to calibrate the device. The reliability of calibration parameters was then assessed using the other two datasets. A validation procedure with multiple recordings was performed on 16 healthy participants. Precision over multiple sessions and repetitions across experimental conditions was analyzed using linear mixed models (LMM). For each participant, the coefficient of variation of the recorded MBF values recorded during all the repetitions within the three sessions was used as an indicator of individual variability.

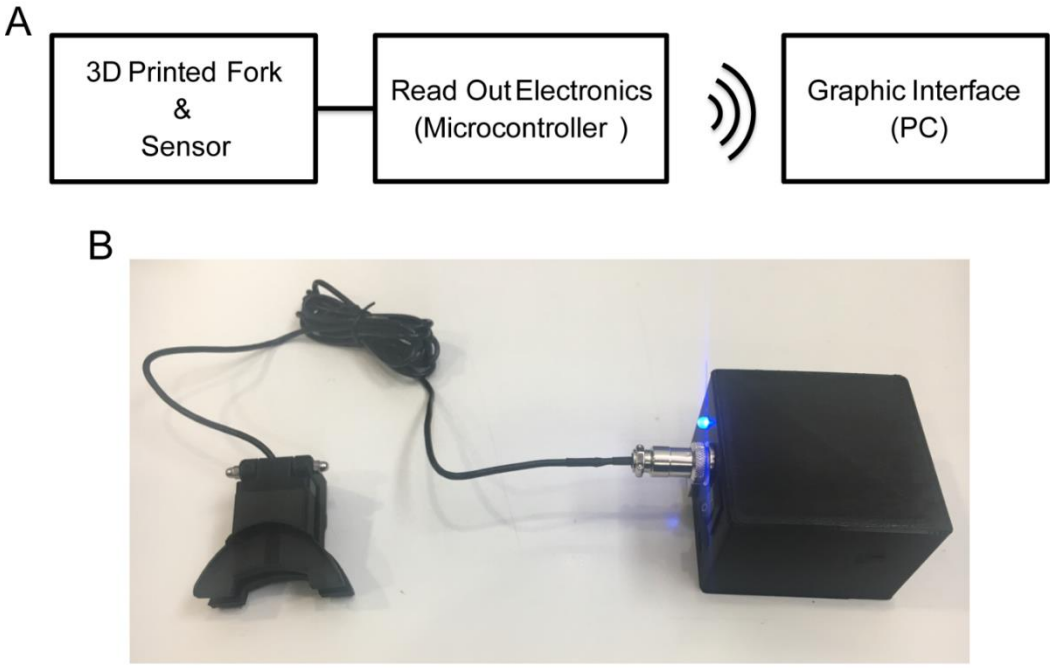

Figure 1. Bite force measurement device. (**A**) Schematic representation of the system: the force sensor placed in a 3D printed forks interface is wired connected to the electronic instrumentation, which is wirelessly connected to the PC. (**B**) Developed device: the force sensor with the 3D printed interface connected to the electronic instrumentation (box).

6.2.1. Force Sensor

A small (20 × 11 mm) and inexpensive alloy steel load cell (TAS606, Ht Sensor Technology Co., Ltd., Xi'an, China) capable of measuring up to 2000 N was used to measure bite force. The load cell transducer has four strain gauges connected in a Wheatstone bridge formation, allowing to measure changes in resistance with an accuracy of 0.3% of the full scale.

6.2.2. Custom Made Ergonomic Design and In-House 3D Printing

A custom-made ergonomic interface between the sensor and the participant's teeth was designed with commercial CAD software (AutoCAD, Autodesk Inc., San Rafael, CA, USA) and printed with a 3D printer (Supplementary Materials CAD drawing and stereolithography meshes S1). The interface consists of two hinged elements with a slot for inserting the load cell (Fig. 2). Each element (maximum length 53.8 mm) had the shape and size of a medium bite fork for dental records. At a distance of 31.8 mm from the hinge axis (fulcrum) is the center of a circular slot for the insertion of the force sensor. At the edges of each fork plate, a series of vertical flanges have been 3D printed to contain the silicone mold and to guide its repositioning. A series of notches placed at 1 mm steps, starting from the center of the force sensor, indicated with a cross notch, were printed on each fork plate. When the mold is placed on the fork plate and pressure is exerted, these notches leave an indentation on the mold. An offline procedure then allows measuring the distance between the center of the sensor (cross notch) and the incisal teeth by comparing the position impressed on the mold of the incisal teeth with respect to the indentations generated by the notches. The total vertical distance between the force application points (on the upper surface of the top element and on the lower surface of the bottom element) was 15.0 mm with the force sensor inserted between the two elements. A commercial 3D printing machine (Ultimaker 2 Extended+, Ultimaker B.V., Geldermalsen, The Netherlands) was used for prototyping the device. Polylactic Acid (PLA) was chosen as the printing material because it is biodegradable and non-toxic when used in solid form. A nozzle of 0.4 mm was used to lay down, at a speed of 50 mm/s, a layer of material with a grid infill pattern and a density of 20%. Stereolithography meshes used for 3D printing can be found in the Supplementary Materials CAD drawing and stereolithography meshes S1.

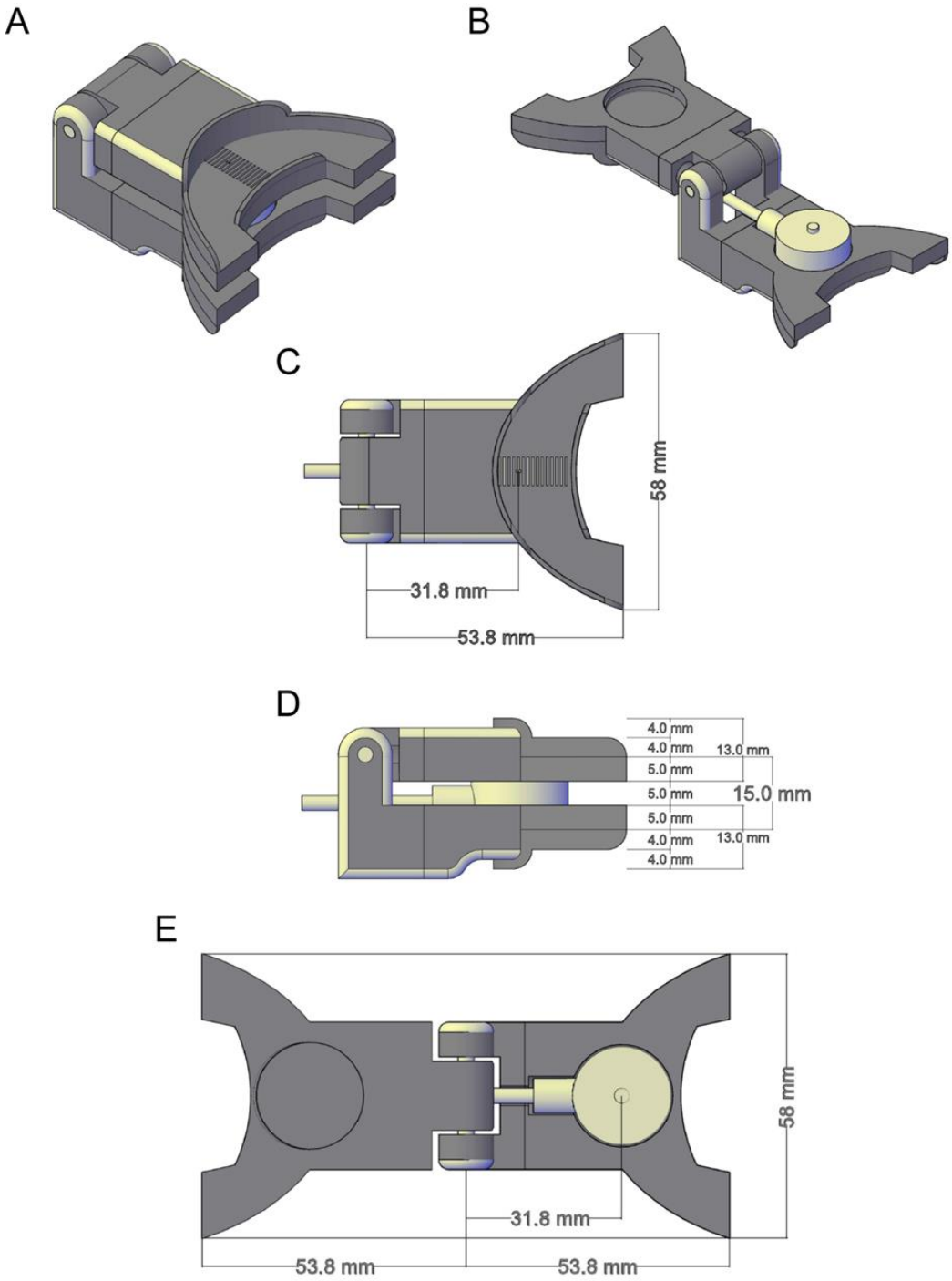

Figure 2. Interface of 3D CAD model. Representation of the 3D printed interface and the force measurement sensor CAD models. (**A**, **B**) Isometric view of the 3D sensor placed in the interface CAD while the upper fork plate is closed (**A**) and open (**B**). (**C**, **D**) The top-bottom and medio-lateral views of the sensor-interface CAD with the relative sizes, respectively. (**E**) Top-bottom view of the sensor while the upper fork plate is open.

6.2.3. Read-Out System

The data read-out system consisted of a microcontroller (Arduino UNO, Arduino S.r.l.) connected to the load cell through an amplifier (HX711, AVIA Semiconductor), powered by a 3.7 V lithium-ion battery with 2000 mAh capacity. A Bluetooth module (HC-05, iTeadStudio) is used to establish a wireless link to transmit data from the microcontroller to a PC and to control the device from the PC. Read-out components are mounted in a custom-made 3D printed housing. The read-out components and circuitry scheme can be found in Supplementary Figure S1, and the 3D CAD model and the stereolithography meshes used for 3D printing the housing can be found in Supplementary Materials CAD drawing and stereolithography meshes S1.

6.2.4. Software

Software modules for data collection, device control, and data display were developed using two different open-source solutions. The software running on the Arduino microcontroller collects data from the force measurement sensor and transmits it via Bluetooth to the PC, which is implemented using Arduino scripting language. The graphical user interface controlling data collection and display on the PC (Fig. 3) was developed in C#. Arduino sketches and the PC GUI C# Visual Studio project can be found in Supplementary Materials Software S1.

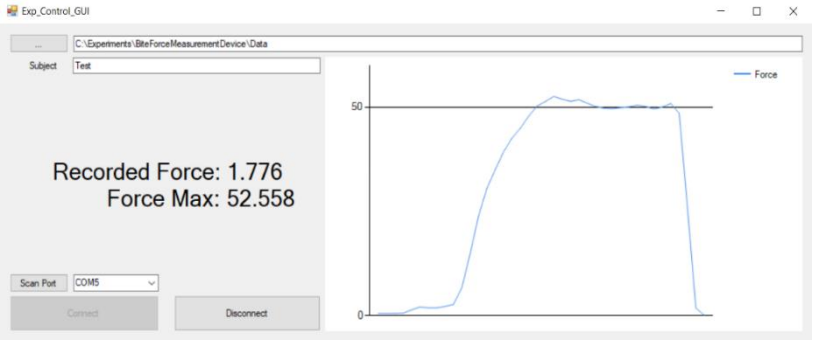

Figure 3. Data visualization software interface. C# based interface running on a PC allows visualizing and saving data sent wirelessly from the Arduino board. The software interface displays the instantaneous expressed force (Kg) and MBF achieved during the whole session.

6.2.5. Physical Model

Since the position of the measuring sensor with respect to the dental arch is necessary to measure MBF, the point of force application by the dental arches on the fork plates must be estimated. A model (Fig. 4), consisting of a simplified representation of both the masticatory system (blue) and the device (red), allowed us to characterize the mechanical interaction between the fork plates and the dental arches and to determine that the force application point occurs at the level of the incisors. In particular, the force recorded by the force sensor on the device is proportional to the force exerted by the incisors furthest away from the force sensor.

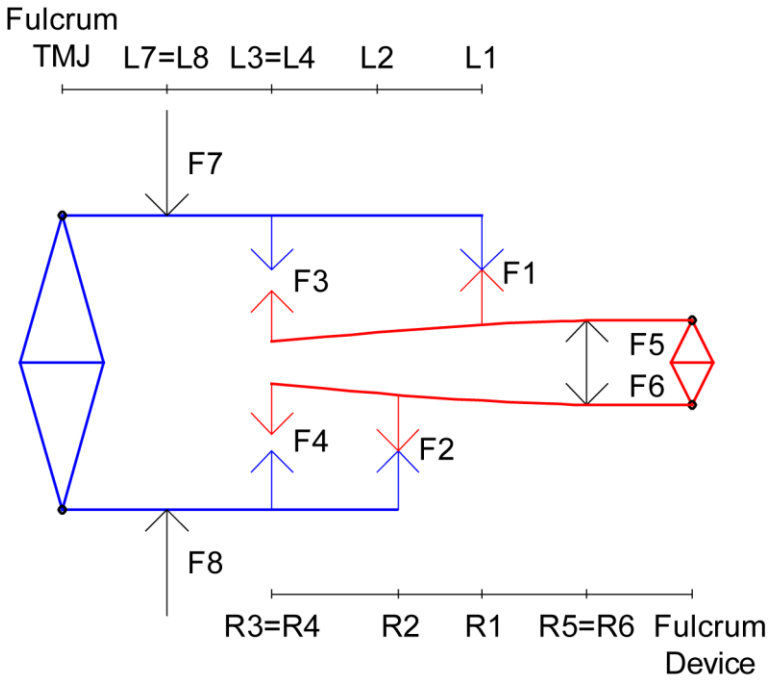

Figure 4. Schematic representation of masticatory system (blue) and device (red) model system. F7 and F8 are equal and opposite forces exerted by the masticatory muscles; F5 and F6 are forces recorded by the sensor. For simplicity, only two contact points between the mouth and the device are considered for each arc: F1 and F3 for the upper part, F2 and F4 for the lower one.

The device is modeled as a second-order lever with the load (force transducer) between the fulcrum and the effort (bite force). The masticatory system can be described as a third-class lever with the effort (masticatory muscles force) between the fulcrum (condyle) and the load (teeth-device application points). The force recorded on the transducer is proportional to the force applied by the masticatory muscles. In particular, since the device acts as a lever, the applied force can be estimated from torque balance and depends on the difference between the distance from the sensor to the fulcrum and the distance from the force application point to the fulcrum, which are the lever arms. Moreover, since the device is a second-order lever, the difference between lever arms will provide a mechanical advantage (gain) in the recorded force with respect to the real one. When the mouth is open, the forces applied by the masticatory muscles (Fig. 4, F7, and F8, equal and opposite forces) rotate the

jaws around the fulcrum. For simplicity, only two contact points between each dental arch and each element of the device are considered: F1 and F3 for the top element, F2 and F4 for the bottom element. However, the method can be generalized to an arbitrary number of contact points without affecting the result. The problem can be considered as a statically indeterminate problem in which the laws of static are not sufficient to determinate all the unknown forces or moments (Crandall et al., 1972). This problem can be solved by writing the appropriate equations of static equilibrium and additional equations pertaining to the deformation and constraints known as compatibility conditions (see Appendix A). From the characterization of the device, if the distance R1 between the application point of F1 and the fulcrum of the device is greater than the distance R2 for F2, then the sensor momentum (Ms = Fs·Rs) is equal to the momentum at the upper incisal teeth (M1 = F1·R1) because the top element of the device works as a hyperstatic beam and the force F3 is equal to zero. Conversely, if R1 is smaller than R2, then Ms is proportional to the momentum at the upper lower incisal teeth (M2 = F2·R2), and F4 is equal to zero, see Equation (1). Therefore, the force recorded by the sensor depends on the distance between the sensor and the most distant incisal application point.

$$\begin{cases} F1 = \dfrac{Fs \cdot Rs}{R1}, & if\ R1 > R2 \\ F2 = \dfrac{Fs \cdot Rs}{R2}, & if\ R1 < R2 \end{cases} \quad (1)$$

6.2.6. Calibration Procedure Using a Second Force Transducer

To calibrate the device, it was loaded with known forces through a manual press. To measure the forces applied by the press, two accurate 6-axis force transducers were used: a small 6-axis transducer (Nano 25 F/T Sensor, ATI Industrial Automation, Apex, NC, USA, Fig. 5A) calibrated by the manufacturer, with a resolution of 1/16 N and a maximum force of 500 N (single-axis overload: ± 7300 N) for the longitudinal axes and a large 6-axis transducer (Delta F/T Sensor, ATI Industrial Automation, Apex, NC, USA, Fig. 5B), with a resolution of 1/16 N and a longitudinal maximum force of 495 N (single-axis overload: ± 10,000 N) for the longitudinal axis. Forces were applied on the two elements of the device

through a 3D-printed PLA interface (base 0.2 × 2 mm) mounted on the 6-axis force transducer so that both devices were firmly coupled with the manual press machine (Fig. 5A, B). The system, 1D-6D load cell (Fig. 5C), can be characterized by the linear equation derived from the system of torque balance equations (Halliday et al., 2013):

$$F_{1D}d_{1D} = F_{6D}d_{6D}$$

where F6D is the force measured by the 6-axis sensor, F1D is the force measured by the device 1-axis sensor, d1D = Lever is the lever arm, i.e., the distance from the center 1-axis sensor to fulcrum; d6D = Lever + Δd is the distance from the center of 6-axis sensor to the fulcrum:

$$F_{6D} = \frac{F_{1D}Lever}{Lever + \Delta d} = F_{6D} + \frac{F_{6D}\Delta d}{Lever}$$

If F_{6D} = x and F_{1D} = y,

$$y = x + \frac{x\Delta d}{Lever} = x(1 + \frac{\Delta d}{Lever}) \quad (4)$$

$$\hat{y} = Offset + x\ Slope + x\ Slope\frac{\Delta d}{Lever} \quad (5)$$

$$\hat{y} = \beta_1 + x\ \beta_2 + x\ \beta_3\Delta d \quad (6)$$

where β1 = Offset, β2 = Slope, β3 = Slope/Lever. Then:

$$\hat{x} = \frac{y - \beta_1}{\beta_2 + \beta_3\Delta d} = \frac{y - Offset}{Slope + Slope\frac{\Delta d}{Lever}} \quad (7)$$

$$\widehat{F_{6D}} = \frac{F_{1D} - \beta_1}{\beta_2 + \beta_3\Delta d} = \frac{(F_{1D} - Offset)}{Slope + Slope\frac{\Delta d}{Lever}} \quad (8)$$

The parameters β_1, β_2, and β_3 (Equation (6)) were estimated with a linear regression performed on the dataset. In the first dataset with the small transducer, 21 different force values, ranging from 0 to 490 N (0–50 Kg), were recorded. Each measurement consisted of

50 samples. Then, 2 additional datasets were recorded to test the reliability of the estimated parameters. The first test dataset consisted of 15 force recordings, with a load range from 98 to 490 N with a step size of 100 N and different force application points at 0, 5, and 10 mm from the 1D load cell axis, in order to characterize the lever gain. The second dataset collected with the large transducer consisted of 6 recordings (50 samples each), from 0 to 980 N.

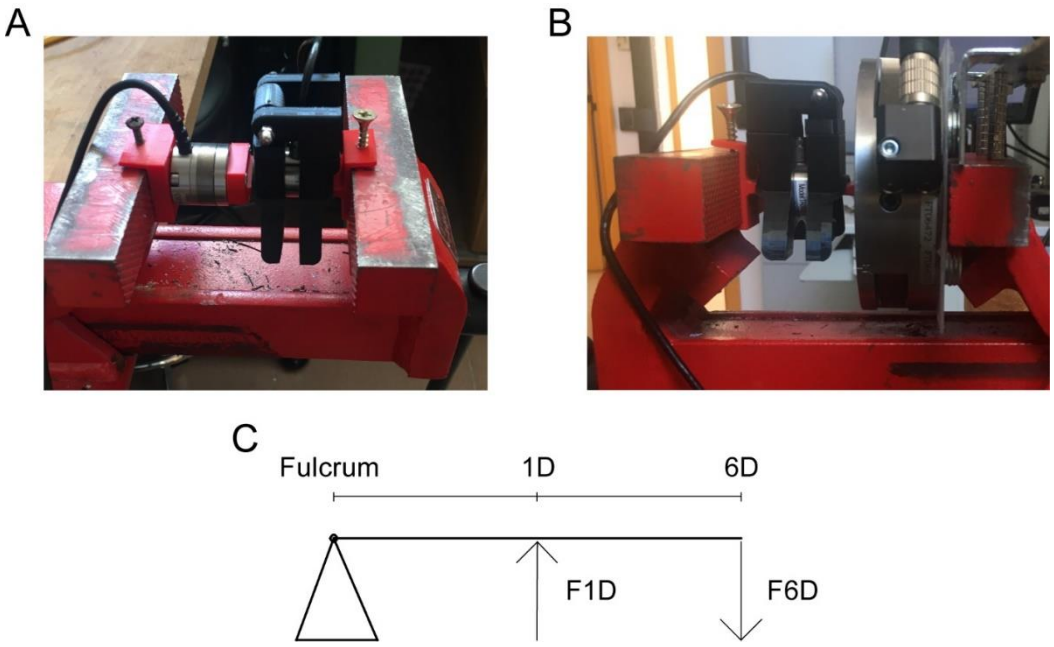

Figure 5. Calibration procedure. A manual press machine applies several loads on the device through a second calibrated load cell. (**A**) The calibration procedure used a small 6D force transducer (max force 500 N) as the second device. (**B**) the setup with a large 6D force transducer (max force 495 N). (**C**) Schematic representation of the second-order lever, which characterizes the calibration process. In particular, the press machine exerts a force on the 6 DOF (*F6D*) sensor, which can be placed at a variable distance ($\Delta d = d_{6D} - d_{1D}$) from the main axes of the 1 DOF. d_{6D} and d_{1D} are, respectively, the distances from the fulcrum of the lever of the 6 DOF and 1 DOF sensors. *F1D* is the resulting force recorded on the 1 DOF sensor.

6.2.7. Validation Procedure with Multiple Force Recordings of Healthy Participants

Sixteen healthy participants (7 females), aged from 24 to 55 years (32 ± 10, mean ± SD), height 155 to 187 cm (170 ± 10 mean ± SD), weight 52 to 87 kg (68 ± 11 mean ± SD), performed 3 consecutive MBF measurement sessions for 3 days. Subjects were tested at the U.O.C. Odontoiatria ed Odontostomatologia of the Azienda Ospedaliera Universitaria (AOU) Gaetano Marino in Messina, were informed of the purposes of the measurement and gave their consent to the measurement and to the collection of personal data. The study was conducted in accordance with the Declaration of Helsinki, and since the measurements did not involve any intervention, they did not require ethical approval according to the standard procedures of the AOU. Subjects were seated on a chair with heads positioned so that the Frankfort horizontal plane would be parallel to the floor while performing the task. When the subject performed the task for the first time, the forks were filled with silicone teeth mold and covered by a plastic thin film that sealed the device from liquids (Fig. 6A). The operator placed the device in the mouth of the participant simulating the teeth moulding procedure in order to obtain a subject-specific interface (Fig. 6B, C). Thanks to the fork supports, the silicone mold can be easily removed from the fork and replaced in the same position for multiday recordings. The silicone mold provides a measure of the incisive teeth application point, which can be used offline in order to estimate the correct MBF value (Fig. 6C).

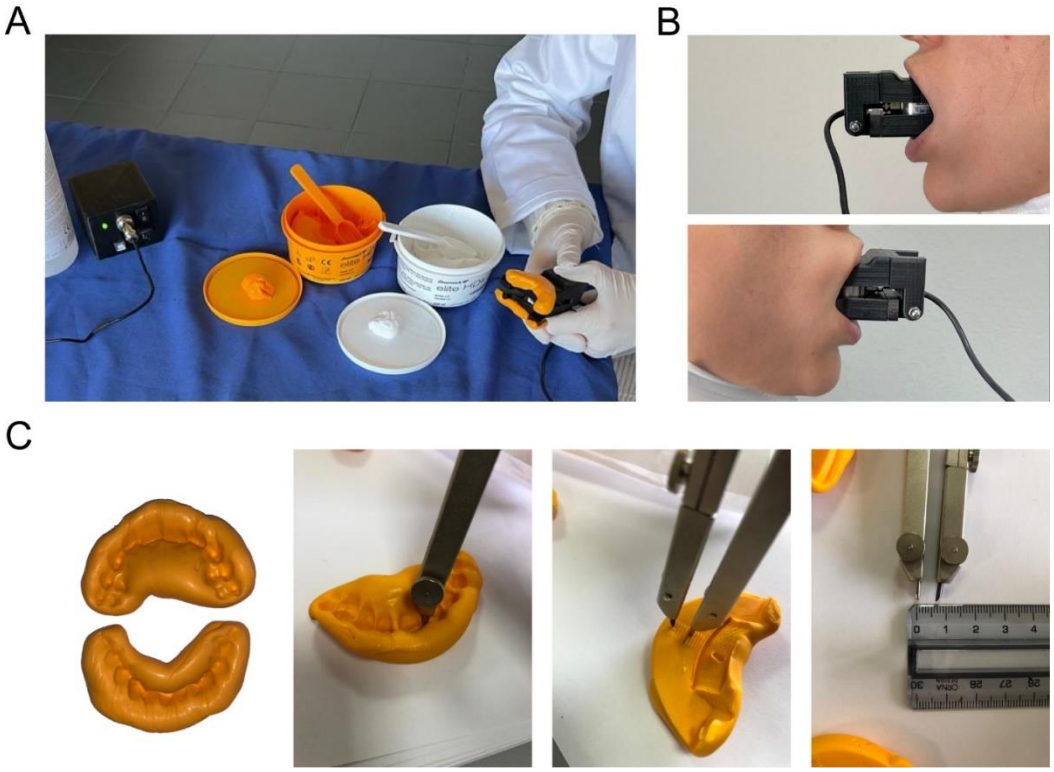

Figure 6. Experimental procedure. (**A**) Device setup steps. During setup phase, therapist places the teeth silicone molds on the device forks. (**B**) Device placed in subject's mouth. (**C**) Example of the subject's customized upper and lower silicone molds and the application point distance measurement phase. During this phase, the distances between both incisors, upper and lower, and the center of the sensor are estimated thanks to the notches on the silicone mold.

6.2.8. Statistical Analysis

The dependence of MBF on experimental factors was analysed with a linear mixed model (LMM) that accounts for interindividual variability by including the participant as a random effect. The session (S) and the repetition (R) within each session were treated as fixed effect factors. Data were fitted with the model described in Equation (9).

$$Y = u_0 + \alpha_0 S + \beta_0 R + \epsilon$$

In Equation (9), u_0 represents the individual intercept and accounts for inter-individual differences. The coefficients α_0 and β_0 represent fixed-effects; thus, the modulation of the response variable by the main factors *S* and *R*. The estimation of model parameters was based on the maximum likelihood approximation. To test the significance of each fixed effect term in the selected model, a hypothesis test on the fixed effect terms applying analysis of variance (ANOVA) on the fitted LMM was performed. The analysis was implemented in Matlab.

6.3. Results

6.3.1. Calibration: Accuracy and Precision

In Figure 7A, the forces recorded during the calibration and testing phases are reported for three datasets. For each estimated point, which represents the mean value over 50 samples, the distance of the force application point from the center of the device (1-axis) force sensor is reported. The forces estimated with the 6-axis sensor (red) and the one recorded with the 1-axis sensor (blue) are reported for the calibration session (filled circular markers) and the test sessions (empty circular markers). The mean force estimation error of the force measured with the device (1-axis sensor) with respect to the 6-axis sensor was 0.00 ± 0.65 N for the calibration dataset and 6.4 ± 6.7 N for the test datasets. Figure 7B shows the force estimated by the device (1-axis sensor) as a function of the force estimated with the accurate 6-axis sensor, and Figure 7C the force residual, for the test sessions. The color of the triangular markers indicates the distance of the force application point from the center of the 1-axis sensor.

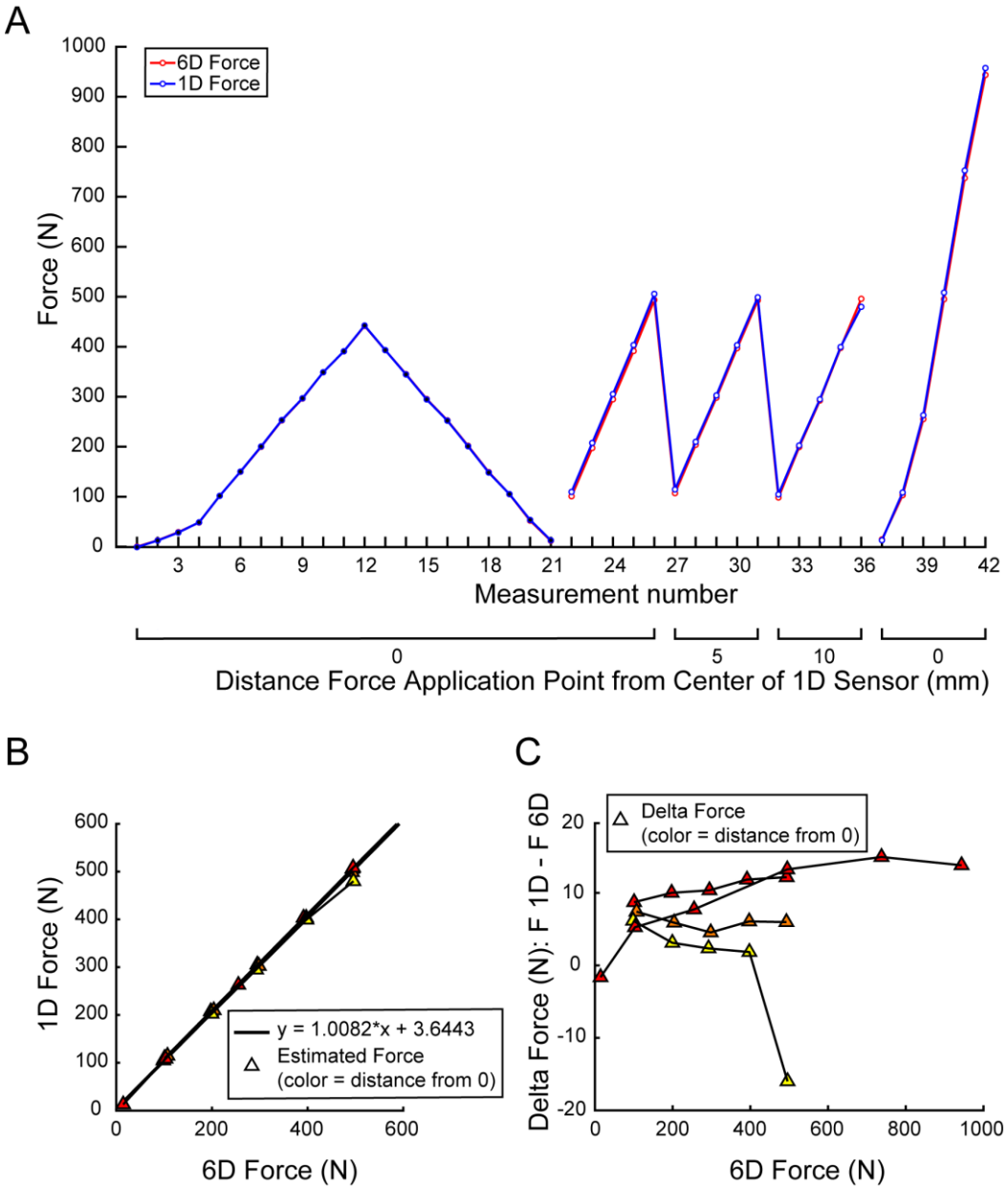

Figure 7. Calibration results. (**A**) Calibration and test session curves. Estimated force recorded with the 6D load cell (red), and the estimated force recorded with the 1D sensor (blue), are reported in the function of the application point distance from the center of the 1D load cell. Black dots are the records used for the calibration; white dots are the data used for the test. (**B**) Compares the 1D load cell estimated force with the 6D load cell one. (**C**) Delta force (1D − 6D estimated force) in function of the 6D one. Triangle color indicates the distance of the force application point from the center of the 1D sensor (yellow: 10 mm; orange: 5 mm; red: 0 mm).

6.3.2. Validation: Repeatability and Effect of Session and Participant

Figure 8A illustrates an example of the force data recorded in one participant (12). In each recording session (different colors) performed on three different days, the participant generated MBF three times in the course of about 20 s. The average MBF over all sessions for each participant varied from a minimum of 65 N to a maximum of 584 N (see Fig. 8B). Gender is indicated with different colors (blue) for male and (red) for female participants. Thus, the data revealed a large inter-individual variability of MBF. The average MBF over participants was 240 ± 105 N (mean ± SD), which is compatible with the mean incisal range found in the literature (108-293 N) [12]. The mean maximum bite force for men was (277 ± 114 N), with the range of 584 to 105 N. The mean maximum bite force for women was (195 ± 64 N), with the range of 308 to 65 N. Figure 8C shows the mean values over repetitions in each session, better highlighting the repeatability over repetitions and sessions. A linear mixed effect (LME) model, with gender, repetition, and session as fixed effects and subject as random effect, did not reveal any statistically significant differences between gender ($p = 0.25$), repetitions ($p = 0.26$), and sessions ($p = 0.24$). Figure 8D shows a broad distribution of the coefficient of variation (CV) of MBF across sessions for each participant. The average CV over participants was 11 ± 4%, indicating a low extent of variation for the recorded forces for each subject, which confirm the precision and repeatability of the measurement within and between sessions. Figure 8E shows the individual CV as a function of MBF. No significant relations between MBF and the CV were found.

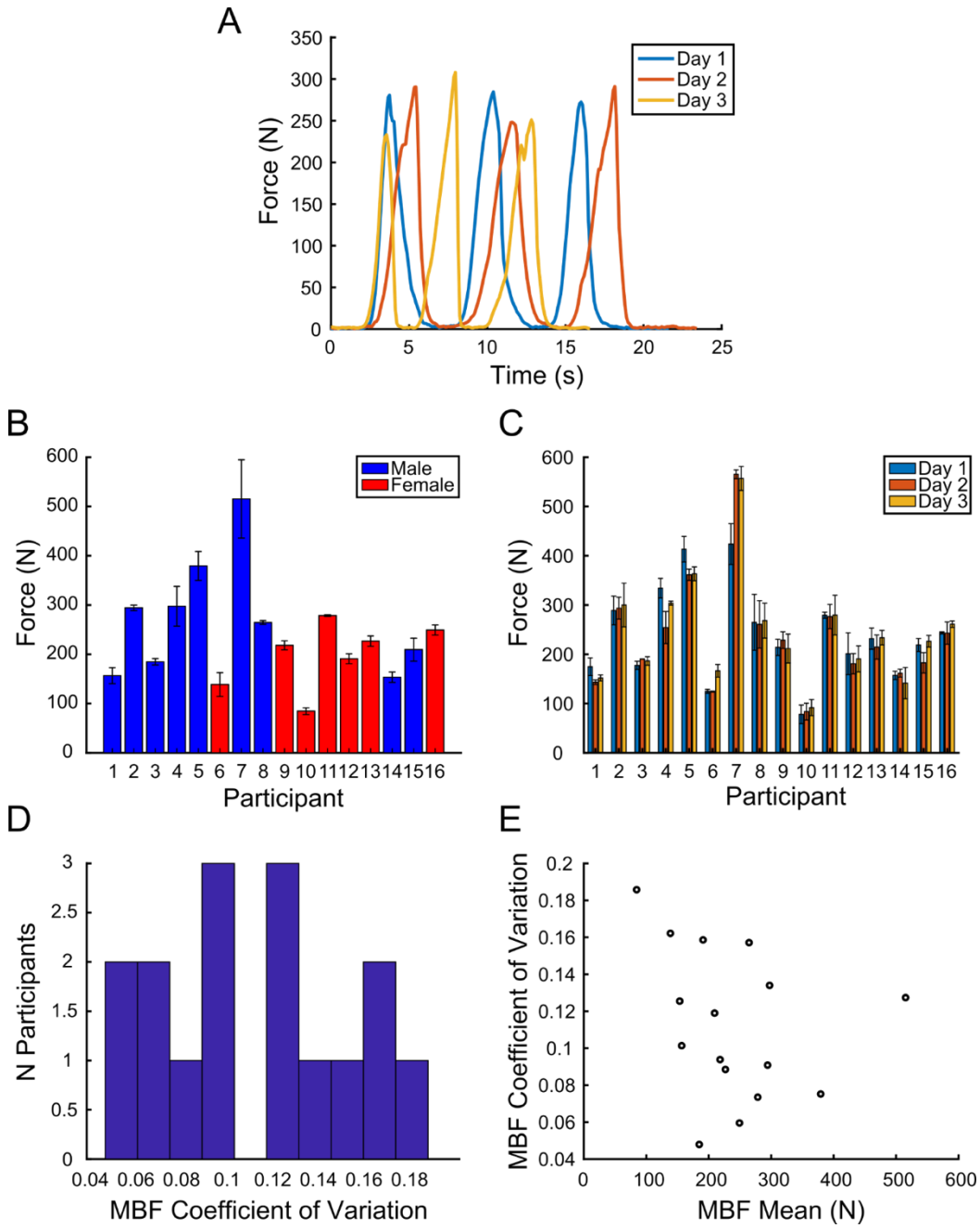

Figure 8. (**A**) Recorded MBF profiles as a function of time for the 3 different sessions (different colors). During each session, subject performed MBF 3 times. (**B**) Mean MBF value over sessions for each subject, (blue) for male and (red) for female. (**C**) Mean MBF value over session repetitions for each subject. (**D**) Histogram of MBF coefficient of variation value, (**E**) MBF coefficient of variation in function of MBF mean.

6.4. Discussion

Evaluation of MBF is important to assess the functional state of the masticatory system. Despite the various devices using different technologies that have been developed to measure MBF, there is still no standardized measurement method that is also easy to use and reliable. It is well known that the mechanical characteristics and the measurement technique of the recording device can influence the accuracy and precision of MBF estimation (Koc et al., 2010). Moreover, as MBF can be affected, in addition to the used technologies, by the presence of TMJ disorders (Molin, 1972), patient-specific anatomical factors (Fernandes et al., 2003), and force application point (Braun et al., 1996; Gu et al., 2021), device placement within the oral cavity must be standardized and evaluated to reliably estimate MBF. Finally, to obtain adequate reliability and repeatability while performing multiple measurements in the same patient, it is critical to minimize the dependence of the results from the operator and to make an accurate repositioning of the device that is easy to perform.

A novel, low-cost MBF measurement device, based on a commercially available strain gauge sensor, with a nominal working range adequate for use with adult subjects, inserted in a custom housing interface, using a simple microcontroller-based data read-out system connected wirelessly to a data acquisition and display software on a personal computer was introduced. The soft polymeric housing of the sensor can be easily reproduced, without any industrial machinery, with a commercial 3D printer and provides a homogeneous soft surface to bite, which overcomes the fear of breaking edges of the teeth that may occur when biting in the hard surface of the strain-gauge force sensor (Van Eijden, 1990; van Steenberghe & de Vries, 1978; Verma et al., 2017). The developed measurement procedure, based on the usage of a reusable subject-specific silicone mold, allows for customizing the device according to individual anatomical factors and easily repositioning the device within the mouth. A series of notches in the 3D printed forks are imprinted by pressure on the silicone mold, providing a graduated indicator that allows to easily estimate the distance between the force sensor and both the upper and lower incisive teeth region. Such estimation is

necessary to evaluate the force application point, which may vary across individuals since the distances between both teeth regions and the sensor depend on the anatomical structure. The distance between the sensor and the application point is required for a reliable estimation of MBF since the device acts as a lever due to the developed 3D printed interface design. Neglecting the distance between the device and the force application point when measuring MBF may lead to unreliable force estimation, especially for strain gauge-based devices with a metal fork acting as a lever (Braun et al., 1996; Gu et al., 2021). To reliably estimate MBF according to the participant's morphology, a model of the interaction between the masticatory system and the device was developed. Then, a test calibration was performed in the laboratory to assess the reliability and repeatability of the device within the physiological range of loads and application points. The device demonstrated satisfactory performance in terms of accuracy and precision in an adequate force range. In particular, the device could record forces in the range of 0-980 N with an accuracy of about 6.4 N and a precision of 6.7 N, corresponding to a mean relative accuracy of 2% over the test dataset and a relative precision of 2% for the mean force value of the test dataset. Previous reviews reported a mean accuracy of 2% in the range 0-350 N (Koc et al., 2010) or an accuracy of 10 N and 20% relative precision (assuming that one minus relative precision, i.e., 80%, was reported) in the range of 50–800 N (Fernandes et al., 2003; Manns et al., 1979; Verma et al., 2017). It is worth noticing that the selected force transducer allows for an even wider force range, up to about 2000 N, but the calibrated load range was adequate for incisive region MBF (Hellsing, 1980; Linderholm & Wennström, 1970; Singh et al., 2011; Waltimo & Könönen, 1993). The consistency and accuracy of the bite force recorder were further supported by testing 16 adult subjects. As shown in the results section, the reliability and validity of MBF estimations (240 ± 105 N) are in line with published studies using state of the art bite force recording devices for measuring maximum incisal teeth bite force in healthy subjects (108-293 N) (Hellsing, 1980; Linderholm & Wennström, 1970; Singh et al., 2011; Waltimo & Könönen, 1993). The values recorded were just above those reported in the literature, possibly due to physiological factors specific to the selected participants or to the more comfortable bite afforded by the developed device, which allows for exerting MBF

without fear. Differences between gender were also investigated. While in some studies, no differences between gender were detected, in most studies, men produced greater bite forces than women (Bakke et al., 1990; Garner & Kotwal, 1973; Helkimo et al., 1975; Singh et al., 2011; Waltimo & Könönen, 1993). Even if, in our study, men's mean maximum bite force (277 ± 114 N) was greater than for women (195 ± 64 N), no statistically significant differences in bite force were found (Singh et al., 2011). This might be due to the small number of subjects included in the study.

The customization of the device using a subject-specific silicone mold allows for adequate repeatability across multiple sessions. The developed methods also allow performing multiple recordings either within the same day or on different days with high precision (CV of 11 ± 4%) and no statistically significant differences within or across sessions. Because teeth shape may vary and because of the variation in positioning the sensor in the patient's mouth, which might also be due to operator inaccuracy, force estimation (Braun et al., 1996; Gu et al., 2021) may be unreliable (D. Flanagan et al., 2012; Hellsing, 1980), and highly repeatable measurements of patient MBF may be difficult to achieve (D. Flanagan et al., 2012), especially in the premolar and molar region (Testa et al., 2016). However, one study did not find statistically significant differences between repetitions (Fernandes et al., 2003), possibly because the authors were very careful in repositioning the sensor within the oral cavity. Since in our device, after the first application, the replacement within the oral cavity is standardized by the silicone mold, the device can be repositioned precisely and also used without the operator's supervision.

Finally, the design of our device has additional desirable features. To ensure the safety of the device, the electronic read-out component transmits wireless data to a PC for storage, and it is therefore intrinsically safe, as it does not require a power isolation thanks to a low voltage battery supply. Moreover, the device is low-cost, can be easily reproduced, and is able to assess MBF in clinical or domestic settings for characterizing the functionality of the masticatory system for patients with TMJ disorders during a longitudinal study or a rehabilitation program. However, the device also has some limitations. Even if the device is wireless, it requires a PC to visualize and store data. Future developments will address this

limitation by integrating a display and a data storage system directly into the small-size, portable read-out system. Another limitation is the requirement of an initial silicone mold customization procedure to standardize device replacement within the mouth, compared to a simple stick fork that can be directly bitten. However, the silicone mold has several benefits, such as the accuracy of the repositioning and the device customization with respect to the patient's mouth, that justify its use. Moreover, the material required for the mold is easily available in dentistry. Finally, to be reproduced, the device requires a 3D printer. However, nowadays, 3D printing is very affordable.

6.5. Conclusions

A novel computer-assisted design for an MBF measurement device was developed that is portable, cost effective, and open-source. The device is easy to use, reliable and can be employed in both clinical and domestic environments, for accurate functional assessments, for monitoring of the therapy of patients with muscular and/or orthopedic TMD, and in telemedicine scenarios. Further studies will use the novel device to characterize the changes in MBF and evaluate the efficacy of physical therapy in specific pathologies, such as TMD (Linsen et al., 2009) and myotonic dystrophy (Guimaraes et al., 2007). Moreover, further development will concern the integration of a low-cost EMG system to study the relation between MBF and myoelectric signals recorded from jaw-closing muscles (Manns et al., 1979).

6.6. Appendix A

6.6.1. Appendix A.1. Physical Model

In this section, the interaction between the masticatory system and the force measurement device can is described using a simple physical model. The equilibrium of momentum equations is used to characterize the device, which works as a second-order lever. Static methods have been applied to solve the problem, which shows an indeterminate solution. Through this model, the device can record the force applied at the most distant incisive teeth from the sensor, and thus the correct MBF estimation requires taking into account the participant's dental arc morphology.

Figure A1 shows a simplified model of the masticatory system and the device. In this system, the masticatory system in blue and the force recording device in red are represented. The masticatory system can be described as a third-class lever with the effort (masticatory muscles force) between the fulcrum (condyle) and the load (teeth-device application points). Our device is modeled as a second-order lever with the load (force transducer) between the fulcrum and the effort (bite force).

In particular, equal and opposite *F7* and *F8* represent the force exerted by the masticatory muscles system, *F5* and *F6*, instead of the force measured by the sensor. For simplicity, only two points of contact between the mouth and the device are considered for each arch: *F1* and *F3* for the upper part, *F2* and *F4* for the lower one. Table A1 reports the momentum equilibrium equations for both the device and the masticatory system. The method can be generalized to an arbitrary number of contact points.

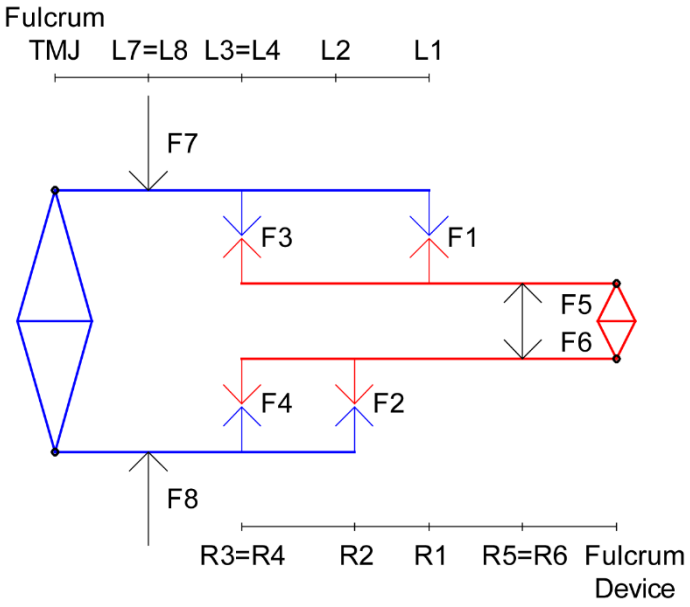

Figure A1. Schematic representation of masticatory system (blue) and device (red) model system. F7 and F8 are equal and opposite forces exerted by the masseter, F5 and F6 force recorded by the sensor. For simplicity, only two points of contact between the mouth and the device are considered for each arch: F1 and F3 for the upper part, F2 and F4 for the lower one.

Momentum Equilibrium Equations	
Device	**Masticatory System**
$\Sigma M = 0$	$\Sigma M = 0$
$(1)\ M5 = M1 + M3$	$(1)\ M7 = M1 + M3$
$(2)\ M6 = M2 + M4$	$(2)\ M8 = M2 + M4$
$(3)\ M5 = M6$	$(3)\ M7 = M8$
$M1 = R1 \cdot F1$	$M1 = L1 \cdot F1$
$M2 = R2 \cdot F2$	$M2 = L2 \cdot F2$
$M3 = R3 \cdot F3$	$M3 = L3 \cdot F3$
$M4 = R4 \cdot F4$	$M4 = L4 \cdot F4$
$M5 = R5 \cdot F5$	$M7 = L7 \cdot F7$
$M6 = R6 \cdot F6$	$M8 = L8 \cdot F8$
$F1 \cdot R1 + F3 \cdot R3 = F2 \cdot R2 + F4 \cdot R4$	$F1 \cdot L1 + F3 \cdot L3 = F2 \cdot L2 + F4 \cdot L4$

Table A1. Momentum equilibrium equations for the device (left column) and the masticatory system (right column).

If only the upper arches of the device and the masticatory system are considered (Fig. A2), the model would be composed of two beams hinged at one end and resting on two supports (device-dental arc contact points). The force in both cases is applied between the hinge and the two supports, which will generate constraint reactions.

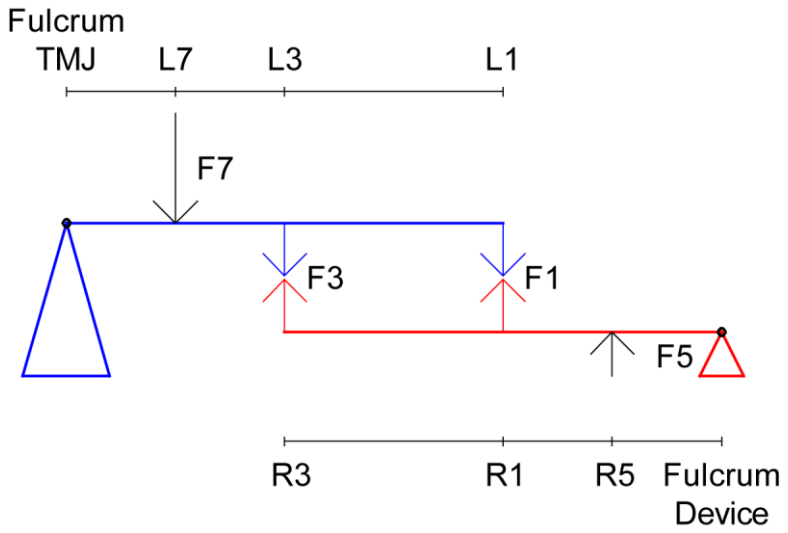

Figure A2. Schematic representation of upper component of the masticatory system (blue) and device (red) model system.

Each beam is considered separately, and since the number of unknown constraints is higher than the available equations, the problem is statically indeterminate (or hyperstatic) (Equation (A1)). However, while isostatic structures can be treated as rigid bodies, hyperstatic structures must be treated as deformable bodies to solve all the constraints. Therefore, both the masticatory system and the device as a hyperstatic beam whose load (representing the action exerted by the masticatory muscles) is applied between the fulcrum and the loads (device-teeth contact points) are considered (Fig. A3). Hyperstatic structures require compatibility conditions and solid body deformation equations to be considered in addition to the static equilibrium equations for determining the internal forces and reactions. Therefore, the superposition effect principle (Crandall et al., 1978) to the

deformations of the redundant constraint, which is assumed to be the support in *L1*, was applied. The principle of superposition states that on a linear elastic structure, the combined effect of several loads acting simultaneously is equal to the algebraic sum of the effects of each load acting individually (Equation (A1)).

$$\begin{cases} \Sigma VerticalForces = V0 + V1 + V2 \\ \Sigma Ma = F \cdot L = V1 \cdot L1 + V2 \cdot L2 \end{cases} \quad \text{(A1)}$$

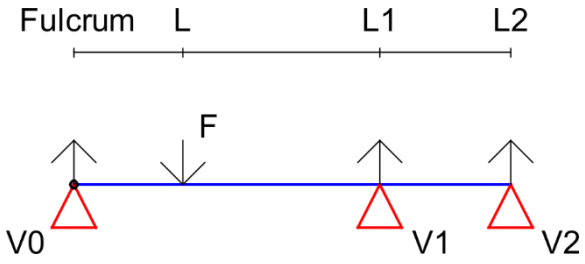

Figure A3. Hyperstatic beam representation.

6.6.2. Appendix A.2. Principle of Superposition

1. Removing the constraint *L1*

If the constrain *L1* is removed, a supported beam with a concentrated load is obtained (Fig. A4). For the resolution, it is necessary to consider the differential equation of the elastic line (Crandall et al., 1978).

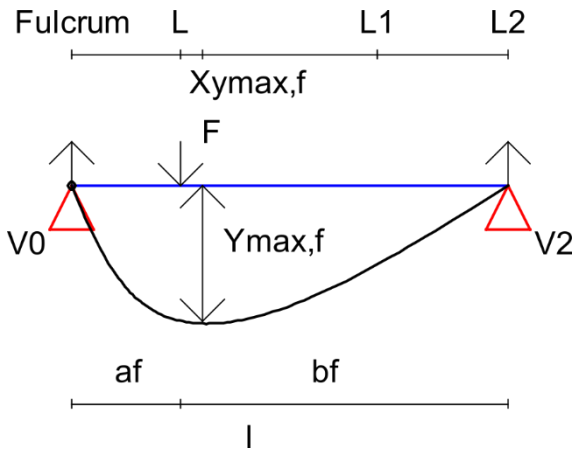

Figure A4. Representation of the hyperstatic beam without the constrain *L1*.

If *af* > *bf*,

$$X_{Ymax,f} = \frac{\sqrt{l^2 - bf^2}}{\sqrt{3}}$$

$$Y_{max,f} = \frac{F \cdot bf \cdot \sqrt{(l^2 - bf^2)^3}}{9 \cdot \sqrt{3} \cdot E \cdot J \cdot l}$$

where *E* is the Young's modulus and *J* is the second moment of area.

If *af* < *bf*, x-axes must be inverted:

$$\begin{cases} af' = bf \\ bf' = af \end{cases}$$

$X_{Ymax,f'} = \frac{\sqrt{l^2 - bf'^2}}{\sqrt{3}}$ for inverted x-axes,

$X_{Ymax,f} = l - X_{Ymax,f'}$ for original x-axes,

$$Y_{max,f'} = \frac{F \cdot bf' \cdot \sqrt{(l^2 - bf'^2)^3}}{9 \cdot \sqrt{3} \cdot E \cdot J \cdot l}$$

2. Removing the force F

In this case, a supported beam with concentrated load is obtained (Fig. A5).

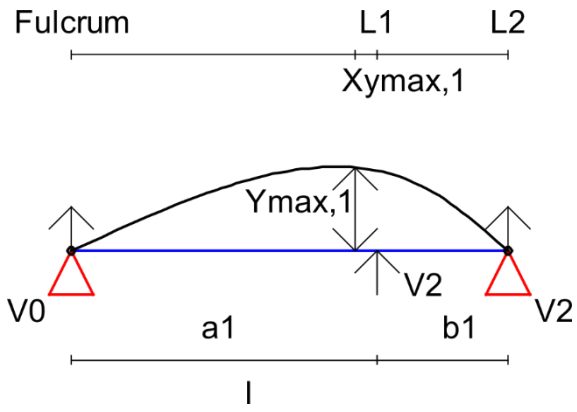

Figure A5. Representation of the hyperstatic beam without the force F.

If $a1 > b1$,

$$X_{Ymax,1} = \frac{\sqrt{l^2 - b1^2}}{\sqrt{3}}$$

$$Y_{max,1} = \frac{V1 \cdot b1 \cdot \sqrt{(l^2 - b1^2)^3}}{9 \cdot \sqrt{3} \cdot E \cdot J \cdot l}$$

If $a1 < b1$, x-axes must be inverted:

$$\begin{cases} a1' = b1 \\ b1' = a1 \end{cases}$$

$X_{Ymax,1'} = \frac{\sqrt{l^2 - b1'^2}}{\sqrt{3}}$ for inverted x-axes,

$X_{Ymax,1} = l - X_{Ymax,1'}$ for original x-axes,

$$Y_{max,1'} = \frac{V1 \cdot b1' \cdot \sqrt{(l^2 - b1'^2)^3}}{9 \cdot \sqrt{3} \cdot E \cdot J \cdot l}$$

Since the displacements $Y_{max,f}$ and $Y_{max,1}$ are in the opposite direction:

$$Y_{max,f} = Y_{max,1}$$

It is obtained:

$$V1(F)$$

In our case:

$$V1 = \frac{F \cdot bf \cdot \sqrt{(l^2 - bf^2)^3}}{b1 \cdot \sqrt{(l^2 - b1^2)^3}}$$

Then, from the sum of the moments in the system of equations (A1):

$$\Sigma Ma = F \cdot L = V1 \cdot L1 + V2 \cdot L2$$

$$V2 = \frac{(F \cdot L - V1 \cdot L1)}{L2}$$

Since:

$$F \cdot L < V1 \cdot L1$$

Therefore:

$$V2 < 0$$

However, since $Y2$ is not strictly a support because it does not constrain the upward movement, the beam will flex (Fig. A6). Therefore, the point of application of the force can be considered unique and, in particular, as the point closest to the force.

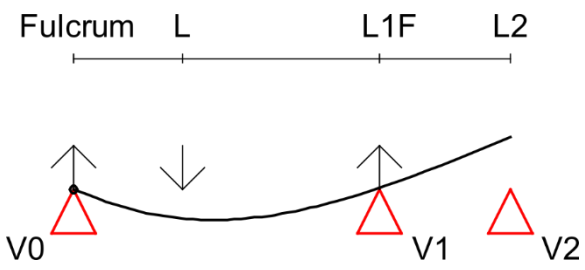

Figure A6. Representation of the effect superimposition analysis on the hyperstatic beam.

Despite the dental being modeled as a deformable beam, its lower deformability with respect to the device allows us to neglect it, only a deformation of the device is considered (Fig. A7). Then, only *L1* can be considered as a point of contact. The same approach can be replicated in the lower half of the system (Fig. A8).

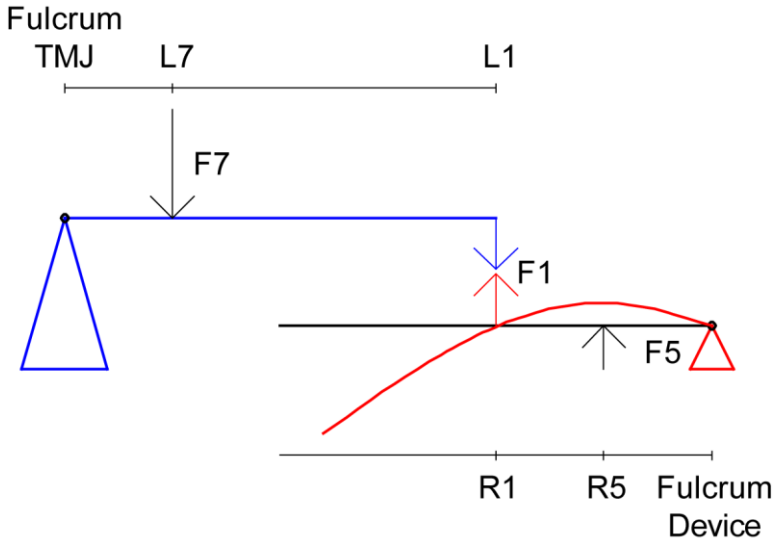

Figure A7. Representation of the single deformation acting only on the upper device fork plate.

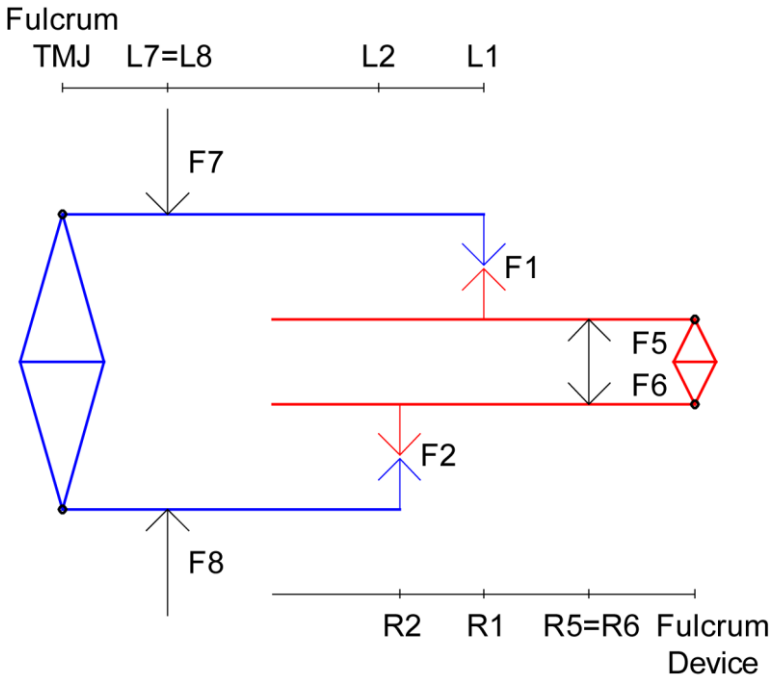

Figure A8. Representation of the masticatory system and the device with only one application point for each dental arc.

Since the distances of the upper and lower incisal teeth *R1* and *R2* are different, it is necessary to understand which of the two forces between *F1* and *F2* generates the moment recorded by the sensor (*M5* or *M6*). Therefore, the internal forces are neglected, and then the device is modeled as a unique rigid beam (Fig. A9).

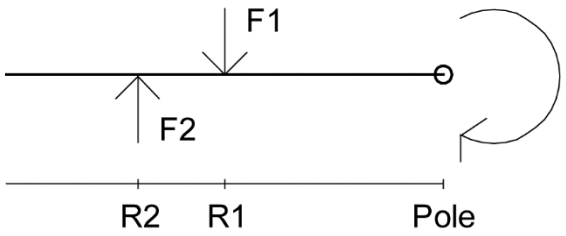

Figure A9. Representation of the masticatory system and the device neglecting internal forces.

Since the upper and lower forces are not applied along the same axis, the resultant unbalanced moment would generate a rotation. The direction of this moment will depend on the difference $R1 - R2$. However, since the real device does not actually rotate during the task, other constraints would compensate for the resultant moment. Therefore, the contact

points *R3* and *R4* can be reconsidered as applied points for constraint forces, which balance that moment. Whether *R1* < *R2*, the moment would have a clockwise direction and negative sign, which will unload on *R3* (Fig. A10).

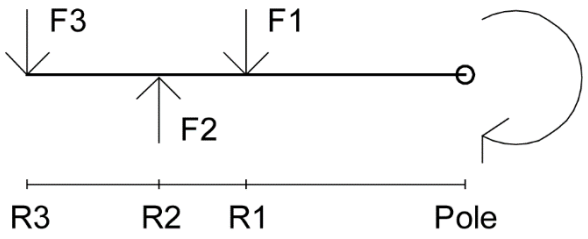

Figure A10. Representation of the masticatory system and the device neglecting internal forces and considering R3 as the moment unloading point.

$$\Sigma M = 0$$
$$M1 + M3 = M2$$
$$F1 \cdot R1 + F3 \cdot R3 = F2 \cdot R2$$

In summary, the device in Figure A1 can be modeled as in Figure 4, where based on the difference between *L1* and *L2*, an unload on *L3* or *L4* will occur.

If *R1* < *R2*:

$$F4 = 0$$

Knowing the force recorded on the sensor *F6*, the force applied in *F2* is obtained by summing the moments:

$$Ms = F6 \cdot R6 = F2 \cdot R2$$
$$F2 = \frac{F6 \cdot R6}{R2}$$

Then, from distance *L2* (incisor-masticatory system fulcrum distance) and *L8* (masticatory muscles-masticatory system fulcrum distance), the moment and, therefore, the force exerted by the masseter *F8*, can be calculated as a function of the force recorded at the sensor *F6*:

$$Mm = F8 \cdot L8 = F2 \cdot L2 = \frac{F6 \cdot R6}{R2} \cdot L2$$

Otherwise, if *R1* > *R2*:

$$F3 = 0$$
$$Ms = F5 \cdot R5 = F1 \cdot R1$$
$$F1 = \frac{F5 \cdot R5}{R1}$$

Finally, from the distance L1 (incisor-masticatory system fulcrum distance) and L7 (masseter-masticatory system fulcrum distance), the moment and, therefore, the force exerted by the masseter F7, can be calculated as a function of the force recorded at sensor F5:

$$Mm = F7 \cdot L7 = F1 \cdot L1 = \frac{F5 \cdot R5}{R1} \cdot L1$$

7. Conclusions

During my PhD program, I conducted research activities within 5 different projects that addressed different aspects of human movement, ranging from the analysis of visuomotor control of complex naturalistic movements, to the development and validation of novel upper-limb rehabilitation protocols for stroke survivors, to the development of a new device for the functional assessment of the masticatory system. The thesis has presented, for each project, the procedures that have been developed and the methods that have been used to obtain acceptable performances in terms of estimation of the physiological parameters and the metrics necessary to carry out, analyse and study various motor tasks. These projects mostly used low-cost technologies or technologies developed ad-hoc through open-source systems that allowed customization of the developed devices taking into account the individual characteristics of the participants. Methods were developed to obtain a reliable estimation of kinematic parameters and performance metrics useful for quantifying neuromotor function and to assess improvements due to the proposed rehabilitation protocols. Thanks to the VR systems and the 3D virtual environment development platforms, it has been possible to develop immersive scenarios that allow for studying complex tasks such as intercepting virtual balls, throwing virtual and real balls, and bimanually reaching virtual objects. The use of open source systems (such as the Arduino platform) combined with open-source software and 3D models development solutions has instead allowed the development of a subject-specific customized and low-cost system for recording the maximum bite force. Various data analysis methodologies were developed and compared to estimate with sufficient reliability the parameters necessary to establish the performance of the various motor tasks.

Regarding the first project (presented in chapter 2), VR was used to study complex visuomotor processes underlying interceptive actions. It was observed that adult naive participants, without any expertise in sports that involve throwing or interception, can extract information from the throwing action kinematic and use this information online to

improve their interception performance. It was also highlighted that some throwing styles among those identified are more informative than others. These results extend our current understanding of the nature of predictive abilities for action, and in particular for intercepting behaviour. Studies focusing on interceptive performance have demonstrated how humans use internal predictions of projectile trajectories to successfully intercept flying objects, presumably based on an internal model of how objects move under the effect of gravity. These results show that untrained adults are able to correctly predict the direction of projected objects based on the kinematics of the throwing action, which involves a more complex prediction capability than just processing the flight of a ball.

The second project (presented in chapter 3) focused on the development of low-cost system for studying unconstrained throwing of virtual and real balls. Such system is capable of recording the kinematic parameters necessary for characterizing throwing actions the exploiting the motion capture capability of a commercial VR system, replacing an expensive motion capture system as those usually employed for this type of studies. Ball release and ball impact parameters were used to quantify the accuracy and precision of the developed data acquisition setup. Time, position and speed of the ball release were estimated through several computational methods that were developed taking into account the ball-hand interactions and with ad-hoc hardware solutions, such a microswitch interfaced with the controller of the VR system. An image processing algorithm allowed to estimate time and position of ball impact on a target board. To obtain the most reliable parameters, several ball release estimation methods were compared. In the future, the system will be used to investigate the effect of different throwing styles and strategies, as well as sport expertise by recruiting participants practicing different sports, either involving throwing actions or not.

The third project (presented in chapter 4) has been conducted within a collaboration between UniMe, FSL, and DLR, aiming at the development and validation of a novel neuromotor rehabilitation approach. The main goal of the project, which is still ongoing, is

to use VR and myoelectric control to enhance recovery of upper limb motor functional in patients suffering from hemiparesis following a stroke event. The novel approach is based on the idea of using VR systems integrating motion capture sensors and machine learning techniques applied to EMG to provide assistance to patients during bimanual reaching tasks in the virtual environment by mirroring the unimpaired limb. As in a conventional mirror therapy, the developed rehabilitation protocol allows to assist the movement of a virtual representation of the impaired upper limb and the gesture of the virtual impaired hand with the mirrored movement and gesture of the unimpaired ones. Based on the functional assessment and recovery of the patient during the rehabilitation process, therapists can adjust the level of assistance taking into account the reaching performance. A preliminary analysis on the data collected so far has highlighted an improvement in the functionality of the upper limb, quantified through clinical evaluation (Fugl-Meyer) and instrumental evaluations. Clinical evaluations have highlighted a significant difference between the beginning and the end of the rehabilitation protocol. The instrumental evaluations have not shown a statistically significant improvement by comparing the selected parameters. This may be due to the choice of an inadequate metric. Future analysis will compare several additional parameters from the entire experimental dataset with the control group dataset, to find the best metric to quantify motor function and to highlight further statistical differences.

The fourth project (presented in chapter 5) aimed at extending the virtual mirror therapy approach described in chapter 4 by exploiting the full potential of myoelectric control. I performed this project during an internship at DLR. The idea was to use the EMG signals from many upper-limb muscles, rather than only from forearm muscle mostly involved in controlling hand gestures as in the approach described in chapter 4, to assist the movement of the virtual impaired limb. In this new system assistance will be provided by a combination of mirrored kinematics from the unimpaired hand and a prediction of the position of the impaired hand from EMG signals. Such myoelectric control component is intended to provide a salient feedback on the muscle patterns that need to be re-learned by

the patient and to stimulate positive neuroplasticity by reinforcing any attempt to improve the functionality of the muscle patterns. As a first step towards the development of such a system, as a proof-of-concept of the proposed approach, a data analysis was performed on a dataset previously collected at the FSL. The goal was to understand the feasibility of using EMG signals from many muscles of the entire upper limb, instead of only from forearm muscles, to estimate hand position. Different regression methods, including a machine learning algorithm previously developed by the DLR group to fit a non-linear mapping of EMG signal into hand kinematic variables, were compared to determine which was most adequate to perform the task. The non-linear method (RR-RFF), with the appropriate data pre-processing and regression parameters, provided the best prediction of the kinematic from EMG signals, superior with respect to the other linear methods. A new version of the VVITA software will be developed to validate the approach in an online operative scenario and to test the software on healthy participants as a model for motor rehabilitation of stroke survivors.

Finally, the fifth project (presented in chapter 6) resulted from a collaboration with the department of Odontoiatria ed Odontostomatologia of the Azienda Ospedaliera Universitaria (AOU) Gaetano Marino in Messina. It aimed at developing a new device to assess the functionality of the masticatory system by measuring the maximum bite force (MBF). A wireless, low-cost device was developed thought several iterations among the various collaborators, taking into account the individual anatomical and biomechanical characteristics of each participant and therefore customizable according to the participant's physiognomy. A method to standardize the repositioning of the device within the oral cavity was developed. The developed device and force estimation methods allow to estimate MBF in a reliable and repeatable manner over multiple measurement sessions. The device takes into account the different conformation of the mouth, which is a fundamental aspect for reliable recordings since the mouth acts as a physical lever and allows multi day recordings thanks to the position replacement standardization. Moreover, from the literature review emerged that no low-cost devices allow the MBF to be estimated reliably

and reproducibly in a laboratory without a development process based on industrial machinery. For this reason, both the software and the 3D CAD models needed to replicate the device have been available as open-source distribution. The device is a useful tool for estimating MBF in both single session clinical evaluation or in longitudinal studies and can be freely developed and used. Further studies will investigate the changes in MBF and evaluate the efficacy of physical therapy in specific pathologies such as TMD. Further development will integrate a low-cost EMG system to study the relation between MBF and jaw-closing myoelectric signals.

In sum, several research projects have been conducted for this PhD thesis, involving the investigation of basic principles of human motor control and the development of novel methods for the assessment of motor function and for neuromotor rehabilitation. While these projects addressed different neuroscientific and bioengineering questions, they all shared the use of VR tools and innovative data analysis methods. Several low-cost devices have been developed as a result of collaborations with other research groups of the University of Messina and international centres. Some of the work presented in this thesis has already been published in international scientific journals (iScience, Materials) or presented at international motion control or bioengineering conferences (International IEEE/EMBS Conference on Neural Engineering, Society for the Neural Control of Movement). Further developments and data analyses will be necessary to complete part of the ongoing studies and developments and to expand the research field of the already consolidated and published studies.

8. References

Abernethy, B. (1990). Expertise, Visual Search, and Information Pick-up in Squash. *Perception*, *19*(1), 63–77. https://doi.org/10.1068/p190063

Aglioti, S. M., Cesari, P., Romani, M., & Cosimo Urgesi. (2008). Action anticipation and motor resonance in elite basketball players. *Nature Neuroscience*, *11*(9), 1109–1116. https://doi.org/10.1038/nn.2182

Ambrosini, E., Pezzulo, G., & Costantini, M. (2015). The eye in hand: Predicting others' behavior by integrating multiple sources of information. *Journal of Neurophysiology*, *113*(7), 2271–2279. https://doi.org/10.1152/jn.00464.2014

Ansuini, C., Cavallo, A., Bertone, C., & Becchio, C. (2015). Intentions in the Brain: The Unveiling of Mister Hyde. *The Neuroscientist*, *21*(2), 126–135. https://doi.org/10.1177/1073858414533827

Ansuini, C., Giosa, L., Turella, L., Altoè, G., & Castiello, U. (2008). An object for an action, the same object for other actions: Effects on hand shaping. *Experimental Brain Research*, *185*(1), 111–119. https://doi.org/10.1007/s00221-007-1136-4

Bakke, M. (2006). Bite Force and Occlusion. *Seminars in Orthodontics*, *12*(2), 120–126. https://doi.org/10.1053/j.sodo.2006.01.005

Bakke, M., Holm, B., Jensen, B. L., Michler, L., & Möller, E. (1990). Unilateral, isometric bite force in 8-68-year-old women and men related to occlusal factors. *European Journal of Oral Sciences*, *98*(2), 149–158. https://doi.org/10.1111/j.1600-0722.1990.tb00954.x

Bizzi, E., Cheung, V. C. K., d'Avella, A., Saltiel, P., & Tresch, M. (2008). Combining modules for movement. *Brain Research Reviews*, *57*(1), 125–133. https://doi.org/10.1016/j.brainresrev.2007.08.004

Braun, S., Hnat, W. P., Freudenthaler, J. W., Marcotte, M. R., Hönigle, K., & Johnson, B. E. (1996). A study of maximum bite force during growth and development. *The Angle Orthodontist*, *66*(4), 261–264. https://doi.org/10.1043/0003-3219(1996)066<0261:ASOMBF>2.3.CO;2

Brenner, E., & Smeets, J. B. J. (2018). Continuously updating one's predictions underlies successful interception. *Journal of Neurophysiology*, *120*(6), 3257–3274. https://doi.org/10.1152/jn.00517.2018

Calderon, P. dos S., Kogawa, E. M., Lauris, J. R. P., & Conti, P. C. R. (2006). The influence of gender and bruxism on the human maximum bite force. *Journal of Applied Oral Science*, *14*(6), 448–453. https://doi.org/10.1590/S1678-77572006000600011

Calvin, W. H. (1982). Did throwing stones shape hominid brain evolution? *Ethology and Sociobiology*, *3*(3), 115–124. https://doi.org/10.1016/0162-3095(82)90010-3

Calvo-Merino, B., Ehrenberg, S., Leung, D., & Haggard, P. (2010). Experts see it all: Configural effects in action observation. *Psychological Research PRPF*, *74*(4), 400–406. https://doi.org/10.1007/s00426-009-0262-y

Casile, A., & Giese, M. A. (2006). Nonvisual Motor Training Influences Biological Motion Perception. *Current Biology*, *16*(1), 69–74. https://doi.org/10.1016/j.cub.2005.10.071

Cavallo, A., Koul, A., Ansuini, C., Capozzi, F., & Becchio, C. (2016). Decoding intentions from movement kinematics. *Scientific Reports*, *6*(1), 37036. https://doi.org/10.1038/srep37036

Cheung, V. C. K., Piron, L., Agostini, M., Silvoni, S., Turolla, A., & Bizzi, E. (2009). Stability of muscle synergies for voluntary actions after cortical stroke in humans. *Proceedings of the National Academy of Sciences of the United States of America*, *106*(46), 19563–19568. https://doi.org/10.1073/pnas.0910114106

Cheung, V. C. K., Turolla, A., Agostini, M., Silvoni, S., Bennis, C., Kasi, P., Paganoni, S., Bonato, P., & Bizzi, E. (2012). Muscle synergy patterns as physiological markers of motor cortical damage. *Proceedings of the National Academy of Sciences of the United States of America*, *109*(36), 14652–14656. https://doi.org/10.1073/pnas.1212056109

Clark, D. J., Ting, L. H., Zajac, F. E., Neptune, R. R., & Kautz, S. A. (2010). Merging of Healthy Motor Modules Predicts Reduced Locomotor Performance and Muscle Coordination Complexity Post-Stroke. *Journal of Neurophysiology*, *103*(2), 844–857. https://doi.org/10.1152/jn.00825.2009

Cramer, S. C., Nelles, G., Benson, R. R., Kaplan, J. D., Parker, R. A., Kwong, K. K., Kennedy, D. N., Finklestein, S. P., & Rosen, B. R. (1997). A Functional MRI Study of Subjects Recovered From Hemiparetic Stroke. *Stroke*, *28*(12), 2518–2527. https://doi.org/10.1161/01.STR.28.12.2518

Crandall, S. H., Dahl, N. C., & Lardner, T. J. (1978). *An introduction to the mechanics of solids*. McGrawHill International Book Company.

d'Avella, A., Portone, A., Fernandez, L., & Lacquaniti, F. (2006). Control of Fast-Reaching Movements by Muscle Synergy Combinations. *Journal of Neuroscience*, *26*(30), 7791–7810. https://doi.org/10.1523/JNEUROSCI.0830-06.2006

Dayan, E., Casile, A., Levit-Binnun, N., Giese, M. A., Hendler, T., & Flash, T. (2007). Neural representations of kinematic laws of motion: Evidence for action-perception coupling. *Proceedings of the National Academy of Sciences*, *104*(51), 20582–20587. https://doi.org/10.1073/pnas.0710033104

DiCicco, M., Lucas, L., & Matsuoka, Y. (2004). Comparison of control strategies for an EMG controlled orthotic exoskeleton for the hand. *IEEE International Conference on Robotics and Automation, 2004. Proceedings. ICRA '04. 2004*, 1622-1627 Vol.2. https://doi.org/10.1109/ROBOT.2004.1308056

Domínguez-Téllez, P., Moral-Muñoz, J. A., Salazar, A., Casado-Fernández, E., & Lucena-Antón, D. (2020). Game-Based Virtual Reality Interventions to Improve Upper Limb Motor Function and Quality of Life After Stroke: Systematic Review and Meta-analysis. *Games for Health Journal*, *9*(1), 1–10. https://doi.org/10.1089/g4h.2019.0043

Donnarumma, F., Costantini, M., Ambrosini, E., Friston, K., & Pezzulo, G. (2017). Action perception as hypothesis testing. *Cortex*, *89*, 45–60. https://doi.org/10.1016/j.cortex.2017.01.016

Dýraçoðlu, D., Güçlü, B., Alptekin, K., Karan, A., & Aksoy, C. (2008). *MAXIMAL BITE FORCE MEASUREMENT BY THE «ISTANBUL BITE FORCE RECORDER» «ÝSTANBUL KUVVET ÖLÇERÝ» ÝLE MAKSÝMAL ISIRMA KUVVETÝ ÖLÇÜMÜ*. 7.

Farrow, D., Abernethy, B., & Jackson, R. C. (2005). Probing Expert Anticipation with the Temporal Occlusion Paradigm: Experimental Investigations of Some Methodological Issues. *Motor Control*, *9*(3), 330–349. https://doi.org/10.1123/mcj.9.3.330

Fernandes, C. P., Glantz, P.-O. J., Svensson, S. A., & Bergmark, A. (2003). A novel sensor for bite force determinations. *Dental materials*, *19*(2), 118–126.

Ferrario, V. F., Sforza, C., Serrao, G., Dellavia, C., & Tartaglia, G. M. (2004). Single tooth bite forces in healthy young adults. *Journal of Oral Rehabilitation*, *31*(1), 18–22. https://doi.org/10.1046/j.0305-182X.2003.01179.x

Flanagan, D., Ilies, H., O'Brien, B., McManus, A., & Larrow, B. (2012). Jaw Bite Force Measurement Device. *Journal of Oral Implantology*, *38*(4), 361–364. https://doi.org/10.1563/AAID-JOI-D-10-00101

Flanagan, J. R., & Johansson, R. S. (2003). Action plans used in action observation. *Nature*, *424*(6950), 769–771. https://doi.org/10.1038/nature01861

Foley, N., Pereira, S., Salter, K., Meyer, M., Andrew McClure, J., & Teasell, R. (2012). Are Recommendations Regarding Inpatient Therapy Intensity Following Acute Stroke Really Evidence-Based? *Topics in Stroke Rehabilitation*, *19*(2), 96–103. https://doi.org/10.1310/tsr1902-96

Franklin, D. W., & Wolpert, D. M. (2011). Computational mechanisms of sensorimotor control. *Neuron*, *72*(3), 425–442. https://doi.org/10.1016/j.neuron.2011.10.006

Ganesh, G., & Burdet, E. (2013). Motor planning explains human behaviour in tasks with multiple solutions. *Robotics and Autonomous Systems*, *61*(4), 362–368. https://doi.org/10.1016/j.robot.2012.09.024

Ganesh, G., Haruno, M., Kawato, M., & Burdet, E. (2010). Motor Memory and Local Minimization of Error and Effort, Not Global Optimization, Determine Motor Behavior. *Journal of Neurophysiology*, *104*(1), 382–390. https://doi.org/10.1152/jn.01058.2009

Garner, L. D., & Kotwal, N. S. (1973). Correlation Study of Incisive Biting Forces with Age, Sex, and Anterior Occlusion. *Journal of Dental Research*, *52*(4), 698–702. https://doi.org/10.1177/00220345730520041001

Giese, M. A., & Rizzolatti, G. (2015). Neural and Computational Mechanisms of Action Processing: Interaction between Visual and Motor Representations. *Neuron*, *88*(1), 167–180. https://doi.org/10.1016/j.neuron.2015.09.040

Gijsberts, A., Bohra, R., Sierra González, D., Werner, A., Nowak, M., Caputo, B., Roa, M. A., & Castellini, C. (2014). Stable myoelectric control of a hand prosthesis using non-linear incremental learning. *Frontiers in Neurorobotics*, *8*. https://doi.org/10.3389/fnbot.2014.00008

GitHub - Xirexel/CaptureManagerSDK: CaptureManager SDK - Capturing, Recording and Streaming Video and Audio from Web-Cams. (s.d.). GitHub. https://github.com/Xirexel/CaptureManagerSDK

Gladstone, D. J., Danells, C. J., & Black, S. E. (2002). The Fugl-Meyer Assessment of Motor Recovery after Stroke: A Critical Review of Its Measurement Properties. *Neurorehabilitation and Neural Repair*, *16*(3), 232–240. https://doi.org/10.1177/154596802401105171

Gokhare, V. G., & Raut, D. D. N. (2017). A Review paper on 3D-Printing Aspects and Various Processes Used in the 3D-Printing. *International Journal of Engineering Research*, *6*(06), 7.

GoProCSharpSample: Open GoPro. https://gopro.github.io/OpenGoPro/demos/csharp/GoProCSharpSample

Gu, Y., Bai, Y., & Xie, X. (2021). Bite Force Transducers and Measurement Devices. *Frontiers in Bioengineering and Biotechnology*, *9*, 665081. https://doi.org/10.3389/fbioe.2021.665081

Guimaraes, A. S., Carlsson, G. E., & Marie, S. K. N. (2007). Bite force and handgrip force in patients with molecular diagnosis of myotonic dystrophy. *Journal of Oral Rehabilitation*, *34*(3), 195–200. https://doi.org/10.1111/j.1365-2842.2006.01665.x

Helkimo, E., Carlsson, G. E., & Carmeli, Y. (1975). Bite force in patients with functional disturbances of the masticatory system. *Journal of Oral Rehabilitation*, *2*(4), 397–406. https://doi.org/10.1111/j.1365-2842.1975.tb01539.x

Hellsing, G. (1980). On the regulation of interincisor bite force in man. *Journal of Oral Rehabilitation*, *7*(5), 403–411. https://doi.org/10.1111/j.1365-2842.1980.tb00459.x

Huys, R., Cañal-Bruland, R., Hagemann, N., Beek, P. J., Smeeton, N. J., & Williams, A. M. (2009). Global Information Pickup Underpins Anticipation of Tennis Shot Direction. *Journal of Motor Behavior*, *41*(2), 158–171. https://doi.org/10.3200/JMBR.41.2.158-171

Karamians, R., Proffitt, R., Kline, D., & Gauthier, L. V. (2020). Effectiveness of Virtual Reality- and Gaming-Based Interventions for Upper Extremity Rehabilitation

Poststroke: A Meta-analysis. *Archives of Physical Medicine and Rehabilitation*, *101*(5), 885–896. https://doi.org/10.1016/j.apmr.2019.10.195

Koc, D., Dogan, A., & Bek, B. (2010). Bite Force and Influential Factors on Bite Force Measurements: A Literature Review. *European Journal of Dentistry*, *04*(02), 223–232. https://doi.org/10.1055/s-0039-1697833

Krotov, A., Russo, M., Nah, M., Hogan, N., & Sternad, D. (2022). Motor control beyond reach—How humans hit a target with a whip. *Royal Society Open Science*. https://doi.org/10.1098/rsos.220581

Kwakkel, G., van Peppen, R., Wagenaar, R. C., Wood Dauphinee, S., Richards, C., Ashburn, A., Miller, K., Lincoln, N., Partridge, C., Wellwood, I., & Langhorne, P. (2004). Effects of Augmented Exercise Therapy Time After Stroke. *Stroke*, *35*(11), 2529–2539. https://doi.org/10.1161/01.STR.0000143153.76460.7d

Liarokapis, M. V., Artemiadis, P. K., Kyriakopoulos, K. J., & Manolakos, E. S. (2013). A Learning Scheme for Reach to Grasp Movements: On EMG-Based Interfaces Using Task Specific Motion Decoding Models. *IEEE Journal of Biomedical and Health Informatics*, *17*(5), 915–921. https://doi.org/10.1109/JBHI.2013.2259594

Linderholm, Håk., & Wennström, A. (1970). Isometric Bite Force and its Relation to General Muscle Forge and Body Build. *Acta Odontologica Scandinavica*, *28*(5), 679–689. https://doi.org/10.3109/00016357009058590

Linsen, S., Schmidt-Beer, U., Fimmers, R., Grüner, M., & Koeck, B. (2009). Craniomandibular Pain, Bite Force, and Oral Health-Related Quality of Life in Patients with Jaw

Resection. *Journal of Pain and Symptom Management*, *37*(1), 94–106. https://doi.org/10.1016/j.jpainsymman.2006.12.019

Lombardo, M. P., & Deaner, R. O. (2018). Born to Throw: The Ecological Causes that Shaped the Evolution of Throwing In Humans. *The Quarterly Review of Biology*, *93*(1), 1–16. https://doi.org/10.1086/696721

Mann, D. L., Abernethy, B., & Farrow, D. (2010). Action specificity increases anticipatory performance and the expert advantage in natural interceptive tasks. *Acta Psychologica*, *135*(1), 17–23. https://doi.org/10.1016/j.actpsy.2010.04.006

Manns, A., Miralles, R., & Palazzi, C. (1979). EMG, bite force, and elongation of the masseter muscle under isometric voluntary contractions and variations of vertical dimension. *Journal of prosthetic dentistry*, *42*(6), 674–682.

Mardia, K. V., Kent, J. T., & Bibby, J. M. (1979). *Multivariate analysis*. Academic Press.

Maselli, A., Dhawan, A., Cesqui, B., Russo, M., Lacquaniti, F., & d'Avella, A. (2017). Where are you throwing the ball? I better watch your body, not just your arm! *Frontiers in Human Neuroscience*, *11*. https://doi.org/10.3389/fnhum.2017.00505

Maselli, A., Dhawan, A., Russo, M., Cesqui, B., Lacquaniti, F., & d'Avella, A. (2019). A whole-body characterization of individual strategies, gender differences and common styles in overarm throwing. *Journal of Neurophysiology*, 2486–2503. https://doi.org/10.1152/jn.00011.2019

Molin, C. (1972). Vertical Isometric Muscle Forces of the Mandible: A Comparative Study of Subjects with and Without Manifest Mandibular Pain Dysfunction Syndrome. *Acta Odontologica Scandinavica*, *30*(4), 485–499. https://doi.org/10.3109/00016357209002499

Müller, S., & Abernethy, B. (2012). Expert Anticipatory Skill in Striking Sports: A Review and a Model. *Research Quarterly for Exercise and Sport*, *83*(2), 175–187. https://doi.org/10.5641/027013612800745059

Oldfield, R. C. (1971). The assessment and analysis of handedness: The Edinburgh inventory. In *Neuropsychologia* (Vol. 9, Fascicolo 1, pp. 97–113). https://doi.org/10.1016/0028-3932(71)90067-4

Payne, V. G. (2017). *Human Motor Development: A lifespan approach* (9ª ed.). Routledge. https://doi.org/10.4324/9781315213040

Peper, L., Bootsma, R. J., Mestre, D. R., & Bakker, F. C. (1994). Catching balls: How to get the hand to the right place at the right time. *Journal of Experimental Psychology: Human Perception and Performance*, *20*, 591–612. https://doi.org/10.1037/0096-1523.20.3.591

Pezzulo, G., Donnarumma, F., Dindo, H., D'Ausilio, A., Konvalinka, I., & Castelfranchi, C. (2019). The body talks: Sensorimotor communication and its brain and kinematic signatures. *Physics of Life Reviews*, *28*, 1–21. https://doi.org/10.1016/j.plrev.2018.06.014

Roach, N. T., & Richmond, B. G. (2015). Clavicle length, throwing performance and the reconstruction of the Homo erectus shoulder. *Journal of Human Evolution*, *80*, 107–113. https://doi.org/10.1016/j.jhevol.2014.09.004

Roach, N. T., Venkadesan, M., Rainbow, M. J., & Lieberman, D. E. (2013). Elastic energy storage in the shoulder and the evolution of high-speed throwing in Homo. *Nature*, *498*(7455), 483–486. https://doi.org/10.1038/nature12267

Rohrer, B., Fasoli, S., Krebs, H. I., Hughes, R., Volpe, B., Frontera, W. R., Stein, J., & Hogan, N. (2002). Movement Smoothness Changes during Stroke Recovery. *The Journal of*

Neuroscience, *22*(18), 8297–8304. https://doi.org/10.1523/JNEUROSCI.22-18-08297.2002

Russo, M., Cesqui, B., La Scaleia, B., Ceccarelli, F., Maselli, A., Moscatelli, A., Zago, M., Lacquaniti, F., & d'Avella, A. (2017). Intercepting virtual balls approaching under different gravity conditions: Evidence for spatial prediction. *Journal of Neurophysiology*, *118*(4), 2421–2434. https://doi.org/10.1152/jn.00025.2017

Russo, M., Ozeri-Engelhard, N., Hupfeld, K., Nettekoven, C., Thibault, S., Sedaghat-Nejad, E., Buchwald, D., Xing, D., Zobeiri, O., Kilteni, K., Albert, S. T., & Ariani, G. (2021). Highlights from the 30th Annual Meeting of the Society for the Neural Control of Movement. *Journal of Neurophysiology*, *126*(4), 967–975. https://doi.org/10.1152/jn.00334.2021

Sanford, J., Moreland, J., Swanson, L. R., Stratford, P. W., & Gowland, C. (1993). Reliability of the Fugl-Meyer Assessment for Testing Motor Performance in Patients Following Stroke. *Physical Therapy*, *73*(7), 447–454. https://doi.org/10.1093/ptj/73.7.447

Shadmehr, R., & Mussa-Ivaldi, F. A. (1994). Adaptive representation of dynamics during learning of a motor task. *Journal of Neuroscience*, *14*(5), 3208–3224. https://doi.org/10.1523/JNEUROSCI.14-05-03208.1994

Sharif Razavian, R. (2017). *A Human Motor Control Framework based on Muscle Synergies*. Waterloo.

Singh, S., Sandhu, N., Utreja, A. K., & Dhaliwal, Y. S. (2011). An Innovative Miniature Bite Force Recorder. *International Journal of Clinical Pediatric Dentistry*, *4*(2), 113–118. https://doi.org/10.5005/jp-journals-10005-1093

Song, R., Tong, K., Hu, X., & Zhou, W. (2013). Myoelectrically controlled wrist robot for stroke rehabilitation. *Journal of NeuroEngineering and Rehabilitation*, *10*(1), 52. https://doi.org/10.1186/1743-0003-10-52

Soriano, M., Cavallo, A., D'Ausilio, A., Becchio, C., & Fadiga, L. (2018). Movement kinematics drive chain selection toward intention detection. *Proceedings of the National Academy of Sciences*, *115*(41), 10452–10457. https://doi.org/10.1073/pnas.1809825115

SteamVR su Steam. https://store.steampowered.com/app/250820/SteamVR/

Testa, M., Di Marco, A., Pertusio, R., Van Roy, P., Cattrysse, E., & Roatta, S. (2016). A validation study of a new instrument for low cost bite force measurement. *Journal of Electromyography and Kinesiology*, *30*, 243–248. https://doi.org/10.1016/j.jelekin.2016.08.005

Thomas, J. S., France, C. R., Leitkam, S. T., Applegate, M. E., Pidcoe, P. E., & Walkowski, S. (2016). Effects of Real-World Versus Virtual Environments on Joint Excursions in Full-Body Reaching Tasks. *IEEE Journal of Translational Engineering in Health and Medicine*, *4*, 1–8. https://doi.org/10.1109/JTEHM.2016.2623787

Todorov, E., & Jordan, M. I. (2002). Optimal feedback control as a theory of motor coordination. *Nature Neuroscience*, *5*(11), Art. 11. https://doi.org/10.1038/nn963

Tommasino, P., Maselli, A., Campolo, D., Lacquaniti, F., & d'Avella, A. (2021). A Hessian-based decomposition characterizes how performance in complex motor skills depends on individual strategy and variability. *PLOS ONE*, *16*(6), e0253626. https://doi.org/10.1371/journal.pone.0253626

Tortopidis, D., Lyons, M. F., Baxendale, R. H., & Gilmour, W. H. (1998). The variability of bite force measurement between sessions, in different positions within the dental arch. *Journal of Oral Rehabilitation*, *25*(9), 681–686. https://doi.org/10.1046/j.1365-2842.1998.00293.x

Unity Real-Time Development Platform | 3D, 2D VR & AR Engine. https://unity.com/

Van Der Bilt, A., Tekamp, A., Van Der Glas, H., & Abbink, J. (2008). Bite force and electromyograpy during maximum unilateral and bilateral clenching. *European journal of oral sciences*, *116*(3), 217–222.

Van Eijden, T. M. G. J. (1990). Jaw Muscle Activity in Relation to the Direction and Point of Application of Bite Force. *Journal of Dental Research*, *69*(3), 901–905. https://doi.org/10.1177/00220345900690031401

van Steenberghe, D., & de Vries, J. H. (1978). The development of a maximal clenching force between two antagonistic teeth. *Journal of Periodontal Research*, *13*(1), 91–97. https://doi.org/10.1111/j.1600-0765.1978.tb00157.x

Veerbeek, J. M., van Wegen, E., van Peppen, R., van der Wees, P. J., Hendriks, E., Rietberg, M., & Kwakkel, G. (2014). What Is the Evidence for Physical Therapy Poststroke? A Systematic Review and Meta-Analysis. *PLoS ONE*, *9*(2), e87987. https://doi.org/10.1371/journal.pone.0087987

Verma, T. P., Kumathalli, K. I., Jain, V., & Kumar, R. (2017). Bite Force Recording Devices—A Review. *Journal of Clinical and Diagnostic Research: JCDR*, *11*(9), ZE01–ZE05. https://doi.org/10.7860/JCDR/2017/27379.10450

Vidal, P.-P., & Lacquaniti, F. (2021). Perceptual-motor styles. *Experimental Brain Research*, *239*(5), 1359–1380. https://doi.org/10.1007/s00221-021-06049-0

Waltimo, A., & Könönen, M. (1993). A novel bite force recorder and maximal isometric bite force values for healthy young adults. *European Journal of Oral Sciences*, *101*(3), 171–175.

Young, R. W. (2009). The ontogeny of throwing and striking. *Human_ontogenetics*, *3*(1), 19–31. https://doi.org/10.1002/huon.200800013

Zago, M., McIntyre, J., Senot, P., & Lacquaniti, F. (2008). Internal models and prediction of visual gravitational motion. *Vision Research*, *48*(14), 1532–1538. https://doi.org/10.1016/j.visres.2008.04.005

Zago, M., McIntyre, J., Senot, P., & Lacquaniti, F. (2009). Visuo-motor coordination and internal models for object interception. *Experimental Brain Research*, *192*(4), 571–604. https://doi.org/10.1007/s00221-008-1691-3

Zhang, Z., & Sternad, D. (2021). Back to reality: Differences in learning strategy in a simplified virtual and a real throwing task. *Journal of Neurophysiology*, *125*(1), 43–62. https://doi.org/10.1152/jn.00197.2020

9. Acknowledgement

First of all, I would like to thank my tutor, Prof. Andrea d'Avella, for giving me the great opportunity to grow up in such a stimulating laboratory. I am very grateful for being one of his students and for having had the chance to learn from him. In particular I would like to thank Andrea for being not only a brilliant and thoughtful advisor, but also for being a mentor and a supportive guide during these years.

A special thank you goes to my fabulous team, Antonella, Daniele, Denise, Marta, Sergio, and all the people met at IRCCS Santa Lucia Foundation, at the Institute of Robotics and Mechatronics and at University of Messina. We shared a lot in these years and I couldn't make it without their support, long chats and their precious tips.

Finally, I thank my family, my sister, my cousins and my friends who have been always there for me and I thank them for being such a strong support. I would like to thank them for being patient with me, always on my side and for taking care of me. Thanks for all the time you have dedicated to me, you helped me becoming who I am and I hope you will keep doing that. Wherever I go I bring you all with me.